Lyle, M., Wilson, P.A., Janecek, T.R., et al., 2002
Proceedings of the Ocean Drilling Program, Initial Reports Volume 199

2. EXPLANATORY NOTES[1]

Shipboard Scientific Party[2]

INTRODUCTION

Information assembled in this chapter will help the reader understand the basis for our preliminary conclusions and also enable the interested investigator to select samples for further analysis. This information concerns only shipboard operations and analyses described in the site reports in the Leg 199 *Initial Reports* volume of the *Proceedings of the Ocean Drilling Program*. Methods used by various investigators for shore-based analyses of Leg 199 data will be described in the individual contributions published in the *Scientific Results* volume and in publications in various professional journals.

Authorship of Site Chapters

The separate sections of the site chapters were written by the following shipboard scientists (authors are listed in alphabetical order; no seniority is implied):

Principal Results: Shipboard Scientific Party
Background and Objectives: Lyle, Wilson
Operations: Grout, Janecek
Lithostratigraphy: Hovan, Kruse, Nishi, D. Rea, Steiger, Tripati, Wade
Biostratigraphy: Backman, Coxall, Moore, Nigrini, Nomura, Norris, Raffi
Paleomagnetism: Lanci, Pares
Composite Depths: Janecek, Moore, Pälike
Sedimentation and Accumulation Rates: Moore, D. Rea
Geochemistry: Faul, Lear, Quintin
Physical Properties: Busch, Vanden Berg
Downhole Measurements: Gaillot, Knoop, B. Rea

[1]Examples of how to reference the whole or part of this volume.
[2]Shipboard Scientific Party addresses.

Ms 199IR-102

Drilling Operations

Two standard coring systems were used during Leg 199: the advanced piston corer (APC), and the extended core barrel (XCB). These standard coring systems and their characteristics are summarized in various "Explanatory Notes" chapters of previous *Initial Reports* volumes as well as in a number of technical notes. The Leg 139 *Initial Reports* volume includes a particularly detailed description of these systems. Most cored intervals were ~9.6 m long, which is the length of a standard core barrel. In a few cases, the drill string was drilled, or "washed ahead," without recovering sediments to advance the drill bit to a target depth where core recovery needed to be resumed.

Drilled intervals are referred to in meters below rig floor (mbrf) that are measured from the kelly bushing on the rig floor to the bottom of the drill pipe and meters below seafloor (mbsf) that are calculated. When sediments of substantial thickness cover the seafloor, the mbrf depth of the seafloor is determined with a mudline core, assuming 100% recovery for the cored interval in the first core. Water depth is calculated by subtracting the distance from the rig floor to sea level from the mudline measurement in mbrf. This water depth usually differs from precision depth recorder measurements by a few to several meters. The mbsf depths of core tops are determined by subtracting the seafloor depth (in mbrf) from the core-top depth (in mbrf). The resulting core-top datums in mbsf are the ultimate reference for any further depth calculation procedures.

Drilling Deformation

When cores are split, many show signs of significant sediment disturbance, including the concave-downward appearance of originally horizontal bedding, haphazard mixing of lumps of different lithologies (mainly at the tops of cores), fluidization, and flow-in. Core deformation may also occur during retrieval because of changes in pressure and temperature as the core is raised and during cutting and core handling on deck.

Curatorial Procedures and Sample Depth Calculations

Numbering of sites, holes, cores, and samples follows the standard Ocean Drilling Program (ODP) procedure (Fig. F1). A full curatorial identifier for a sample consists of the leg, site, hole, core number, core type, section number, and interval in centimeters measured from the top of the core section. For example, a sample identification of 199-1215A-1H-1, 10–12 cm, represents a sample removed from the interval between 10 and 12 cm below the top of Section 1, Core 1 (H designates that this core was taken with the APC system) of Hole 1215A during Leg 199. Cored intervals are also referred to in "curatorial" mbsf. The mbsf of a sample is calculated by adding the depth of the sample below the section top and the lengths of all higher sections in the core to the core top datum measured with the drill string.

A sediment core from less than a few hundred mbsf may expand upon recovery (typically 10% in the upper 300 mbsf), and its length may not necessarily match the drilled interval. In addition, a coring gap typically occurs between cores, as shown by composite depth construction (see Mayer, Pisias, Janecek, et al., 1992; Exon, Kennett, Malone, et al., 2001). Thus, a discrepancy may exist between the drilling mbsf and

F1. Example of coring and depth intervals, p. 43.

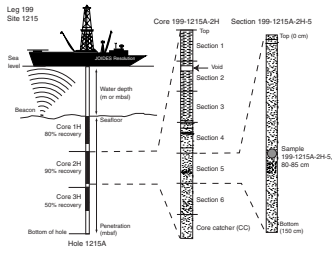

the curatorial mbsf. For instance, the curatorial mbsf of a sample taken from the bottom of a core may be greater than that of a sample from the top of the subsequent core, where the latter corresponds to the drilled core-top datum.

If a core has incomplete recovery, all cored material is assumed to originate from the top of the drilled interval as a continuous section for curation purposes. The true depth interval within the cored interval is not known. This should be considered as a sampling uncertainty in age-depth analysis and correlation of core facies with downhole log signals.

Core Handling and Analysis

General core-handling procedures (described in previous *Initial Reports* volumes and the Shipboard Scientist's Handbook) are summarized here. As soon as the cores arrived on deck, gas-void samples (if present) were taken, by means of a syringe, for immediate analysis as part of the shipboard safety and pollution prevention program. Core catcher samples were obtained for biostratigraphic analysis. When the core was cut in sections, whole-round samples were taken for shipboard interstitial water analysis, if needed. In addition, headspace gas samples were immediately extracted from the ends of cut sections and sealed in glass vials for light hydrocarbon analysis.

Before splitting, whole-round core sections were run through the multisensor track (MST), and thermal conductivity measurements were taken. The cores were then split into working and archive halves (from bottom to top). Investigators should be aware that older material could have been transported upward on the split face of each section by the splitting process. When short pieces of sedimentary rock were recovered, the individual pieces were split with the rock saw and placed in split liner compartments (created by sealing spacers into the liners with acetone).

Coherent and reasonably long archive-half sections were measured for color reflectance using the archive-half multisensor track (AMST). All archive-half sections were run through the cryogenic magnetometer, described macroscopically and microscopically, and photographed with both black-and-white and color film. Close-up photographs were taken of particular features for illustrations in site chapters, as requested by individual scientists. During Leg 199, a digital imaging track system equipped with a line-scan camera was used extensively.

The working half was sampled both for shipboard analysis—such as physical properties, carbonate, and bulk X-ray diffraction (XRD) mineralogy—and for shore-based studies. Both halves of the core were then put into labeled plastic tubes, sealed, and placed in cold storage space aboard the ship. At the end of the leg, the cores were transferred from the ship into refrigerated containers and shipped to the ODP Gulf Coast Repository in College Station, Texas.

LITHOSTRATIGRAPHY

Sediment Barrel Sheets

Core-description forms, or "barrel sheets," provide a summary of the data obtained during shipboard analysis of each sediment core. Detailed observations of each section were recorded initially by hand on standard ODP visual core description (VCD) forms. Copies of original

VCD forms are available from ODP upon request. This information was subsequently entered into AppleCORE software (version 8.1m), which generates a simplified, annotated graphical description (barrel sheet) for each core (Fig. F2). These barrel sheets appear alongside corresponding core photographs (see the "Core Descriptions" contents list). Site, hole, and depth (in mbsf) are given at the top of the barrel sheet, with mbsf positions of core sections along the left margin. Columns on the barrel sheets include graphic lithology, bioturbation, sediment disturbance, sample types, color, and remarks. Features related to sedimentary structures, lithologic accessories, and fossils are plotted on the graphic lithology near the depth interval where they are present. These columns are discussed below, followed by an outline of the lithologic classification used during Leg 199. In addition to lithologic information, graphs showing measurements collected by the MST were plotted alongside each core interval. These data include gamma ray attenuation (GRA) densitometer bulk density (g/cm^3), corrected magnetic susceptibility (MS) (10^{-5} SI units), and lightness as determined by color reflectance (L^*).

F2. Example of an AppleCORE summary barrel sheet, p. 44.

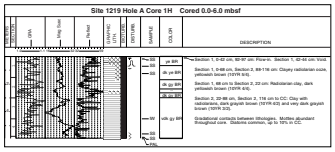

Graphic Lithology

Lithologies of the core intervals recovered are represented on barrel sheets by graphic patterns in the column titled "Graphic Lithology" (Fig. F3). For intervals containing homogeneous mixtures of multiple lithologies, symbols are arranged within the column from left to right in order of their relative abundance. Graphic lithologies are used for all components that comprise 25% or more of the total sediment. The width of each pattern in the column approximates the relative abundance of that component. Relative abundances reported in this volume are useful for general characterization of the sediment but are not precise, quantitative data.

F3. Key to symbols used for graphic lithologies, p. 45.

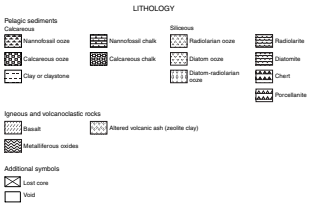

Sedimentary Structures

Sedimentary structures formed by natural processes (i.e., not a result of drilling disturbance) are represented on the barrel sheet with symbols placed on the graphic lithology (Fig. F4). Structures formed by both biogenic and physical processes are included. These include varying degrees of bioturbation, types of trace fossils, parallel laminations, macro- and microfaults, and soft sediment deformation structures.

F4. Key to other symbols used on the computer-generated core-description forms, p. 46.

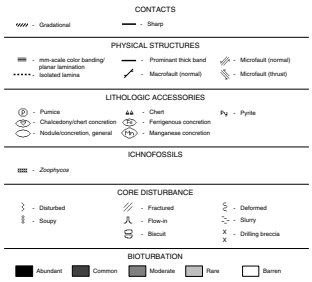

Bioturbation

Five levels of bioturbation are recognized using a scheme similar to that of Droser and Bottjer (1986). Bioturbation intensity is classified as abundant (>75%), common (>50%–75%), moderate (10%–50%), rare (<10%), and absent (none). These levels are illustrated with graphic symbols in the "Bioturbation" column (Fig. F4).

Accessory Lithologies, Authigenic Minerals, Concretions, Fossils, and Sediment Disturbance

Symbols are used to denote accessory lithologies, authigenic minerals, concretions, fossils, and coring-induced sediment disturbance (Fig. F4). Symbols are positioned near the location in the section where that

feature is observed. If the feature extends over an interval, the symbol appears centered on a vertical line to denote the extent of occurrence.

Color

Colors are determined qualitatively using Munsell Soil Color Charts (Munsell Color Company, 1994) and described immediately after cores are split in order to avoid color changes associated with drying and redox reactions. Colors for some chert and pumice fragments are identified using the Geological Society of America (GSA) color chart (Rock-Color Chart Committee, 1991). Munsell and GSA color names are provided in the color column on the barrel sheet, and the corresponding hue, value, and chroma data are provided with the remarks.

Sample Types

Sample material taken for shipboard sedimentologic and chemical analysis consisted of pore water whole rounds, micropaleontology samples, "toothpick" samples, smear slides, thin section billets, and discrete samples for XRD. Typically, four or five smear slides were made per core, one pore water sample was taken at a designated interval, and a micropaleontology sample was obtained from the core catcher of most cores. XRD samples were taken only where needed to assess the lithologic components. Additional samples were selected to better characterize lithologic variability within a given interval. Tables summarizing relative abundance of sedimentary components from the smear slides were generated using a spreadsheet program (Sliders).

Remarks

The written description for each core contains a brief overview of both major and minor lithologies present and notable features such as sedimentary structures and disturbances resulting from the coring process.

Sediment Classification

Lithologic names consist of a principal name based on composition, degree of lithification and/or texture as determined from visual description, and smear slide observations. For a mixture of components, the principal name is preceded by major modifiers (in order of increasing abundance) that refer to components making up >25% of the sediment. Minor components that represent between 10% and 25% of the sediment follow the principal name (after a "with") in order of increasing abundance. An unconsolidated sediment containing 30% nannofossils, 25% clay minerals, 20% foraminifers, 15% quartz silt, and 10% manganese nodules would be described as a clayey nannofossil ooze with manganese nodules, quartz silt, and foraminifers. Sedimentary components ranging from 10% to 25% are reflected in the sediment name in the description column as "with," but these components are not designated in the graphic lithology column. These naming conventions follow the ODP sediment classification scheme (Mazzullo et al., 1988), with the exception that during Leg 199 a separate "mixed sediment" category was not distinguished. During Leg 199 neritic and chemical sediments were not encountered, except as accessory minerals; therefore, these categories are not addressed below.

Granular sediments were subdivided on the basis of composition and abundance of different grain types estimated from visual examination of the core, smear slides, thin sections, and by shipboard measurements of carbonate content (see below) and shipboard XRD analyses (see below) (Fig. F5). In volcaniclastic sediments, the term ash (or tuff if lithified) is used in place of sand, whereas lapilli is used for granule and cobble size categories. Larger volcanic clasts (breccia) were not encountered, except for fragments of pumice, which are noted in each barrel sheet. Size divisions for grains are those of Wentworth (1922) (Fig. F6). Size-textural qualifiers were not used for pelagic sediment names (e.g., nannofossil clay implies that the dominant component is detrital clay rather than clay-sized nannofossils).

Terms that describe lithification vary depending upon the dominant composition as described below:

1. Sediments derived predominantly from calcareous, pelagic organisms (e.g., calcareous nannofossils and foraminifers): the lithification terms "ooze," "chalk," and "limestone" reflect whether the sediment can be deformed with a finger (ooze), can be scratched easily by a fingernail (chalk), or cannot be scratched easily (limestone).
2. Sediments derived predominantly from siliceous microfossils (diatoms, radiolarians, and siliceous sponge spicules): the lithification terms "ooze," "radiolarite/spiculite/diatomite," "porcellanite," and "chert" reflect whether the sediment can be deformed with a finger (ooze), cannot be easily deformed manually (radiolarite/spiculite/diatomite), or displays a glassy luster (chert). We use the term porcellanite as defined by Keene (1975) to describe a siliceous limestone/claystone that has a dull luster and is less hard and compact than chert. It may contain a mix of opal, quartz, clay minerals, and carbonate. Note that the terms "porcellanite" and "chert" do not imply crystallinity of the silica.
3. Sediments derived predominantly from siliciclastic material: if the sediment can be deformed easily with a finger, no lithification term is added and the sediment is named for the dominant grain size. For more consolidated material, the lithification suffix "-stone" is appended to the dominant size classification (e.g., "clay" vs. "claystone").
4. Sediments composed of sand-sized volcaniclastic grains: if the sediment can be deformed easily with a finger, the interval is described as ash. For more consolidated material, the rock is called tuff.

Color Reflectance Spectrophotometry

In addition to visual estimates of the color, reflectance of visible light from soft sediment cores was routinely measured using a Minolta spectrophotometer (model CM-2002) mounted on the AMST. The AMST measures the archive half of each core section and provides a high-resolution stratigraphic record of color variations for visible wavelengths (400–700 nm). Freshly split cores were covered with clear plastic wrap and placed on the AMST. Measurements were taken at 2.0-cm spacing. The AMST skips empty intervals and intervals where the core surface is well below the level of the core liner but does not recognize relatively small cracks or disturbed areas of core. Thus, AMST data may

F5. Ternary diagram showing nomenclature for principal components of whole-rock composition, p. 47.

F6. Grain-size divisions for sedimentary rocks, p. 48.

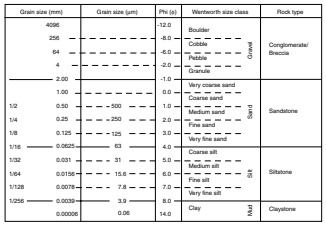

contain spurious measurements that should to the extent possible, be edited out of the data set before use. Each measurement recorded consists of 31 separate determinations of color reflectance in 10-nm-wide spectral bands from 400 to 700 nm. Additional detailed information about measurement and interpretation of spectral data with the Minolta spectrophotometer can be found in Balsam et al. (1997, 1998) and Balsam and Damuth (2000).

Core Curation and Shipboard Sampling of Igneous Rocks

To describe important mineralogic and structural features in both the archive and working halves, we examined core sections containing igneous rocks prior to cutting the core with a diamond-impregnated saw. Each piece was numbered sequentially from the top of the core section and labeled on the outside surface. Pieces that could be fit together were assigned the same number and lettered consecutively (e.g., 1A, 1B, 1C, etc.). Plastic spacers were placed between pieces with different numbers. The presence of a spacer may represent a substantial interval of no recovery. If it was evident that an individual piece had not rotated about a horizontal axis during drilling, an arrow was added pointing to the top of the section.

Visual Core Descriptions and Barrel Sheets for Igneous Rocks

The few fragments of basalt recovered during Leg 199 were described on the VCD forms for sediments.

XRD

Selected samples were taken for qualitative mineral analysis by using an XRD Philips model PW1729 X-ray diffractometer using Ni-filtered CuK_{α} radiation. Instrument conditions were as follows: 40 kV, 35 mA; goniometer scan from 2 to 70 °2θ (air-dried samples) and from 2 to 12 °2θ (glycolated samples); step size of 0.01 °2θ; scan speed at 1.2 °2θ/min; and count time of 0.5 s each.

Some samples were decalcified using 10% acetic acid then washed repeatedly with demineralized water in a centrifuge. The carbonate-free fraction was deflocculated with a 1% Calgon (sodium hexametaphosphate) solution and homogenized in a sonic dismembrator for 1 min. MacDiff software (version 4.1.1 PPC by Rainer Petschick) was used to display diffractograms, and identifications are based on multiple peak matches, using the mineral database provided with MacDiff. Diffractograms were peak corrected to match the calcite peak at 3.035 Å. In the absence of calcite, no peak correction was applied.

Digital Color Imaging

Systematic, high-resolution line-scan digital core images of the archive half of each core were obtained using the GEOTEK X-Y Imaging system (Geoscan II). This digital imaging system (DIS) collects digital images with three linescan charge coupled device arrays (1024 pixels each) behind an interference filter to create three channels (red, green, blue). The image resolution is dependent on the width of the camera

and core. The standard configuration for GEOSCAN II produces 300 dpi on an 8-cm-wide core with a zoom capability up to 1200 dpi on a 2-cm-wide core. Synchronization and track control are better than 0.02 mm. The dynamic range is 8 bits for all three channels. The Framestore Card has 48 MByte of onboard RAM for the acquisition of images with an ISA Interface card for personal computers. After cores were visually described, they were placed in the DIS and scanned. A spacer holding a neutral gray color chip and a label identifying the section was placed at the base of each section and scanned along with each section. Output from the DIS includes a Windows bitmap (.BMP) file and a Mr.Sid (.SID) file for each section scanned. The bitmap file contains the original data with no compressional algorithms applied, whereas the Mr. Sid files apply extensive compressional algorithms. Additional postprocessing of data was done to achieve a medium-resolution JPEG image of each section and a composite JPEG image (stored as a Microsoft PowerPoint slide) of each core, which is comparable to the traditional photographic image of each core. The JPEG image of each section was produced by an Adobe Photoshop batch job that opened the bitmap file, resampled the file to a width of 0.6 in (~15 mm) at a resolution of 300 pixels/in, and saved the result as a maximum-resolution JPEG. The DIS system was calibrated for black and white approximately every 12 hr. No significant change in this calibration was observed during Leg 199. For Sites 1215–1220, the lens aperture was reset whenever significant changes in core color were observed. The resetting of the lens aperture, however, resulted in undesirable side effects when compiling composite digital core images of multiple sections across critical boundaries; color changes in composite images were often the result of aperture changes, rather than changes in sedimentary characteristics, and overwhelmed true sediment color change. For Sites 1221 and 1222, a constant aperture setting of f11 was used. This resulted in underexposed images in some of the darker-colored intervals, which obscured some of the sediment features. These image files were adjusted for brightness and contrast using a suitable software application, such as Adobe Photoshop or Microsoft PowerPoint, before inclusion in the core composite images.

BIOSTRATIGRAPHY

Preliminary age assignments were based on biostratigraphic analyses of calcareous nannofossils, planktonic foraminifers, and radiolarians. Paleodepth interpretations were based on benthic foraminifers. Age constraints of calcareous nannofossil datums were determined by examining from one to six samples per section of core (sampling spacing of 1.5–0.25 m) as well as core catcher samples. Planktonic foraminifers were examined in one core sample per section (sampling density of ~1.5 m) in addition to core catcher samples. Efforts were focused on Hole A at multiply cored sites, allowing greater sampling density resulting in a more detailed shipboard planktonic foraminifer biostratigraphy to be developed. Benthic foraminifers were examined in core catcher samples from Hole A at each site. Radiolarians were examined in each core catcher, as well as in one sample from within each section of core. The preservation, abundance, and zonal assignment for selected samples and for each microfossil group were recorded in the stratigraphic site-summary sheets and entered into the Janus database.

Recognition of Critical Intervals

Much emphasis is placed on three critical intervals of the biostratigraphic determinations: the Eocene/Oligocene (E/O) boundary, the upper Eocene impact events, and the Paleocene/Eocene (P/E) boundary. Biostratigraphic indicators for each of these events are discussed below.

E/O Boundary

The lower Oligocene is zoned in most detail by calcareous nannofossils, although the E/O boundary is recognized by the last occurrence of the planktonic foraminifer genus *Hantkenina*. The E/O boundary is present within uppermost Chron C13r at the planktonic foraminifer Zone P16/P18 boundary and within the middle of calcareous nannofossil Subzone CP16a. We do not recognize planktonic foraminifer Zone P17 of Berggren et al. (1995a) because of taxonomic and preservational problems associated with identification of the last occurrence of *Cribrohantkenina inflata*. Calcareous nannofossil datum levels within 2 m.y. of the E/O boundary (33.7 Ma) include the base of *Reticulofenestra umbilicus* (31.7 Ma), the base of *Ericsonia formosa* (32.9 Ma), and the base of the acme of *Ericsonia subdisticha* (33.3 Ma). The acme of *Ericsonia obruta* (33.7 Ma) coincides with the E/O boundary. The presence of the planktonic foraminifer *Pseudohastigerina* (base 32.0 Ma) is considered a reliable datum for the lowermost Oligocene. The uppermost Eocene is easily determined by the presence of the calcareous nannofossils *Discoaster saipanensis* (top at 34.0 Ma) and *Discoaster barbadiensis* (top at 34.2 Ma) as well as the presence of planktonic foraminifers *Globigerinatheka* spp. (top at 34.3 Ma) and *Turborotalia cerroazulensis* (top at 33.8 Ma). The base of the *Theocyrtis tuberosa* radiolarian zone (RP20) has been approximated to 32.8 Ma (Sanfilippo and Nigrini, 1998).

Eocene Impact Horizons

The Eocene impact events occur within Subchron C16n.2n (~35.78 Ma) (Poag et al., in press), near the top of planktonic foraminifer Zone P15 and the lower third of calcareous nannofossil Zone CP15. There are four radiolarian events coincident with the horizon in middle latitudes (e.g., Leg 171B sites; Norris, Kroon, Klaus, et al., 1998). The four radiolarian markers are the simultaneous last occurrences of *Calocyclas turris, Cryptocarpium azyx, Thyrsocyrtis bromia,* and *Thyrsocyrtis rhizodon*. The same four extinctions occur approximately simultaneously in the tropics (Sanfilippo and Nigrini, 1998) but have not yet been formally linked with the Eocene impact event. The planktonic foraminifers *Turborotalia pomeroli* and *Globigerinatheka semiinvoluta* (reported top for both taxa; 35.3 Ma) (Berggren et al., 1995b) have extinction datums that are actually nearly coincident with the impact horizon (Norris, Kroon, Klaus, et al., 1998). The last occurrence of the calcareous nannofossil *Calcidiscus protoannulus* (35.4 Ma) slightly postdates the event. The first occurrence of the calcareous nannofossil *Chiasmolithus oamarensis* (37.0 Ma) and the last occurrence of *Chiasmolithus grandis* (37.1 Ma) are present below the impact level.

P/E Boundary

Global stratigraphic sections and points (GSSPs) have been established for the Pliocene/Pleistocene, Miocene/Pliocene, Oligocene/

Miocene, and E/O boundaries. A GSSP has not yet been established for the P/E boundary, which remains controversial and is discussed further here.

The P/E boundary has, until recently, been placed at the planktonic foraminifer Biozone P5/6 boundary, which is found in the middle part of calcareous nannofossil Zone NP10 (CP9a) (Aubry et al., 1996). In 2000, the International Geological Correlation Programme Project 308 membership *(Paleocene/Eocene Events in Space and Time)* voted to recognize the carbon isotope excursion (CIE) associated with the Paleocene–Eocene Thermal Maximum (PETM) as the defining criteria for identifying the P/E boundary. For Leg 199, we will adhere to this definition of the P/E boundary. The P/E boundary (as defined by the CIE) can be approximated by a series of calcareous microfossil datums. These events include a major extinction event among benthic foraminifers (including *Gavelinella beccariiformis, Aragonia velascoenis,* and *Osangularia velascoensis*) precisely at the boundary. The boundary can also be approximated by the presence of the planktonic foraminifer "excursion fauna" that includes *Acarinina africana, Acarinina sybiaensis,* and *Morozovella allisonensis* (Kelly et al., 1996, 1998). The planktonic foraminifers *Pseudohastigerina wilcoxensis* and large specimens of *Chiloguembelina wilcoxensis* also have first occurrences close to the boundary (Speijer, 1997). The interval, ~500–700 k.y. above the P/E boundary, is marked by the last occurrences of *Morozovella velascoensis* (marking the top of planktonic foraminifer Zone P5) and *Morozovella occlusa* as well as the first occurrences of *Morozovella gracilis* and *Acarinina wilcoxensis*. The extinction of the calcareous nannofossil genus *Fasciculithus* occurred during the CIE just above the boundary. The base of *Campylosphaera eodela* occurred shortly before the boundary, and the lineage *Rhomboaster-Tribrachiatus* evolved after the boundary. Thus, from a biostratigraphic point of view, the P/E boundary falls within planktonic foraminifer Biozone P5 and within calcareous nannofossil Biozone CP8b (NP9).

All these biostratigraphic events are present in the long interval of Chron 24r. According to our timescale (Cande and Kent, 1995), this interval of uniform reversed polarity has a duration of 2.557 m.y. Very few sites are known to have recovered continuous sedimentation with unambiguous magnetostratigraphy across this critical interval (Chron C24r), explaining some of the ongoing debate about age relationships in this long interval of uniform magnetic polarity. Recent cyclostratigraphic work (Norris and Röhl, 1999; Röhl et al., 2000) has shown that the CIE, and therefore the P/E boundary, occurred ~1 m.y. above the top of Chron C25n. Thus, it has an age of 55 Ma according to the Leg 199 timescale.

Hole 1051A (Leg 171B), in the western North Atlantic, is the only recovered P/E boundary section in which radiolarians have been studied (Sanfilippo and Blome, 2001). In this midlatitude fauna, many tropical zonal markers are missing, and others are diachronous with their tropical equivalents. There is no gross change in the composition of the fauna and only a minor increase in the number of first and last occurrences across the PETM and P/E boundary.

Sanfilippo and Nigrini (1998) established the stratigraphic sequence of the 70 lowest and highest radiolarian occurrences in a 10-m.y. interval spanning the P/E boundary from the Paleocene *Bekoma campechensis* Zone (RP6) to the upper part of the lower Eocene *Buryella clinata* Zone (RP8) and related them to the calcareous nannofossil zonation. Although none of their investigated tropical sequences contained the actual P/E boundary, they determined that there are six reliable, easily rec-

ognized, and potentially useful radiolarian lowest occurrences that approximate the P/E boundary. They are *Calocyclas castum, Theocotylissa auctor, Lamtonium fabaeforme, Podocyrtis (Podocyrtis) papalis, Giraffospyris lata,* and *Phormocyrtis turgida*.

Calcareous Nannofossil Zonal Scheme and Taxonomy

The zonal scheme of Bukry (1973, 1975) (zonal code numbers CN and CP added and modified by Okada and Bukry, 1980) was used for Cenozoic calcareous nannofossil biostratigraphy. These zonations represent a general framework for the biostratigraphic classification of mid- to low-latitude nannofossil assemblages and are presented in Figure **F7.** Ages and sources for Cenozoic calcareous nannofossil datums are presented in Table **T1.** The age estimates presented are all adjusted to the timescale of Leg 199. Martini's (1971) nannofossil zonation (NN and NP zones) are also shown for reference. Nannofossil taxonomy follows that of Perch-Nielsen (1985).

Planktonic Foraminiferal Zonal Scheme and Taxonomy

The tropical planktonic foraminiferal zonal scheme (N and P zones) for the Cenozoic follows Berggren et al. (1995b) and is illustrated in Figure **F7.** Ages and sources for Cenozoic planktonic foraminifer datums are presented in Table **T2.** Cenozoic taxonomic concepts selectively follow Postuma (1971), Kennett and Srinivasan (1983), Bolli and Saunders (1985), Toumarkine and Luterbacher (1985), Spezzaferri and Premoli Silva (1991), Chaisson and Leckie (1993), Leckie et al. (1993), Spezzaferri (1994), Pearson (1995), Berggren and Norris (1997), Chaisson and Pearson (1997), Pearson and Chaisson (1997), Norris (1998), and Olsson et al. (1999). Eocene planktonic foraminifer taxonomy is currently under revision by the Eocene Planktonic Foraminifer Working Group and is adopted here. Genus-species combinations generally follow those rules used by Berggren et al. (199b) with few modifications.

Benthic Foraminiferal Taxonomy and Paleodepth Determination

At suprageneric levels, the classification scheme of Loeblich and Tappan (1988) is followed. Cenozoic benthic foraminiferal taxonomic concepts were mainly based on Pflum et al. (1976), Tjalsma and Lohmann (1983), van Morkhoven et al. (1986), and Bolli et al. (1994) for Paleocene–Eocene species.

Paleodepth estimates are based on van Morkhoven et al. (1986):

Neritic = <200 m.
Bathyal = 200–2000 m.
Abyssal = >2000 m.

Radiolarian Zonal Scheme and Taxonomy

Leg 199 radiolarian biostratigraphy was based largely on the radiolarian zonation and code numbers that were tied to the geomagnetic polarity timescale (GPTS) of Cande and Kent (1995) and documented by Sanfilippo and Nigrini (1998). Supplemental markers, also derived from Sanfilippo and Nigrini (1998), are used whenever possible and are corre-

F7. Correlation chart for 0–65 Ma, p. 49.

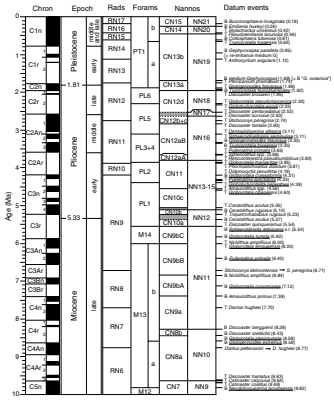

T1. Age estimates of calcareous nannofossil datum events, p. 56.

T2. Age estimates of planktonic foraminifer datum events, p. 58.

lated with the data supplied by calcareous nannofossils. Primary and supplemental datums are listed in Table T3 and illustrated in Figure F7.

T3. Age estimates of radiolarian datum events, p. 61.

Methods of Study for Calcareous Nannofossils

Calcareous nannofossils were examined in smear slides using standard, light-microscope techniques under crossed nicols and transmitted light at 1000× magnification. The following abbreviations were used to describe nannofossil preservation:

- G = good preservation (little or no evidence of dissolution and/or recrystallization; diagnostic characters fully preserved).
- M = moderate preservation (dissolution and/or secondary overgrowth; partially altered primary morphological characteristics; most specimens were identifiable to the species level).
- P = poor preservation (severe dissolution, fragmentation, and/or overgrowth; primary morphological characteristics largely destroyed; specimens often could not be identified at the species and/or generic level).

Five calcareous nannofossil abundance levels are recorded as follows:

- A = abundant (the taxonomic category constitutes >10% of the total assemblage).
- C = common (the taxonomic category makes up from 1% to 10% of the total assemblage).
- F = few (the taxonomic category makes up from 0.1% to <1% of the total assemblage).
- R = rare (the taxonomic category constitutes <0.1% of the total assemblage).
- B = barren.

Methods of Study for Foraminifers

Foraminifers from unlithified ooze were soaked in a 3% solution of hydrogen peroxide (with a small amount of Calgon added), warmed on a hot plate, then washed with tap water over a 63-µm sieve. Semilithified ooze and chalk were first partially fragmented by hand then soaked in hydrogen peroxide and Calgon before washing. Each sieve was dipped in a dilute solution of methyl blue dye to identify contaminants from previous samples. All samples were dried in a low-temperature oven at ~50°C. Species identification for planktonic foraminifers were generally made on the >250-µm and >150-µm size fractions, whereas two picking trays per sample from the >125-µm fraction were examined for benthic foraminiferal identification and abundance estimation because benthic foraminifers were found to be extremely few.

The following abundance categories were estimated from visual examination of the dried sample for planktonic and benthic foraminifers:

- D = dominant (>30%).
- A = abundant (10%–30%).
- F = few (5%–<10%).
- R = rare (1%–<5%).
- P = present (<1%).
- B = barren.

The preservation status of the planktonic and benthic foraminifers was estimated as follows:

VG = very good (no evidence of overgrowth, dissolution, or abrasion).
G = good (little evidence of overgrowth, dissolution, or abrasion).
M = moderate (calcite overgrowth, dissolution, or abrasion were common, but minor).
P = poor (substantial overgrowth, dissolution, or fragmentation).

Methods of Study for Radiolarians

Core catcher samples were disaggregated by gentle boiling in a solution of 10% H_2O_2 and ~5 g of tetrasodium pyrophosphate. The solution was sieved through a 63-µm sieve. Calcareous components were dissolved by adding a 10% solution of hydrochloric acid and sieving again. A strewn slide was prepared by pipetting the microfossils onto a microscope slide, allowing the water to evaporate, adding a drop or two of xylene and some Canada balsam to the slide, and covering the slide with a 22 mm × 40 mm glass coverslip.

Overall radiolarian abundances were determined based on strewn-slide evaluation at 100×, using the following convention:

A = abundant (>100 specimens per slide traverse).
C = common (51–100 specimens per slide traverse).
F = few (11–50 specimens per slide traverse).
R = rare (1–10 specimens per slide traverse).
T = trace (<1 specimen per slide traverse).
B = barren (no radiolarians in sample).

The abundance of individual species was recorded relative to the fraction of the total assemblages as follows:

A = abundant (>10% of the total assemblage).
C = common (5%–10% of the total assemblage).
F = few (<5% of the total assemblage).
R = rare (a few or more specimens per slide).
T = trace (present in slide).
B = barren (absent).

Preservation was recorded as follows:

G = good (majority of specimens complete, with minor dissolution, recrystallization, and/or breakage).
M = moderate (minor but common dissolution, with a small amount of breakage of specimens).
P = poor (strong dissolution, recrystallization, or breakage, many specimens unidentifiable).

PALEOMAGNETISM

Paleomagnetic investigations during Leg 199 focused mainly on measurements of the natural remanent magnetization (NRM) and alternating-field (AF) demagnetization of archive-half core, and on detailed

measurements of discrete samples. Discrete samples were collected during the cruise from working halves of core sections from Hole A at each site in standard (8 cm^3) cubic plastic boxes. The sampling frequency was generally two samples per section. About 30% of the samples were demagnetized on board; the rest of them will be analyzed on shore to help determine the mineralogy and grain size of the magnetic minerals, complement the shipboard magnetic stratigraphy, and confirm the paleolatitude of the studied sites.

Instrumentation

Remanent magnetization was measured using the shipboard 2G Enterprises (model 760R) long-core cryogenic magnetometer equipped with direct-current superconducting quantum interference devices (DC SQUIDs) and an in-line, automated AF demagnetizer capable of reaching a peak field of 80 mT. Continuous core measurements were made at 5-cm intervals with 10-cm-long headers and trailers. The response curve from the sensor coils of the cryogenic magnetometer, however, is ~12 cm wide; therefore, measurements taken every 5 cm are not completely independent from each other. Measurements at core and section ends and within intervals of drilling-related core disturbance were not measured or were removed during data processing. The background noise of the instrument seems to be amplified by the ship's movement compared to shore-based instruments, and it was estimated to be ~5×10^{-5} A/m assuming a measured volume of ~100 cm^3. The relatively large volume of core material within the sensing region compensates for the relatively high background noise, and with very few exceptions, the sediment magnetization was well above the instrumental noise level.

The standard ODP coordinate system was used, where +x is the vertical upward direction when the core is on its side, +y is the direction to the right along the split-core surface when looking upcore, and +z is the downcore direction. AF demagnetization on the archive halves was performed routinely with the in-line AF demagnetizer at typical fields of up to 20 mT in order to avoid compromising future shore-based paleomagnetic studies.

Magnetic field measurements taken in the AF coil region of the magnetometer have shown two prominent leaks in the magnetic shielding at the points where the magnetic shields are bolted together. This results in peak fields of ~30,000 nT directed along the z-axis of the magnetometer, which might produce a spurious anhysteretic remanent magnetization (ARM) during AF demagnetization. To check for potential problems, we tested the in-line demagnetizer by comparing the results with those obtained using the onboard D-tech apparatus (D-2000). The test that was conducted on discrete samples using a relatively high field (up to 80 mT) suggested that there are not any major differences in the results obtained with the two instruments; therefore, the faster in-line demagnetizer was used for all subsequent samples.

The Schonstedt Demagnetizer (model TSD-1) was used to test thermal demagnetization on a set of discrete samples from Hole 1215A, but this technique was not routinely used as it was more time consuming compared to use of the in-line AF demagnetizer.

The orientations of APC cores were recorded using the Tensor tool (Tensor Inc., Austin, Texas). The instrument has a three-axis fluxgate magnetometer that records the orientation of the double lines scribed on the core liner with respect to magnetic north. The critical parameters for core orientation are the inclination angle (typically <2°) and the

angle between magnetic north and the double line on the core liner, known as the magnetic toolface (MTF) angle. The Tensor tool readings were recorded continuously at 30-s intervals, downloaded to a computer, and analyzed once the tool was back on deck. Orientation of cores is of particular importance in paleomagnetic studies of equatorial regions, where the paleomagnetic inclination is close to zero. Unfortunately we encountered some difficulties in using the MTF angle, and some cores had to be reoriented by aligning the paleomagnetic declination to north. Though the reference paleomagnetic direction for the Paleogene is a few degrees to the east, this assumption is acceptable for our magnetostratigraphic purposes.

Measurements and Procedures

Measurements of NRM and stepwise AF demagnetization were performed on all archive halves and discrete samples taken from the working halves. More than 10,000 runs were carried out on the shipboard magnetometer. After some tests at 5, 10, 15, 20, 25, and 30 mT, most core sections were demagnetized at 5, 10, 15, and 20 mT or 7, 15, and 20 mT depending on core flow in the laboratory. Because AF demagnetization of the archive half was conducted mostly to remove the soft magnetic overprint that was acquired during the drilling process, field strengths were limited to 20 mT to avoid erasing the entire primary NRM component. Most of the discrete samples were fully demagnetized using the in-line AF demagnetizer in fields of up to 80 mT.

Site paleolatitudes for the Neogene and Paleogene are important goals of Leg 199, and this makes the characteristic remanent magnetization (ChRM) inclinations an important target in the paleomagnetic study, especially in discrete samples. ChRM can be potentially contaminated by a spurious ARM acquired in the magnetometer due to the presence of a small DC field around the AF demagnetizing coils. Because this DC field is directed along the z axis (horizontal and parallel to the long axis of the magnetometer) the ARM would directly affect the inclination. To avoid this potential problem we chose to measure the discrete samples with the samples' –z axis directed along the magnetometer's x axis and the samples' +x axis directed along the magnetometer's z axis. Using this configuration, a possible ARM acquired along the magnetometer's z axis would mostly affect the declination but would preserve the inclination of the ChRM. The correct coordinate system of the sample magnetization was restored after the measurement using a simple Perl script or an Excel spreadsheet.

We have taken two different approaches to estimate site paleolatitude. When discrete samples were available, we used standard Fisher statistics to compute a mean declination and inclination and the corresponding paleolatitude assuming a dipole field. Limited time between sites reduced the number of discrete samples that could be analyzed, so the long-core data were also used to calculate mean magnetic inclination. From the core data we discarded all samples with virtual geomagnetic pole (VGP) latitudes smaller than ±45° to remove possible transitional, spurious, and partially isolated primary magnetization directions. We then grouped them by age in large data sets. Although less precise than discrete samples, the latitudes computed from core data comprise a very large data set (often larger than 1000 measurements), and we believe that such a redundancy compensates for the lower quality of the long-core data compared to discrete samples data.

Magnetostratigraphy

The magnetic polarity was calculated using VGP latitudes. Whenever possible, we offer an interpretation of the magnetic polarity, with the naming convention following that of correlative anomaly numbers prefaced by the letter C (Tauxe et al., 1984). Normal polarity subchrons are referred to by adding suffixes (n1, n2) that increase with age. For the younger part of the timescale (Pliocene–Pleistocene) we often use the traditional names to refer to the various chrons and subchrons (e.g., Brunhes, Jaramillo). In general, polarity reversals occurring at core ends have been treated with extreme caution and always double-checked with overlapping records from parallel holes. Occasionally, the polarity of paleomagnetic directions for cores taken from higher-latitude holes (Sites 1215 and 1216) was assigned by using inclination-only data from continuous core measurements. At paleoequatorial sites (all the remaining sites) and, in general, for sediments older than late Oligocene, however, this was not possible, and we combined the data from parallel holes to find the best match of both polarity assignment and core orientation. This left a minor uncertainty in core orientation, which was typically resolved by using the orientation of the present-day field overprint as revealed by progressive demagnetization in discrete samples. The same procedure was used to retrieve the orientation of samples taken from nonoriented XCB cores.

The ages of the polarity intervals used in Leg 199 are a composite of four previous magnetic polarity timescales. We used Shackleton et al.'s (1990) astronomically tuned timescale for the interval between 0 and 2.6 Ma, Hilgen's (1991a, 1991b) astronomically tuned timescale for the interval between 2.6 and 5.23 Ma, Shackleton et al.'s (1995b, table 17) partially astronomically tuned timescale for the interval between 5.23 and 14.8 Ma, and Cande and Kent's (1995) seafloor spreading–based timescale for ages older than 14.8 Ma. These four separate timescales are compatible and should not introduce artificial discontinuities in the calculated sedimentation rates. This composite timescale approach was developed by Curry, Shackleton, Richter, et al. (1995) and subsequently adopted by Berggren et al. (1995b). The absolute ages that make up the Leg 199 magnetic polarity timescale are summarized in Table **T4.**

T4. Magnetic polarity timescale used during Leg 199, p. 65.

COMPOSITE DEPTHS

The scientific objectives of Leg 199 require the examination of the sedimentary record at high resolution as well as the recovery of a geological record that is as complete as possible. Core recovery from a single hole is insufficient to accomplish these goals because of recovery gaps between adjacent cores, even with a nominal 100% recovery. To obtain a complete sedimentary record, multiple adjacent holes are cored, with an offset in depth of typically 2–4 m between different holes to ensure that intervals missing within a single APC-cored hole can be recovered from an adjacent hole. The offset in depth required in subsequent holes must rapidly be determined before and during coring. The continuity of recovery is assessed by developing composite sections that align prominent features in physical properties data from adjacent holes. The procedure and rationale for this stratigraphic correlation is described in this section and follows the methodology pioneered during Legs 94 (Ruddiman et al., 1987) and 138 (Hagelberg et al., 1992). Similar methods were employed and developed further during Legs 154

(Curry, Shackleton, Richter, et al., 1995), 162 (Jansen, Raymo, Blum, et al., 1996), 167 (Lyle, Koizumi, Richter, et al., 1997), 171B (Norris, Kroon, Klaus, et al., 1998), and other more recent ODP legs such as 189 (Exon, Kennett, Malone, et al., 2001).

Data Employed for Stratigraphic Correlation

Onboard stratigraphic correlation requires closely spaced data that can be generated rapidly. After each whole-core section had equilibrated to room temperature (typically 4–5 hr), it was run through the MST assemblage (see **"MST Measurements,"** p. 23, in "Physical Properties"). The MST generates high-resolution (2-cm interval) measurements of MS, GRA wet bulk density, and *P*-wave velocity. The MST data set also comprises less closely spaced (20-cm interval) measurements of natural gamma ray (NGR) emissions, which are typically less useful for correlation work. In addition, measurements of color reflectance in the 400- to 700-nm band and calculated L*a*b* values were made at 2-cm resolution on the split archive half of the core using a Minolta spectrophotometer (see **"Color Reflectance Spectrophotometry,"** p. 6, in "Lithostratigraphy"). All measurements were entered into the shipboard database.

Composite Section Development

By convention, ODP sample and core depths are recorded as mbsf from the first core in each hole that shows a true mudline, and consecutive depth measurements are determined by the length of the drill string. Several factors can lead to a deviation of the relative distance of geological features in the core from their true in situ stratigraphic separation. For example, sediment inside the core can expand as a result of reduced environmental pressure following core recovery, leading to an expanded sedimentary sequence relative to its original length (Moran, 1997). Thus, sediment can be missing between cores, even if a nominal 100% recovery is achieved. In addition, variations in the ship motion, tides, and heave can result in stretching and/or squeezing of the recovered sediment in particular subintervals.

To allow the placement of geological data from different holes according to their stratigraphic position, a correlation of physical properties measurements is made to create a meters composite depth (mcd) scale. The generation of an mcd scale attempts to match coeval stratigraphic features, as recorded by the MST and color reflectance measurements, at the same level by generating a composite record from different holes. This process requires depth shifting of cores relative to each other. During this step, the total length on the mcd scale is typically expanded by 10% compared to the mbsf scale, although this factor can vary between ~5% and 15% (Hagelberg et al., 1992; Norris et al., 1998).

Hole-to-hole correlation was facilitated by using the graphical and interactive UNIX platform software, SPLICER, that was developed by Peter deMenocal and Ann Esmay of the Lamont-Doherty Earth Observatory Borehole Research Group (LDEO-BRG). We used version 2.2 of this software (available on the World Wide Web at **www.ldeo.columbia.edu/BRG/ODP**). SPLICER allows data sets from adjacent holes to be correlated simultaneously, making use of an interactive, cross-correlation computation. After prominent features are aligned on the new mcd scale, a "spliced" record can be generated by switching holes to avoid core gaps or disturbed sediment, resulting in a

continuous record that forms the basis for further sampling and analysis.

In addition to creating a high-resolution shipboard record for time-series analysis, one of the primary purposes of the composite depth scale is the generation of a template that forms the basis for sediment sampling along a complete section with a minimal waste of samples and analytical time. For this reason, it is highly desirable to apply a constant offset to an entire core, such that the depth increments along individual cores on the mcd scale are linearly related to the curated mbsf depth increments. The SPLICER software only allows the application of a constant offset for each core.

However, composite depth scales created by using the SPLICER method are usually not satisfactory to create a stacked record from different holes because not every individual feature present across different holes can be aligned. Hence, if the aim is to increase the signal-to-noise ratio of quasiperiodic cycles that might be recorded in the sedimentary record, it would be necessary to allow stretching and squeezing within individual sections to align data from different holes on the individual cycle level. The procedure for the generation of a common depth scale that allows stretching and squeezing on a fine level was pioneered by Hagelberg et al. (1995) and results in a revised mcd common depth scale. The generation of revised mcd scales is typically carried out as part of postcruise work.

In detail, the composite depth generation using SPLICER begins by assigning the core with the best record of the upper few meters of a hole as the top of the composite record. This core is assigned an mcd identical to its mbsf depth. A tie point, which gives the preferred correlation, is selected between data from this first core and a core in a second hole. All the data from the second hole below the correlation point are vertically shifted to align the tie points between the holes. After choosing an appropriate tie point and adjusting the depths, the shifted section becomes the next "reference" section, and a tie is made to a core from the first hole. Working downhole in an iterative fashion, each core is then vertically shifted. The tie points are added to the SPLICER "affine" table (which records all the depth adjustments that define composite depth scale) in units of mcd. The affine table that relates mbsf to mcd values along with the applied linear offsets for each core is presented in tabular form in the "Composite Depths" section of each site chapter. The composite depth table of Site 1218 is given as an example in Table **T5.** The last two columns in each table give, for each core, the cumulative depth offset added to the ODP curatorial sub-bottom depth (in mbsf) and the composite depth (in mcd), respectively. The depth offset column allows the calculation of the equivalent depth in mcd by adding the amount of offset listed to the depth in mbsf of a sample taken in a particular core. Table **T6** shows a typical example for the SPLICER file that defines the switching across holes to generate a spliced composite section. The composite depth and splice tie point tables from each site chapter are also presented in ASCII (see the **"ASCII Tables"** contents list).

Figure **F8** illustrates how the creation of a composite record allows the alignment of the most prominent lithology features. In the left panel, MS data from three holes at Site 1218 are shown on the mbsf depth scale, whereas in the middle panel the data are shown on a common depth (mcd) scale. The right panel shows the generated spliced record, indicating where the sample track was switched from one hole to the next. If the available data only allow an ambiguous or imprecise

T5. Example of composite depth table, p. 66.

T6. Example of splice tie points table, p. 67.

F8. MS data, Site 1218, p. 53.

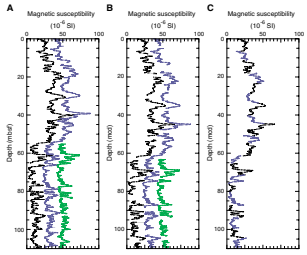

correlation, or where multiple hole data were unavailable, no additional depth adjustments were made. In this case, the cumulative offset remains constant for all subsequent cores below.

Splice tie points were made between adjacent holes at identifiable, highly correlated features, attempting to construct the splice crossover points at transitions rather than peaks. Each splice was constructed beginning at the mudline at the top of the composite section and working downward. Typically, one hole was chosen as the backbone for the record, and cores from other holes are used to patch in the missing intervals in core gaps (Fig. F8). Intervals were chosen for the splice such that section continuity was maintained, whereas disturbed intervals were avoided.

The final alignment of the adjacent holes could be slightly different from the best overall visual or quantitative hole-to-hole correlation because of the constraint that a constant offset be applied to each core by the SPLICER software. Thus, in addition to creating an additional revised mcd scale for time-series analysis and other studies that require the stacking of data from multiple holes, investigators intend to rescale the spliced record to downhole logging data (Harris et al., 1995) as part of postcruise studies. Although the difference between the lengths of the mcd and mbsf scale will not normally be significant as far as uncertainties in geological flux calculations are concerned, this rescaling process would be required for some studies (e.g., the calibration of seismic studies that make use of physical properties measurements).

SEDIMENTATION AND ACCUMULATION RATES

To determine sedimentation rates, we must first generate an age-depth relationship. At a site with precisely determined paleomagnetic stratigraphy and with unambiguously identified chrons, accumulation rate uncertainties arise almost entirely from uncertainties in the ages and depths of reversal boundaries.

The chief uncertainty with shipboard biostratigraphic data arises from the fact that the samples that constrain the datums may be widely separated in depth. During many ODP legs, it has been necessary to reconstruct sedimentation rates using datums determined only in core catchers (i.e., within 9.5 m). The amount of uncertainty in each sedimentation-rate estimate derived in this way is related to the thickness interval over which it is averaged, divided by the combined uncertainty in the top and bottom controls. The second source of uncertainty in sedimentation rates is the age of the datums. Our aim is to use a primary set of datums, distributed <2 m.y. apart, and to determine these datums in all sites to within one section (1.5 m) or better. Where available, we have used paleomagnetic stratigraphy as our primary age control. Nannofossil datums serve as a very good backup to this stratigraphy. Other fossil groups, such as radiolarians, primarily serve as checks on stratigraphy until the ages of these biostratigraphic events are better calibrated using data from this leg.

Sedimentation rates (meters per million years) may be estimated from age-depth plots either by drawing best-fit lines through all the biostratigraphic and paleomagnetic data over successive depth intervals or by drawing straight-line segments. Inspection of the distribution of other datums about the lines suggests that it might be difficult to rigorously justify one approach vs. another, especially given the difficulty of evaluating the uncertainties in the accuracy of each datum. Age-depth

plots give more direct evidence for or against rapid changes in sedimentation rates that might otherwise be artificially exaggerated by using best-fit lines through discrete intervals of data. All sedimentation rates were calculated using midpoints in the observed depth uncertainty range. In reality, each datum event has an age uncertainty that may vary from a few thousand years to a few hundred thousand years.

Bulk-sediment mass accumulation rates (MARs) (grams per square centimeters per thousand years) are calculated by multiplying linear sedimentation rate data and dry bulk density (DBD) data (in grams per cubic centimeters). The MAR of the bulk sediment was calculated for every depth where a bulk density value was measured by the onboard physical properties program. When elemental concentration data was available, the bulk MAR value was multiplied by the weight percent of an element to produce elemental MARs.

GEOCHEMISTRY

Interstitial Water Sampling and Chemistry

Shipboard interstitial water analyses were performed on 5-cm-long whole-round sections that were cut immediately after the core arrived on deck. In most cases, one whole-round section was taken from the middle of each core for the first six cores and every third core thereafter. To avoid the potential destruction of critical intervals, whole-round sections were not removed from cores adjacent to such intervals as determined by shipboard biostratigraphy. Details of the sampling resolution are described in the individual site chapters. After extrusion from the core liner, the surface of each whole-round section was scraped with a spatula to remove potential contamination. Interstitial waters were collected using a titanium squeezer, modified after the standard ODP stainless steel squeezer of Manheim and Sayles (1974). Pressure up to 205 MPa (30,000 psi) was applied using a hydraulic press. Pore waters were passed through prewashed Whatman No. 1 filters fitted above a titanium screen and subsequently extruded into a plastic syringe attached to the bottom of the squeezer assembly. All interstitial water samples were double-filtered through 0.45-µm polycarbonate filters. Samples for shipboard analysis were stored in plastic vials pending analysis. Aliquots for future shore-based analyses were placed in glass ampules and heat sealed. Aliquots for shore-based analysis of interstitial water $\delta^{13}C$ were poisoned with a saturated mercuric chloride solution (50 µL mercuric chloride solution to 1 mL interstitial water sample).

Interstitial water samples were routinely analyzed for salinity as total dissolved solids with a Goldberg optical handheld refractometer. The pH and alkalinity (Alk) were determined by Gran titration with a Brinkmann pH electrode and a Metrohm autotitrator. Dissolved chloride was determined by titration with silver chloride (AgCl). Sodium (Na^+), potassium (K^+), magnesium (Mg^{2+}), calcium (Ca^{2+}), and sulfate (SO_4^{2-}) were analyzed by ion chromatography using a Dionex DX-120 ion chromatograph. Silica ($Si[OH]_4$), phosphate (HPO_4^{2-}), and ammonium (NH_4^+) concentrations were determined by spectrophotometric methods (Gieskes et al., 1991) using a Milton Roy Spectronic 301 spectrophotometer and a Milton Roy Mr. Sipper sample introduction system. After phosphate values were found to be below detection limit for the first site, samples were no longer analyzed for phosphate. Manganese (Mn^{2+}), lithium (Li^+), strontium (Sr^{2+}), barium (Ba^{2+}), and boron (B) con-

centrations were determined by inductively coupled plasma–atomic emission spectroscopy (ICP-AES) following the general procedure outlined by Murray et al. (2000). In preparation for analysis by ICP-AES, aliquots of interstitial waters were acidified with nitric acid (HNO_3) and diluted tenfold with deionized (DI) water (0.5 mL of sample and 4.5 mL of DI water). Analytical blanks were prepared identically by analyzing DI water, which was acidified to matrix match the samples. At all sites, sodium was determined using charge balance calculations, where

$$[Na^+] = [Alk] - [K^+] - 2 \times [Mg^{2+}] - 2 \times [Ca^{2+}] + [Cl^-] + 2 \times [SO_4^{2-}]$$

(Broecker and Peng, 1982). The chemical data for interstitial waters are reported in molar units. The reproducibility of results, determined via multiple determinations of the International Association for the Physical Sciences of the Ocean standard seawater (alkalinity, Cl^-, Ca^{2+}, Mg^{2+}, K^+, and SO_4^{2-}), spiked synthetic seawater (ICP-AES determinations), or through the use of a calibration curve (NH_4^+, HPO_4^{2-}, and $Si[OH]_4$), is available in Table T7. Initially during Leg 199, reproducibility on interstitial water ICP-AES determinations (Mn^{2+}, Li^+, Sr^{2+}, and Ba^{2+}) was compromised because of analytical problems associated with the baffled spray chamber used for interstitial water ICP-AES. An unbaffled spray chamber more efficiently delivers the sample in the instrument, yields better reproducibility, and is normally used for interstitial water ICP-AES determinations. However, during Leg 199 the only available unbaffled spray chamber was sequestered for bulk-sediment ICP-AES determinations and could not be used for interstitial water analysis, because of concern over the possible contamination of the interstitial waters with lithium metaborate ($LiBO_2$) flux from the bulk-sediment analyses. For these reasons, once the bulk-sediment analyses for Leg 199 were complete, we cleaned the unbaffled spray chamber with ~10% HNO_3 and repeated the interstitial water program for Mn^{2+}, Li^+, Sr^{2+}, Ba^{2+}, and B for all samples. These repeat analyses are the ones that we report. The chemistry lab aboard the *JOIDES Resolution* now carries two unbaffled spray chambers to circumvent the above problems.

T7. Analytical determination reproducibility, p. 68.

Bulk-Sediment Sampling and Chemistry

For the first time, bulk-sediment samples were analyzed routinely during Leg 199. Samples for bulk sediments were taken at a frequency of one sample per section (1.5 m) for Sites 1215–1217. To conserve shipboard argon (used in record quantity during Leg 199) samples were taken at a frequency of three samples per core (1.5 m; Sections 2, 4, and 6) for Sites 1218–1222. For future application of a shipboard bulk-sediment geochemistry program of this magnitude, we recommend significantly increasing the shipboard argon supply. All samples were taken adjacent to physical properties samples so that MARs can be calculated using concentration and bulk density measurements taken as close together as possible.

Bulk samples were prepared according to the method of Murray et al. (2000). Samples were first freeze dried and crushed. Samples and standards (0.1 g) were mixed with $LiBO_2$ flux (0.4 g). Analytical blanks were prepared using 0.4 g $LiBO_2$ flux to ensure matrix matching. A solution of 0.172-mM LiBr wetting agent (10 µL) was added to the samples, standards, and blanks. This mixture was fused for 15 min at 1050°C in a NT-2100 Bead Sampler prior to dissolution in 50 mL of 10% HNO_3. The

supply of platinum crucibles (12) for fusing was a significant limit on sample throughput. A 5-mL aliquot of the resulting solutions was filtered (0.45 µm) and diluted with 35 mL of 10% HNO_3, resulting in a 4000× dilution of the original powders. Si, Al, Ti, Fe, Mn, Ca, Mg, P, Sr, and Ba concentrations were determined using a Jobin-Yvon Ultrace ICP-AES using a type C Meinhard concentric nebulizer following the general procedure outlined by Murray et al. (2000). We chose to report major element sediment concentrations in weight percent (Si, Al, Ti, Fe, Mn, Ca, Mg, and P) and minor element concentrations in parts per million (Sr and Ba) because sediments are composed of a mixture of minerals that are not usually in equilibrium. Reproducibility of results for Sites 1215–1221 is available in Table **T7.** We found at Site 1222 that excessive ship motion during transit or on station affected instrument drift and weighing accuracy enough to significantly degrade precision (e.g., from 11.5% to 34.2% for Ca, 14.7% to 85.4% for Sr, and 3.3% to 21.8% for Si). Therefore, we do not report results for Site 1222 and we recommend that during future legs these analyses not be run in heavy seas or during transit.

Sediment samples (at least one per core, on a split of one of the bulk-sediment samples) were analyzed for calcium carbonate ($CaCO_3$ in weight percent) using a Coulometrics 5011 carbon dioxide coulometer and for total carbon using a Carlo Erba 1500 CNS analyzer. Organic carbon (in weight percent) was calculated as the difference between total carbon and carbonate carbon. $CaCO_3$ was also calculated from Ca (in weight percent) determined by ICP-AES. The following equation (Dymond et al., 1976) was used:

$$CaCO_3 = \{[Ca - (0.41 \times S) - 0.73]/39.31\} \times 100,$$

where,

$CaCO_3$ = calcium carbonate (weight percent) in the sample.
Ca = calcium (weight percent) in the sample.
S = the weight fraction of salt in the sample from physical properties calculations (see **"Physical Properties,"** p. 23).

We compared $CaCO_3$ values calculated from Ca determined by ICP-AES to $CaCO_3$ values measured by coulometer (Fig. **F9**). $CaCO_3$ values calculated from Ca contents yielded similar trends to $CaCO_3$ measured via coulometer. However, absolute values by calculation are lower than by coulometer when $CaCO_3$ is <1 wt% and higher when $CaCO_3$ is >1 wt%. Values by calculation sometimes yield negative values because the normative calculation assumes an aluminosilicate calcium contribution of 0.7 wt%. Scatter is higher when $CaCO_3$ values are >75 wt%. The discrepancy in higher values is probably due to a combination of factors, including the error on Ca measurements determined by ICP-AES (±11.5 wt%; see Table **T7**) and the fact that the highest Ca standard available for the ICP-AES calcium standard calibration curve was 35.9 wt%, equivalent to a value of 90 wt% $CaCO_3$. Any reported calcium values >35.9 wt% should, therefore, be considered suspect and are flagged in this report. In the future, to alleviate this problem, we recommend using a 40 wt% Ca (100 wt% $CaCO_3$) standard in the ICP-AES Ca standard calibration curve.

F9. $CaCO_3$ determined by ICP-AES and coulometer analyses, p. 54.

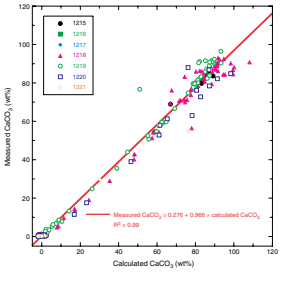

PHYSICAL PROPERTIES

Shipboard measurements of physical properties provide information that assists in characterization of lithologic units, correlation of lithology with downhole geophysical logging data, assessment of the consolidation history, and interpretation of seismic reflection profiles. The primary objectives of the Leg 199 physical properties program were to collect high-resolution data to: (1) provide bulk density data for determination of mass accumulation rates, (2) facilitate hole-to-hole and site-to-site correlation and construction of composite stratigraphic sections, (3) enable postcruise cyclostratigraphy studies, (4) facilitate construction of synthetic seismic profiles, and (5) investigate the characteristics of major seismic reflectors.

Physical properties were measured on whole-round sections and undisturbed parts of split cores. Nondestructive measurements of wet bulk density, MS, transverse compressional wave (*P*-wave) velocity, and natural gamma radiation were made on whole-round sections using the MST. The MST incorporates a GRA bulk density device, a *P*-wave logger (PWL), a MS meter, and a natural gamma radiation sensor. Thermal conductivity, using the needle-probe method, was measured on whole-round sections. Compressional wave velocity and moisture and density (MAD) measurements were made on split-core sections. Bulk properties determined by MAD analyses included wet bulk density, DBD, grain density, water content, and porosity. Light absorption spectroscopy (LAS) analyses were performed on all MAD samples as well as an additional one sample per section. Prior to the whole-round measurements, the cores were allowed to come to thermal equilibrium at ambient room temperature (i.e., 20°–22°C) to ensure thermal homogeneity for the physical properties measurements. A comprehensive discussion of all methodologies and calculations used in the *JOIDES Resolution* physical properties laboratory can be found in Blum (1997).

In situ temperature measurements were made using the Adara temperature tool as part of regular APC coring operations. These data were combined with measurements of thermal conductivity to calculate heat flow.

MST Measurements

The principal aim of MST data acquisition during Leg 199 was to obtain high sampling resolution data sets, especially of GRA bulk density and MS, to facilitate shipboard core-to-core correlation and the construction of composite stratigraphic sections. This objective had to be completed within a reasonable time frame without compromising the shipboard processing of recovered core. The quality of the MST data is highly dependent on the condition of the core.

The measurement of wet bulk density by the GRA system is based on the principle that the attenuation, mainly by Compton scattering, of a collimated beam of gamma rays produced by a ^{137}Ce source passing through a known volume of sediment is related to material density (Evans, 1965). Calibration of the GRA system was completed using known seawater/aluminum density standards. GRA bulk density data are of highest quality when determined on APC cores because the liner is generally completely filled with sediment. In XCB cores, GRA measurements are of lower quality and typically cannot be used to reliably determine bulk density on their own. The measurement width of the

GRA sensor is ~5 mm, with sample spacing generally set at 4.0 cm for Leg 199 cores. The minimum integration time for a statistically significant GRA measurement is 1 s, and routine Leg 199 GRA measurements used either a 3- or 5-s integration time. A freshwater control was run with each section to measure instrument drift.

Whole-core MS was measured with the MST using a Bartington MS2 meter coupled to a MS2C sensor coil with an internal diameter of 8.8 cm operating at 565 Hz. The measurement resolution of the magnetic susceptibility motion sensor is 4 cm, with a minimum statistically significant count time of 1 s. During Leg 199, MST MS was routinely measured at a spacing of 2.0 cm, with five data acquisitions. MS data were archived and are displayed as raw instrument units (SI) and are not corrected for changes in sediment volume (for details see Blum, 1997) although a correction was made for instrument drift.

Transverse *P*-wave velocity was measured on the MST track with the PWL for all APC cores. The use of the PWL on XCB cores was limited by poor acoustic coupling between the sediment and the core liner. The PWL transmits a 500-kHz compressional wave pulse through the core at 1 kHz. The transmitting and receiving transducers are aligned perpendicular to the core axis, and a pair of displacement transducers monitors the separation between the compressional wave transducers. Variations in the outer diameter of the liner do not degrade the accuracy of the velocities, but the unconsolidated sediment or rock core must completely fill the liner for the PWL to provide acoustic coupling, which is often not the case with XCB cores. Calibration of the displacement transducer and measurement of electronic delay within the PWL circuitry were conducted using a series of acrylic blocks of known thickness and *P*-wave traveltime. Repeated measurement of *P*-wave velocity through a core liner filled with distilled water was used to check calibration validity. The measurement width of the PWL sensor is ~1 mm, with sample spacing routinely set at 2.0 cm for Leg 199 APC cores.

NGR emissions of sediments are a function of the random and discrete decay of radioactive isotopes, predominantly those of U, Th, and K, and are measured through scintillating detectors arranged 90° to each other and perpendicular to the core. The installation and operating principles of the NGR system used on the *JOIDES Resolution* are discussed by Hoppie et al. (1994). Data from 256 energy channels were collected and archived. For presentation purposes, the counts were summed over the range of 200–3000 keV, so as to be comparable with data collected during previous legs. This integration range also allows direct comparison with downhole logging data, which were collected over a similar integration range (Hoppie et al., 1994). Over the 200- to 3000-keV integration range, background counts, measured using a core liner filled with distilled water, averaged 30 cps during a 1-hr measurement period. Before taking measurements, each of the four NGR amplifiers were adjusted so that the Th peak was at the highest resolution possible when the other three amplifiers were disabled. The multichannel analyzer was then calibrated by assigning certain channels to the characteristic energies of ^{40}K and the main peak of ^{232}Th (Blum, 1997). The measurement width of the NGR is ~15 cm, with a statistically significant count time of at least 5 s, depending on lithology. Because of the long time required for NGR measurements, sample spacing and count time for NGR measurements varied depending on the age and lithology of the sediment recovered. No corrections were made to NGR data obtained from XCB cores to account for sediment incompletely filling the core liner.

Thermal Conductivity

The thermal conductivity was measured with the TK04 (Teka Bolin) system using the needle-probe method in full-space configuration for soft sediments (Von Herzen and Maxwell, 1959). The needle probe contains a heater wire and calibrated thermistor. It is assumed to be a perfect conductor because it is much more conductive than unconsolidated sediments. With this assumption, the temperature of the superconductive probe has a linear relationship with the natural logarithm of the time after the initiation of the heat:

$$T(t) = (q/4\pi k) \times \ln(t) + C,$$

where,

T = temperature,
q = heat input per unit length per unit time,
k = thermal conductivity,
t = the time after the initiation of the heat, and
C = a constant.

The thermal conductivity was measured by inserting the needle into the unconsolidated sediment through a small hole drilled into the core liner. Three measuring cycles were automatically performed at each sampling location and used to calculate an average conductivity. A self-test, which included a drift study, was conducted at the beginning of each cycle. Once the samples were equilibrated, the heater circuit was closed and the temperature rise in the probes was recorded. Thermal conductivities were calculated from the rate of temperature rise while the heater current was flowing. Temperatures measured during the first 150 s of the heating cycle were fitted to an approximate solution of a constantly heated line source (for details see Kristiansen, 1982, Blum, 1997). Measurement errors were 5%–10%. At sites where in situ temperatures were measured, thermal conductivity was corrected for in situ temperature and pressure as part of the calculation of heat flow. Thermal conductivity measurements were taken with a frequency of one per core in soft sediments, into which the TK04 needles could be inserted without risk of damage.

MAD Analysis

Wet and DBD, grain density, water content, and porosity were determined from measurements of wet sediment mass, dry sediment mass, and dry sediment volume. In soft sediments, samples of ~10 cm^3 were extracted and placed in 10-mL beakers. Stiff sediments drilled with the XCB were cut into cubes using the dual-bladed diamond saw and placed in 50-mL beakers or processed without beakers. One sample was routinely collected in each section from Hole A. Samples were taken in subsequent holes when gaps in Hole A needed to be filled.

Sample mass was determined to a precision of 0.01 g using two Scientech 202 electronic balances and a computer averaging system to compensate for the ship's motion. Sample volumes were determined using a Quantachrome penta-pycnometer (a helium-displacement pycnometer) with a precision of 0.02 cm^3. Volume measurements were repeated five times until the last two measurements exhibited <0.01% standard devi-

ation. A reference volume was included within each sample set and rotated sequentially among the cells to check for instrument drift and systematic error. A purge time of 3–5 min was used before each run. Sample beakers used for discrete determination of moisture and density were calibrated before the cruise. Dry mass and volume were measured after samples were heated in an oven at 105° ± 5°C for 24 hr and allowed to cool in a desiccator. The procedures for the determination of these properties comply with the American Society for Testing and Materials (ASTM) designation (D) 2216 (ASTM, 1990). Blum (1997) discusses the fundamental phase relations and assumptions for the calculations of all relevant phase relationships summarized below.

Mass and Volume Calculation

Wet mass (M_{wet}), dry mass (M_{dry}), and dry volume (V_{dry}) are measured in the laboratory. Salt precipitated in sediment pores during the drying process is included in the M_{dry} and V_{dry} values. The mass of the evaporated water (M_{water}) and the salt (M_{salt}) in the sample are given by

$$M_{water} = M_{wet} - M_{dry} \text{ and}$$

$$M_{salt} = M_{water}\,[s/(1 - s)],$$

where s = the assumed saltwater salinity (0.035) corresponding to a pore water density (ρ_{pw}) of 1.024 g/cm³ and a salt density (ρ_{salt}) of 2.257 g/cm³. The corrected mass of pore water (M_{pw}), volume of pore water (V_{pw}), mass of solids excluding salt (M_{solid}), volume of salt (V_{salt}), volume of solids excluding salt (V_{solid}), and the wet volume (V_{wet}) are, respectively,

$$M_{pw} = M_{water} + M_{salt} = M_{water}/(1 - s),$$

$$V_{pw} = M_{pw}/\rho_{pwt},$$

$$M_{solid} = M_{dry} - M_{salt},$$

$$V_{salt} = M_{salt}/\rho_{salt},$$

$$V_{solid} = V_{dry} - V_{salt} = V_{dry} - M_{salt}/\rho_{salt}, \text{ and}$$

$$V_{wet} = V_{solid} + V_{pw}.$$

Calculation of Bulk Properties

For all sediment samples, water content (w) is expressed as the ratio of the mass of pore water to the wet sediment (total) mass,

$$w = M_{pw}/M_{wet}.$$

Wet bulk density (ρ_{wet}), DBD (ρ_{dry}), sediment grain (solid) density (ρ_{solid}), and porosity (ϕ) are calculated from

$$\rho_{wet} = M_{wet}/V_{wet},$$

$$\rho_{dry} = M_{solid}/V_{wet},$$

$$\rho_{solid} = M_{solid}/V_{solid}, \text{ and}$$

$$\phi = V_{pw}/V_{wet}.$$

LAS

LAS studies were conducted on the MAD sample residues as well as an additional one sample per section (located ~50 cm from the MAD sample). The ~10-cm³ samples were heated in an oven at 105° ± 5°C for 24 hr and allowed to cool in a desiccator. Samples need to be dry, otherwise water completely dominates the spectral signature. Samples were then crushed for improved analyses. Light reflectance, at a bandwidth of 350–2500 nm, was found for each sample using the FieldSpec Pro FR portable spectroradiometer. Semiquantitative mineral concentrations were then calculated from the collected spectra, assuming a four-component system: calcite, opal, smectite, and illite. For a complete description of the LAS technique and calibration methods, refer to **Vanden Berg and Jarrard,** this volume.

Compressional Wave Velocity

Velocity was measured on split-core sections using the PWS1 and PWS2 insertion probe system in soft sediments and the PWS3 contact probe system in firm sediments and rocks. The insertion probe system allows measurement of the longitudinal (perpendicular to bedding) *P*-wave velocity (PWS1) and the transverse *P*-wave velocity (PWS2). The contact probe system (PWS3) measures the transverse velocity across the split-core section and core liner or across samples taken from the cores. In both systems, the compressional wave velocity calculation is based on the accurate measurement of the delay time of a 500-kHz square wave signal traveling between a pair of piezoelectric transducers. Transducer separations of PWS1 and PWS2 are fixed at 6.96 and 3.48 cm, respectively. The transducer pair for PWS3 is adjusted to the thickness of the core half or extracted sample. The separation of the fixed lower PWS3 transducer and the movable, upper transducer is measured by a linear voltage-displacement transducer. Prior to measuring velocity on samples from each hole, the PWS1 and PWS2 transducers were calibrated by inserting the probes in a container of distilled water of known temperature and measuring the traveltime. The PWS3 transducers were calibrated using the linear regression of traveltime vs. distance for a set of Lucite standards.

Routine sampling frequency for *P*-wave measurements was one per section. The positions of the *P*-wave measurements are next to those for MAD analyses. Deionized water was added to the contact between the transducers and sample to improve acoustic coupling when needed. The core temperature was recorded at the time velocity was measured; however, the velocity data stored in the Janus database are uncorrected for in situ temperature and pressure. These corrections can be made using the relationships outlined in Wyllie et al. (1956), Wilson (1960), and Mackenzie (1981).

Velocity anisotropy was calculated where both longitudinal and transverse compressional wave velocity were measured. Anisotropy is determined from the difference between the average horizontal and vertical velocity using the following equation:

$$\text{Anisotropy} = 2 \times (V_{pt} - V_{pl})/(V_{pt} + V_{pl}),$$

where,

V_{pt} = average transverse compressional wave velocity and
V_{pl} = longitudinal velocity.

In Situ Temperature Measurements

The Adara tool was used to obtain in situ sediment temperature measurements during APC coring operations. The components of the Adara tool are contained in an annulus in the coring shoe of the APC string and include a platinum temperature sensor and a data logger. The platinum resistance temperature is calibrated over a range of 0°–100°C with a resolution of 0.01°C. During operation, the coring shoe is attached to a core barrel and lowered down the pipe by wireline. The tool is typically held for 5–10 min at the mudline to equilibrate with bottom-water temperatures and is then lowered to the end of the drill string. The standard APC coring technique is subsequently used, with the core barrel fired through the drill bit using hydraulic pressure. The Adara tool is left in the sediment for 10–15 min to obtain a temperature record. These data provide a sufficiently long transient record for reliable extrapolation of the steady-state temperature. The nominal accuracy of the Adara temperature measurement is ±0.1°C.

Data reduction for the Adara tool estimates the steady-state, bottom-hole temperature by forward modeling the recorded transient temperature curve as a function of time. The shape of the transient temperature curve is determined by the response function of the tool and the thermal properties of the bottom-hole sediment (Bullard, 1954; Horai and Von Herzen, 1985). A synthetic curve is constructed based on the tool geometry, sampling interval, and the properties of the tool and surrounding sediments. It is difficult to obtain a perfect match between the synthetic curves and the data because (1) the probe never reaches thermal equilibrium during the penetration period; (2) contrary to theory, the frictional pulse upon insertion is never instantaneous; and (3) temperature data are sampled at discrete intervals, which means that the exact time of penetration is always uncertain. As a result, both the effective penetration time and equilibrium temperature must be estimated by applying a fitting procedure that involves shifting the synthetic curves in time to obtain a match with the recorded data.

Heat Flow Calculation

Heat flow was determined by the Bullard method, as outlined by Pribnow et al. (2000). This method assumes a linear relation between the temperature (T) and thermal resistance (Ω) of the sediments:

$$T(z) = T_0 + q\Omega(z),$$

where,

z = depth,
T_0 = surface temperature ($z = 0$),
q = heat flow, and

$$\text{thermal resistance} = \Omega(z) = \int_0^z dz/\lambda(z) \approx \sum_{i=1}^{I} (z_i - z_{i-1})/\lambda_i$$

with z_i and z_{i-1} bottom and top depths, respectively, of a horizontal layer with thermal conductivity (λ_i). The number of layers between the surface and depth (z) is I. Heat flow is calculated by plotting $\Omega(z)$ vs. $T(z)$ (the Bullard plot) and using linear regression to determine q from the slope of the best-fit line. Determination of thermal resistance depends on the downhole variation in thermal conductivity, which varies as a function of lithology at the Leg 199 sites. Radiolarian-rich sediments are characterized by nearly constant thermal conductivity, and an average value was used for determination of thermal resistance. Clays and nannofossil oozes typically display a downhole decrease in porosity and increase in thermal conductivity, which was modeled using the assumption of a linear increase in conductivity with depth. Because thermal conductivity is dependent on temperature and pressure, laboratory conductivity measurements were corrected for the appropriate in situ conditions using the correction of Hyndman et al. (1974):

$$\lambda_{P,T}(z) = \lambda_{lab} \times \{1 + (z_w + \rho z)/1829 \times 100 + [T(z) - T_{lab}]/4 \times 100\},$$

where,

$\lambda_{P,T}(z)$ = in situ thermal conductivity at depth z (mbsf),
λ_{lab} = thermal conductivity measured in the lab,
z_w = water depth,
ρ = mean sediment density (in grams per cubic centimeter),
$T(z)$ = in situ temperature, and
T_{lab} = sample temperature during the conductivity measurement.

DOWNHOLE MEASUREMENTS

Downhole logs are used to determine physical, chemical, and structural properties of the formation penetrated by a borehole. The data are rapidly collected, continuous with depth, and, most importantly, are measured in situ. Logs may be interpreted in terms of the stratigraphy, lithology, mineralogy, and geochemical composition of the penetrated formation. Where core recovery is good, log and core data are complementary and should be integrated and interpreted jointly; where core recovery is incomplete or disturbed, log data may provide the only means to characterize the borehole section.

Downhole logs are sensitive to formation properties on a scale that is intermediate between those obtained from laboratory measurements on core samples and geophysical surveys. They are useful in calibrating the interpretation of geophysical survey data (e.g., through the use of synthetic seismograms) and provide a necessary link for the integrated understanding of physical properties on all scales. Wireline logging was scheduled for three of the eight sites. Unfortunately, because of lack of time only two holes were logged (Holes 1218A and 1219A).

Wireline Logging

Measurements are obtained using a variety of Schlumberger and LDEO logging tools combined into several tool strings, which are deployed in the hole after coring operations are completed. Standard time

estimates had to be revised during this leg as a result of the installation of a new wireline that had to be "seasoned," which doubled run times into and out of the holes. Two wireline tool strings were used during Leg 199.

1. The triple combination (triple combo) tool string consisting of resistivity (phasor dual induction tool [DIT]), bulk density (hostile environment litho-density tool [HLDT]), gamma ray (hostile environment natural gamma sonde [HNGS]), and porosity (accelerator porosity sonde [APS]) components, and two additional LDEO tools that measured high-resolution gamma ray (multisensor gamma ray tool [MGT]) and high-resolution temperature/acceleration/pressure tool (TAP tool); and
2. The Formation MicroScanner (FMS)-sonic tool string consisting of microresistivity (FMS), sonic velocity (dipole shear sonic imager [DSI]), gamma ray (natural gamma ray tool [NGT]), and orientation/acceleration (general purpose inclinometer tool [GPIT]) components.

Natural gamma radiation tools were included on both tool strings to provide a common reference for correlation and depth shifting between multiple logging runs. Further tool details are given in Figure **F10** and Table **T8.**

Each tool string contains a telemetry cartridge facilitating communication from the tools along the wireline (seven conductor cable) to the Schlumberger minimum configuration MAXIS (MCM) unit located on the ship. The ship's heave motion is a further complication in the acquisition of quality wireline logging data. To overcome this complication, the wireline is fed over the wireline heave compensator (WHC). As the ship heaves in the swell, an accelerometer located near the ship's center of gravity measures the movement and feeds the data, in real time, to the WHC. The WHC responds to the ship's heave by adding or removing cable slack to decouple the movement of the ship from the toolstring (Goldberg, 1990).

During each logging run, incoming data are recorded and monitored in real time on the MCM logging computer. The tool strings are pulled up at constant speed to provide continuous measurements as a function of depth. The MGT is not a Schlumberger tool and cannot record data while the Schlumberger tools are active. Thus, the MGT requires separate passes for data acquisition, during which time control of the wireline transfers to the LDEO logger and data are recorded, in real time, on the specialized acquisition system in the downhole measurements laboratory (DHML).

Logged Sediment Properties and Tool Measurement Principles

The main logs acquired by the tools are listed in Table **T9.** A brief description of the measurement methods and the logged properties is given below. More detailed information on individual tools and their geological applications may be found in Ellis (1987), Goldberg (1997), Lovell et al. (1998), Rider (1996), Schlumberger (1989, 1994), and Serra (1984, 1986, 1989).

F10. Schematic illustration of tool strings, p. 55.

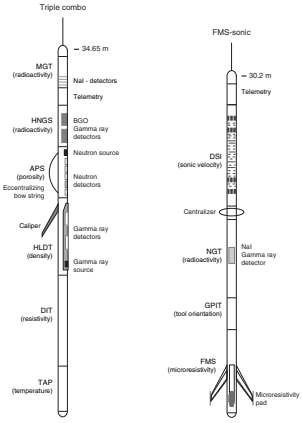

T8. Deployed logging tools, p. 69.

T9. Logging tool acronyms and units, p. 70.

Natural Radioactivity

Three wireline spectral gamma ray tools were used (one for each tool run) to measure and classify natural radioactivity in the formation: the NGT, the HNGS, and the MGT. The NGT uses a sodium iodide (NaI) scintillation detector and five-window spectroscopy to determine concentrations of K (percent), Th (parts per million), and U (parts per million), the three elements whose isotopes dominate the spectrum of natural radiation. The HNGS is similar to the NGT but uses two bismuth germanate scintillation detectors for significantly improved tool precision. It also filters out gamma ray energies below 500 keV, eliminating sensitivity to bentonite or KCl in the drilling mud and improving measurement accuracy. Although the NGT response is sensitive to borehole diameter and the weight and concentration of bentonite or KCl present in the drilling mud, corrections for these effects are routinely made during processing at LDEO.

The MGT was developed by the LDEO-BRG to improve the vertical resolution of NGR logs by using an array of four short detector modules with ~2-ft spacing. Each module comprises a small 2 in × 4 in NaI detector, a programmable 256-channel amplitude analyzer, and an ^{241}Am calibration source. The spectral data are subsequently recalculated to determine the concentration of K, Th, and U radioisotopes or their equivalents. The spectral data from individual modules are sampled 4 times/s and stacked in real time based on the logging speed. This approach increases vertical resolution by a factor of 2–3 over conventional tools while preserving comparable counting efficiency and spectral resolution. The radius of investigation depends on several factors: hole size, mud density, formation bulk density (denser formations display a slightly lower radioactivity), and the energy of the gamma rays (a higher energy gamma ray can reach the detector from deeper in the formation). The MGT also includes an accelerometer channel to improve data stacking by the precise measurement of logging speed. Postcruise processing may correct for borehole size and tool sticking using the acceleration data.

Density

Formation density was determined with the HLDT. The tool contains a radioactive cesium (^{137}Cs) gamma ray source (622 keV) and far and near gamma ray detectors mounted on a shielded skid, which is pressed against the borehole. Gamma rays emitted by the source undergo Compton scattering, which involves the transfer of energy from gamma rays to the electrons in the formation via elastic collisions. The number of scattered gamma rays that reach the detectors is directly related to the density of electrons in the formation that is in turn related to bulk density. Porosity may also be derived from this bulk density if the matrix (grain) density is known.

The HLDT also measures photoelectric absorption as the photoelectric effect (PEF). Photoelectric absorption of the gamma rays occurs when they reach <150 keV after being repeatedly scattered by electrons in the formation. As the PEF depends on the atomic number of the elements in the formation, it also varies according to the chemical composition of the minerals present. For example, the PEF of calcite = 5.08 b/e^-, illite = 3.03 b/e^-, quartz = 1.81 b/e^-, and kaolinite = 1.49 b/e^-. Good contact between the tool and borehole wall is essential for acquisition

of quality HLDT logs; poor contact results in an underestimation of density values.

Porosity

Formation porosity was measured with the APS. The sonde incorporates a minitron neutron generator (which produces fast neutrons [14.4 MeV]) and five neutron detectors (four epithermal and one thermal) positioned at differing intervals from the minitron. The measurement principle involves counting neutrons that arrive at the detectors after being slowed by neutron absorbers surrounding the tool. The highest energy loss occurs when neutrons collide with hydrogen nuclei that have practically the same mass as the neutron (the neutrons simply bounce off heavier elements without losing much energy). If the hydrogen (i.e., water) concentration is small, as in low-porosity formations, neutrons can travel farther before being captured, and the count rates increase at the detector. The opposite effect occurs when the water content is high. However, because hydrogen bound in minerals such as clays or in hydrocarbons also contributes to the measurement, the raw porosity value is often an overestimate.

Upon reaching thermal energies (0.025 eV), the neutrons are captured by the nuclei of Cl, Si, B, and other elements resulting in a gamma ray emission. This neutron capture cross section (S_f) is also measured by the tool.

Electrical Resistivity

The DIT was used to measure electrical resistivity. The DIT provides three measures of electrical resistivity each with a different depth of investigation into the formation. The two induction devices (deep and medium depths of penetration) transmit high-frequency alternating currents through transmitter coils, creating magnetic fields that induce secondary currents in the formation. These currents produce a new inductive signal, proportional to the conductivity of the formation that is measured by the receiving coils. The measured conductivities are then converted to resistivity. For the shallow penetration resistivity, the current necessary to maintain a constant voltage drop across a fixed interval is measured; it is a direct measurement of resistivity. Sand grains and hydrocarbons are electrical insulators, whereas ionic solutions and clays are conductors. Electrical resistivity can therefore be used to evaluate porosity (via Archie's Law) and fluid salinity.

Temperature, Acceleration, and Pressure

Downhole temperature, acceleration, and pressure were measured with the TAP tool. It was attached to the bottom of the triple combo tool string and run in memory mode with the data stored in built-in memory. The data were downloaded in the DHML after the logging run was complete and the TAP tool was removed from the Schlumberger tools.

The tool has a dual-temperature measurement system for identification of both rapid temperature fluctuations and temperature gradients. A thin fast-response thermistor detects small, abrupt changes in temperature, and the thicker slow-response thermistor more accurately estimates temperature gradients and thermal regimes. A pressure transducer is used to activate the tool at a specified depth, typically 200 m

above seafloor. A three-axis accelerometer measures tool movement downhole, which provides data for analyzing the effects of heave on the deployed tool string. The long-term accumulation and analysis of these data, under varying cable lengths and heave conditions, will lead to enhanced performance of the WHC. Also, the acceleration log can aid in deconvolving heave effects postcruise and it has proven at times to provide critical data.

The temperature record must be interpreted with caution because the elapsed time between the end of drilling and the logging operation is generally not sufficient to allow the borehole to reach thermal equilibrium following circulation of the drilling fluid. The data recorded under such circumstances may differ significantly from the thermal equilibrium of that environment. Nevertheless, it is possible to identify abrupt temperature changes that may represent localized fluid flow into the borehole indicative of fluid pathways and fracturing and/or breaks in the temperature gradient that may correspond to contrasts in permeability at lithologic boundaries.

Acoustic Velocity

The DSI measures the transit times between sonic transmitters and an array of eight receivers. It averages replicate measurements, thus providing a direct measurement of sound velocity through sediments that is relatively free from the effects of formation damage and borehole enlargement (Schlumberger, 1989). The tool contains the monopole transmitters found on most sonic tools, but also has two crossed dipole transmitters, providing shear wave velocity measurements in addition to the compressional wave velocity measurements, even in the slow formations typically encountered during some ODP legs.

FMS

The FMS provides high-resolution electrical resistivity–derived images of borehole walls. The tool has four orthogonal arms with pads, each containing 16 button electrodes that are pressed against the borehole wall during the recording (Fig. **F10**). The electrodes are arranged in two diagonally offset rows of eight electrodes. A focused current is emitted from the button electrodes into the formation, with a return electrode near the top of the tool. The intensity of current passing through the button electrodes is measured. Processing transforms these measurements, which reflect the microresistivity variations of the formation into continuous, spatially oriented, high-resolution images that map the geologic structures of the borehole wall. Further processing can provide measurements of dip and direction (azimuth) of structural features in the formation.

The development of the FMS tool has added a new dimension to wireline logging (Luthi, 1990; Lovell et al., 1998; Salimullah and Stow, 1992). Features such as bedding, fracturing, slump folding, and bioturbation can be resolved, and spatially oriented images allow fabric analysis and bed orientations to be measured.

The maximum extension of the caliper arms is 15 in, so in holes or parts of holes with larger diameter the pad contact will be inconsistent and the FMS images may appear out of focus and too conductive. Irregular borehole walls will also adversely affect the image quality if they lead to poor pad-wall contact.

Accelerometry and Magnetic Field Measurement

Three-component acceleration and magnetic field measurements were made with the GPIT. The primary purpose of this tool, which incorporates a three-component accelerometer and a three-component magnetometer, is to determine the acceleration and orientation of the FMS-sonic tool string during logging. This provides a means of correcting the FMS images for irregular tool motion, allowing the true dip and direction (azimuth) of structures to be determined.

Log Data Quality

The principal influence on log data quality is the condition of the borehole wall. If the borehole diameter is variable over short intervals, resulting from washouts during drilling, clay swelling, or ledges caused by layers of harder material, the logs from those tools that require good contact with the borehole wall (i.e., FMS, density, and porosity tools) may be degraded. Deep investigation measurements such as resistivity and sonic velocity, which do not require contact with the borehole wall, are generally less sensitive to borehole conditions. Very narrow ("bridged") sections will also cause irregular log results. The quality of the borehole is improved by minimizing the circulation of drilling fluid while drilling, flushing the borehole to remove debris, and logging as soon as possible after drilling and hole conditioning are completed.

Log Depth Scales

The depth of the wireline-logged measurement is determined from the length of the logging cable played out at the winch on the ship. The seafloor is identified on the natural gamma log by the abrupt reduction in gamma ray count at the water/sediment boundary (mudline). The coring depth (driller's depth) is determined from the known length of the bottom hole assembly and pipe stands. The mudline is usually recovered in the first core from the hole.

Discrepancies between the driller's depth of recovered core and the wireline log depth occur because of core expansion, incomplete core recovery, incomplete heave compensation, drill pipe stretch in the case of drill pipe depth, cable stretch (~1 m/km) and cable slip in the case of log depth. Tidal changes in sea level will also have an effect. In order to minimize the wireline tool motion caused by ship heave, the WHC adjusts for rig motion during wireline logging operations. The small but significant differences between drill pipe depth and logging depth should be taken into account when using the logs for correlation between core and log data. Core measurements, such as susceptibility and density, can be correlated with the equivalent downhole logs using the Sagan program, which allows shifting of the core depths onto the log depth scale. Precise core-log depth matching is difficult in zones where core recovery is low because of the inherent ambiguity of placing the recovered section within the cored interval.

Logs from different wireline tool strings will have slight depth mismatches. Distinctive features recorded by the natural gamma tool, run on every tool string, provide relative depth offsets and a means of depth shifting for correlation between logging runs.

Data Recording and Processing

Data for each logging run were recorded, stored digitally, and monitored in real time using the MCM software. On completion of logging at each hole, data were transferred to the DHML for preliminary interpretation. Basic processing was conducted postcruise to provide scientists with a comprehensive, quality-controlled downhole logging data set that can be used for comparison, integration, and correlation with other data collected during Leg 199 and other ODP legs. The processing includes depth adjustments to remove depth offsets between data from different logging runs, corrections specific to certain tools and logs, documentation for the logs (with an assessment of log quality), and conversion of the data to a widely accessible format (ASCII for the conventional logs and GIF for the FMS images). Schlumberger GeoQuest's GeoFrame software package is used for most of the processing.

Processed acoustic, caliper, density, gamma ray, magnetic, neutron porosity, resistivity, and temperature data in ASCII format are available (see the **"Related Leg Data"** contents list).

Core-Log-Seismic Integration

The IESX seismic interpretation software package was used to display site survey seismic sections acquired prior to Leg 199. Velocity and density logs were used to create synthetic seismograms, which were overlaid on the seismic section and used to refine the depth-traveltime relation. In this way, lithostratigraphic units in the core are correlated with reflectors and sequences in the seismic section.

REFERENCES

ASTM, 1990. Standard method for laboratory determination of water (moisture) content of soil and rock. *Annual Book of ASTM Standards* (Vol. 04.08): Philadelphia (Am. Soc. Testing and Mater.), D 2216–90 (revision of 2216–63, 2216–80).

Aubry, M.-P., Berggren, W.A., Stott, L., and Sinha, A., 1996. The upper Paleocene–lower Eocene stratigraphic record and the Paleocene/Eocene boundary carbon isotope excursion: implications for geochronology. *In* Knox, R.W.O'B., Corfield, R.M., and Dunay, R.E. (Eds.), *Correlation of the Early Paleogene in Northwestern Europe.* Spec. Publ.—Geol. Soc. Am., 101:353–380.

Backman, J., 1986. Late Paleocene to middle Eocene calcareous nannofossil biochronology from the Shatsky Rise, Walvis Ridge and Italy. *Palaeogeogr., Palaeoclimatol., Palaeoecol.,* 57:43–59.

————, 1987. Quantitative calcareous nannofossil biochronology of middle Eocene through early Oligocene sediment from DSDP Sites 522 and 523. *Abh. Geol. Bundesanst. (Austria),* 39:21–31.

Backman, J., and Raffi, I., 1997. Calibration of Miocene nannofossil events to orbitally tuned cyclostratigraphies from Ceara Rise. *In* Shackleton, N.J., Curry, W.B., Richter, C., and Bralower, T.J. (Eds.), *Proc. ODP, Sci. Results,* 154: College Station, TX (Ocean Drilling Program), 83–99.

Backman, J., Schneider, D.A., Rio, D., and Okada, H., 1990. Neogene low-latitude magnetostratigraphy from Site 710 and revised age estimates of Miocene nannofossil datum events. *In* Duncan, R.A., Backman, J., Peterson, L.C., et al., *Proc. ODP, Sci. Results,* 115: College Station, TX (Ocean Drilling Program), 271–276.

Balsam, W.L., and Damuth, J.E., 2000. Further investigations of shipboard vs. shore-based spectral data: implications for interpreting Leg 164 sediment composition. *In* Paull, C.K., Matsumoto, R., Wallace, P., and Dillon, W.P. (Eds.), *Proc. ODP, Sci. Results,* 164: College Station, TX (Ocean Drilling Program), 313–324.

Balsam, W.L., Damuth, J.E., and Schneider, R.R., 1997. Comparison of shipboard vs. shore-based spectral data from Amazon-Fan cores: implications for interpreting sediment composition. *In* Flood, R.D., Piper, D.J.W., Klaus, A., and Peterson, L.C. (Eds.), *Proc. ODP, Sci. Results,* 155: College Station, TX (Ocean Drilling Program), 193–215.

Balsam, W.L., Deaton, B.C., and Damuth, J.E., 1998. The effects of water content on diffuse reflectance measurements of deep-sea core samples: An example from ODP Leg 164 sediments. *Mar. Geol.,* 149:177–189.

Berggren, W.A., Hilgen, F.J., Langereis, C.G., Kent, D.V., Obradovich, J.D., Raffi, I., Raymo, M.E., and Shackleton, N.J., 1995a. Late Neogene chronology: new perspectives in high-resolution stratigraphy. *Geol. Soc. Am. Bull.,* 107:1272–1287.

Berggren, W.A., and Norris, R.D., 1997. Biostratigraphy, phylogeny and systematics of Paleocene trochospiral planktic foraminifera. *Micropaleontology, Suppl. 1,* 43:1–116.

Berggren, W.A., Kent, D.V., Swisher, C.C., III, and Aubry, M.-P., 1995b. A revised Cenozoic geochronology and chronostratigraphy. *In* Berggren, W.A., Kent, D.V., Aubry, M.-P., and Hardenbol, J. (Eds.), *Geochronology, Time Scales and Global Stratigraphic Correlation.* Spec. Publ.—Soc. Econ. Paleontol. Mineral., 54:129–212.

Blum, P., 1997. Physical properties handbook: a guide to the shipboard measurement of physical properties of deep-sea cores. *ODP Tech. Note,* 26 [Online]. Available from World Wide Web: <http://www-odp.tamu.edu/publications/tnotes/tn26/INDEX.HTM>. [Cited 2001-09-02].

Bolli, H.M., Beckmann, J.-P., and Saunders, J.B., 1994. *Benthic Foraminiferal Biostratigraphy of the South Caribbean Region:* Cambridge (Cambridge Univ. Press).

Bolli, H.M., and Saunders, J.B., 1985. Oligocene to Holocene low latitude planktic foraminifera. *In* Bolli, H.M., Saunders, J.B., and Perch-Nielsen, K. (Eds.), *Plankton Stratigraphy:* Cambridge (Cambridge Univ. Press), 155–262.

Broecker, W.S., and Peng, T.-H., 1982. *Tracers in the Sea:* Palisades, New York (El Digio Press).

Bukry, D., 1973. Low-latitude coccolith biostratigraphic zonation. *In* Edgar, N.T., Saunders, J.B., et al., *Init. Repts. DSDP,* 15: Washington (U.S. Govt. Printing Office), 685–703.

————, 1975. Coccolith and silicoflagellate stratigraphy, northwestern Pacific Ocean, Deep Sea Drilling Project Leg 32. *In* Larson, R.L., Moberly, R., et al., *Init. Repts. DSDP,* 32: Washington (U.S. Govt. Printing Office), 677–701.

————, 1991. Paleoecological transect of western Pacific Ocean, late Pliocene coccolith flora: Part 1. Tropical Ontong-Java Plateau at ODP 806B. *Open-File Report—US Geol. Surv.,* 91-552:1–35.

Bullard, E.C., 1954. The flow of heat through the floor of the Atlantic Ocean. *Proc. R. Soc. London A,* 222:408–429.

Cande, S.C., and Kent, D.V., 1995. Revised calibration of the geomagnetic polarity timescale for the Late Cretaceous and Cenozoic. *J. Geophys. Res.,* 100:6093–6095.

Chaisson, W.P., and Leckie, R.M., 1993. High-resolution Neogene planktonic foraminifer biostratigraphy of Site 806, Ontong Java Plateau (western equatorial Pacific). *In* Berger, W.H., Kroenke, L.W., Mayer, L.A., et al., *Proc. ODP, Sci. Results,* 130: College Station, TX (Ocean Drilling Program), 137–178.

Chaisson, W.P., and Pearson, P.N., 1997. Planktonic foraminifer biostratigraphy at Site 925: middle Miocene–Pleistocene. *In* Shackleton, N.J., Curry, W.B., Richter, C., and Bralower, T.J. (Eds.), *Proc. ODP, Sci. Results,* 154: College Station, TX (Ocean Drilling Program), 3–31.

Curry, W.B., Shackleton, N.J., Richter, C., et al., 1995. *Proc. ODP, Init. Repts.,* 154: College Station, TX (Ocean Drilling Program).

Droser, M.L., and Bottjer, D.J., 1986. A semiquantitative field classification of ichnofabric. *J. Sediment. Petrol.,* 56:558–559.

Dymond, J., Corliss, J.B., and Stillinger, R., 1976. Chemical composition and metal accumulation rates of metalliferous sediments from Sites 319, 320, and 321. *In* Yeats, R.S., Hart, S.R., et al., *Init. Repts. DSDP,* 34: Washington (U.S. Govt. Printing Office), 575–588.

Ellis, D.V., 1987. *Well Logging for Earth Scientists:* New York (Elsevier).

Evans, H.B., 1965. GRAPE—a device for continuous determination of material density and porosity. *Trans. SPWLA 6th Ann. Logging Symp.,* Dallas, 2:B1–B25.

Exon, N.F., Kennett, J.K., Malone, M., et al., 2001. *Proc. ODP, Init. Repts.,* 189: College Station, TX (Ocean Drilling Program).

Gieskes, J., Gamo, T., and Brumsack, H.-J., 1991. Chemical methods for interstitial water analysis aboard *JOIDES Resolution. ODP Tech. Note,* 15.

Goldberg, D., 1990. Test performance of the Ocean Drilling Program wireline heave motion compensator. *Sci. Drill.,* 1:206–209.

————, 1997. The role of downhole measurements in marine geology and geophysics. *Rev. Geophys.,* 35:315–342.

Hagelberg, T., Shackleton, N., Pisias, N., and Shipboard Scientific Party, 1992. Development of composite depth sections for Sites 844 through 854. *In* Mayer, L., Pisias, N., Janecek, T., et al., *Proc. ODP, Init. Repts.,* 138 (Pt. 1): College Station, TX (Ocean Drilling Program), 79–85.

Hagelberg, T.K., Pisias, N.G., Shackleton, N.J., Mix, A.C., and Harris, S., 1995. Refinement of a high-resolution, continuous sedimentary section for studying equatorial Pacific Ocean paleoceanography, Leg 138. *In* Pisias, N.G., Mayer, L.A., Janecek, T.R., Palmer-Julson, A., and van Andel, T.H. (Eds.), *Proc. ODP, Sci Results,* 138: College Station, TX (Ocean Drilling Program), 31–46.

Harris, S., Hagelberg, T., Mix, A., Pisias, N.G., and Shackleton, N.J., 1995. Sediment depths determined by comparisons of GRAPE and logging density data during Leg 138. *In* Pisias, N.G., Mayer, L.A., Janecek, T.R., Palmer-Julson, A., and van Andel, T.H. (Eds.), *Proc. ODP, Sci. Results,* 138: College Station, TX (Ocean Drilling Program), 47–57.

Hilgen, F.J., 1991a. Astronomical calibration of Gauss to Matuyama sapropels in the Mediterranean and implication for the geomagnetic polarity time scale. *Earth Planet. Sci. Lett.,* 104:226–244.

————, 1991b. Extension of the astronomically calibrated (polarity) time scale to the Miocene/Pliocene boundary. *Earth Planet. Sci. Lett.,* 107:349–368.

Hollis, C.J., 1993. Latest Cretaceous to late Paleocene radiolarian biostratigraphy: a new zonation from the New Zealand region. *Mar. Micropaleontol.,* 21:295–327.

Hoppie, B.W., Blum, P., and the Shipboard Scientific Party, 1994. Natural gamma-ray measurements on ODP cores: introduction to procedures with examples from Leg 150. *In* Mountain, G.S., Miller, K.G., Blum, P., et al., *Proc. ODP, Init. Repts.,* 150: College Station, TX (Ocean Drilling Program), 51–59.

Horai, K., and Von Herzen, R.P., 1985. Measurement of heat flow on Leg 86 of the Deep Sea Drilling Project. *In* Heath, G.R., Burckle, L.H., et al., *Init. Repts. DSDP,* 86: Washington (U.S. Govt. Printing Office), 759–777.

Hyndman, R.D., Erickson, A.J., and Von Herzen, R.P., 1974. Geothermal measurements on DSDP Leg 26. *In* Davies, T.A., Luyendyk, B.P., et al., *Proc. DSDP, Init. Repts.,* 26: Washington (U.S. Govt. Printing Office), 451–463.

Jansen, E., Raymo, M.E., Blum, P., et al., 1996. *Proc. ODP, Init. Repts.,* 162: College Station, TX (Ocean Drilling Program).

Johnson, D.A., and Nigrini, C.A., 1985. Synchronous and time-transgressive Neogene radiolarian datum levels in the equatorial Indian and Pacific Oceans. *Mar. Micropaleontol.,* 9:489–523.

Johnson, D.A., Schneider, D.A., Nigrini, C.A., Caulet, J.-P., and Kent, D.V., 1989. Pliocene-Pleistocene radiolarian events and magnetostratigraphic calibrations for the tropical Indian Ocean. *Mar. Micropaleontol.,* 14:33–66.

Keene, J.B., 1975. Cherts and porcellanites from the North Pacific DSDP, Leg 32. *In* Larson, R.L., Moberly, R., et al. *Init. Repts. DSDP,* 32: Washington (U.S. Govt. Printing Office), 429–507.

Kelly, D.C., Bralower, T.J., and Zachos, J.C., 1998. Evolutionary consequences of the latest Paleocene thermal maximum for tropical planktonic foraminifera. *Palaeogeogr., Palaeoclimatol., Palaeoecol.,* 141:139–161.

Kelly, D.C., Bralower, T.J., Zachos, J.C., Premoli Silva, I., and Thomas, E., 1996. Rapid diversification of planktonic foraminifera in the tropical Pacific (ODP Site 865) during the late Paleocene thermal maximum. *Geology,* 24:423–426.

Kennett, J.P., and Srinivasan, M.S., 1983. *Neogene Planktonic Foraminifera: A Phylogenetic Atlas:* Stroudsburg, PA (Hutchinson Ross).

Kristiansen, J.I., 1982. The transient cylindrical probe method for determination of thermal parameters of earth materials [Ph.D. dissert.]. Aaehus Univ.

Lazarus, D., Spencer-Cervato, C., Pianka-Biolzi, M., Beckmann, J.P., von Salis, K., Hilbrecht, H., and Thierstein, H., 1995. Revised Chronology of Neogene DSDP Holes from the World. *ODP Tech. Note,* 24.

Leckie, R.M., Farnham, C., and Schmidt, M.G., 1993. Oligocene planktonic foraminifer biostratigraphy of Hole 803D (Ontong Java Plateau) and Hole 628A (Little Bahama Bank), and comparison with the southern high latitudes. *In* Berger, W.H., Kroenke, L.V., and Mayer, L.A., *Proc. ODP, Sci. Results,* 130: College Station, TX (Ocean Drilling Program), 113–136.

Loeblich, A.R., Jr., and Tappan, H., 1988. *Foraminiferal genera and their classification:* New York (Van Nostrand Reinhold).

Lourens, L.J., Antonarakou, A., Hilgen, F.J., Van Hoof, A.A.M., Vergnaud-Grazzini, C., and Zachariasse, W.J., 1996. Evaluation of the Plio-Pleistocene astronomical timescale. *Paleoceanography,* 11:391–413.

Lovell, M.A., Harvey, P.K., Brewer, T.S., Williams, C., Jackson, P.D., and Williamson, G., 1998. Application of FMS images in the Ocean Drilling Program: an overview. *In* Cramp, A., MacLeod, C.J., Lee, S.V., and Jones, E.J.W. (Eds.), *Geological Evolution of Ocean Basins: Results from the Ocean Drilling Program.* Spec. Publ.—Geol. Soc. London, 131:287–303.

Luthi, S.M., 1990. Sedimentary structures of clastic rocks identified from electrical borehole images. *In* Hurst, A., Lovell, M.A., and Morton, A.C. (Eds.), *Geological Applications of Wireline Logs*. Spec. Publ.—Geol. Soc. London, 48:3–10.

Lyle, M., Koizumi, I., Richter, C., et al., 1997. *Proc. ODP, Init. Repts.,* 167: College Station, TX (Ocean Drilling Program).

Mackenzie, K.V., 1981. Nine-term equation for sound speed in the oceans. *J. Acoust. Soc. Am.,* 70:807–812.

Manheim, F.T., and Sayles, F.L., 1974. Composition and origin of interstitial waters of marine sediments, based on deep sea drill cores. *In* Goldberg, E.D. (Ed.), *The Sea* (Vol. 5): *Marine Chemistry: The Sedimentary Cycle:* New York (Wiley), 527–568.

Martini, E., 1971. Standard Tertiary and Quaternary calcareous nannoplankton zonation. *In* Farinacci, A. (Ed.), *Proc. 2nd Int. Conf. Planktonic Microfossils Roma:* Rome (Ed. Tecnosci.), 2:739–785.

Mayer, L., Pisias, N., Janecek, T., et al., 1992. *Proc. ODP, Init. Repts.,* 138 (Pts. 1 and 2): College Station, TX (Ocean Drilling Program).

Mazzullo, J.M., Meyer, A., and Kidd, R.B., 1988. New sediment classification scheme for the Ocean Drilling Program. *In* Mazzullo, J., and Graham, A.G. (Eds.), *Handbook for Shipboard Sedimentologists. ODP Tech. Note,* 8:45–67.

Monechi, S., and Thierstein, H.R., 1985. Late Cretaceous–Eocene nannofossil and magnetostratigraphic correlations near Gubbio, Italy. *Mar. Micropaleontol.,* 9:419–440.

Moran, K., 1997. Elastic property corrections applied to Leg 154 sediment, Ceara Rise. *In* Shackleton, N.J., Curry, W.B., Richter, C., and Bralower, T.J. (Eds.), *Proc. ODP, Sci. Results,* 154: College Station, TX (Ocean Drilling Program), 151–155.

Munsell Color Company, Inc., 1994. *Munsell Soil Color Chart:* (revised ed.): Newburgh, MD (Munsell Color).

Murray, R.W., Miller, D.J., and Kryc, K.A., 2000. Analysis of major and trace elements in rocks, sediments, and interstitial waters by inductively coupled plasma–atomic emission spectrometry (ICP-AES). *ODP Tech. Note, 29* [Online]. Available from World Wide Web: <http://www-odp.tamu.edu/publications/tnotes/tn29/INDEX.HTM>. [Cited 2001-10-15]

Nigrini, C., and Sanfilippo, A., 2001. Cenozoic radiolarian stratigraphy for low and middle latitudes with descriptions of biomarkers and stratigraphically useful species. *ODP Tech. Note,* 27 [Online]. Available from World Wide Web: <http://www-odp.tamu.edu/publications/tnotes/tn27/index.html>. [Cited 2001-10-15]

Nishimura, A., 1992. Paleocene radiolarian biostratigraphy in the northwest Atlantic at Site 384, Leg 43, of the Deep Sea Drilling Project. *Micropaleontology,* 38:317–362.

Norris, R.D., 1998. Planktonic foraminifer biostratigraphy: eastern equatorial Atlantic. *In* Mascle, J., Lohmann, G.P., and Moullade, M. (Eds.), *Proc. ODP, Sci. Results,* 159: College Station, TX (Ocean Drilling Program), 445–479.

Norris, R.D., Kroon, D., Klaus, A., et al., 1998. *Proc. ODP, Init. Reports,* 171B: College Station, TX (Ocean Drilling Program).

Norris, R.D., and Röhl, U., 1999. Carbon cycling and chronology of climate warming during the Palaeocene/Eocene transition. *Nature,* 401:775–778.

Okada, H., and Bukry, D., 1980. Supplementary modification and introduction of code numbers to the low-latitude coccolith biostratigraphic zonation (Bukry, 1973; 1975). *Mar. Micropaleontol.,* 5:321–325.

Olafsson, G., and Villa, G., 1992. Reliability of sphenoliths as zonal markers in Oligocene sediments from the Atlantic and Indian oceans. *In* Proto Decima, F., Monechi, S., and Rio, D. (Eds.), *Proc. Int. Nannoplankton Assoc. Conf., Firenze 1989*. Mem. Sci. Geol., 43:261–275.

Olsson, R.K., Hemleben, C., Berggren, W.A., and Huber, B.T. (Eds.), 1999. *Atlas of Paleocene Planktonic Forminifera.* Smithsonian Contrib. Paleobiol., 85.

Pearson, P.N., 1995. Planktonic foraminifer biostratigraphy and the development of pelagic caps on guyots in the Marshall Islands Group. *In* Haggerty, J., Premoli Silva,

I., Rack, F., and McNutt, M.K. (Eds.), *Proc. ODP, Sci. Results,* 144: College Station, TX (Ocean Drilling Program), 21–59.

Pearson, P.N., and Chaisson, W.P., 1997. Late Paleocene to middle Miocene planktonic foraminifer biostratigraphy of the Ceara Rise. *In* Shackleton, N.J., Curry, W.B., Richter, C., and Bralower, T.J. (Eds.), *Proc. ODP, Sci. Results,* 154: College Station, TX (Ocean Drilling Program), 33–68.

Perch-Nielsen, K., 1985. Cenozoic calcareous nannofossils. *In* Bolli, H.M., Saunders, J.B., and Perch-Nielsen, K. (Eds.), *Plankton Stratigraphy:* Cambridge (Cambridge Univ. Press), 427–554.

Pflum, C.E., and Frerichs, W.E., 1976. Gulf of Mexico deep-water foraminifers. *Spec. Publ.—Cushman Found. Foraminiferal Res.,* 14:1-122.

Poag, C.W., Mankinen, E., and Norris, R.D., in press. Late Eocene impacts: geological record, correlation, and paleoenvironmental consequences. *In* Prothero, D.R., Ivany, L.C., and Nesbitt, E. (Eds.), *From Greenhouse to Icehouse: The Marine Eocene–Oligocene Transition:* New York (Columbia Univ. Press).

Postuma, J.A., 1971. *Manual of Planktonic Foraminifera:* Amsterdam (Elsevier).

Pribnow, D.F.C., Kinoshita, M., and Stein, C.A., 2000. Thermal data collection and heat flow recalculations for ODP Legs 101–180. Institute for Joint Geoscientific Research, GGA, Hanover, Germany, 0120432. Available from World Wide Web: <http://www-odp.tamu.edu/publications/heatflow/>. Cited [2001-10-26]

Raffi, I., Backman, J., Rio, D., and Shackleton, N.J., 1993. Plio-Pleistocene nannofossil biostratigraphy and calibration to oxygen isotope stratigraphies from Deep Sea Drilling Project Site 607 and Ocean Drilling Program Site 677. *Paleoceanography,* 8:387-408.

Raffi, I., and Flores, J.-A., 1995. Pleistocene through Miocene calcareous nannofossils from eastern equatorial Pacific Ocean (Leg 138). *In* Pisias, N.G., Mayer, L.A., Janecek, T.R., Palmer-Julson, A., and van Andel, T.H. (Eds.). *Proc. ODP, Sci. Results,* 138: College Station, TX (Ocean Drilling Program), 233–286.

Rider, M., 1996. *The Geological Interpretation of Well Logs* (2nd ed.): Caithness (Whittles Publishing).

Rock-Color Chart Committee, 1991. *Rock Color Charts.* Geol. Soc. Am.

Röhl, U., Bralower, T.J., Norris, R.D., and Wefer, G., 2000. New chronology for the late Paleocene thermal maximum and its environmental implications. *Geology,* 28:927–930.

Ruddiman, W.F., Cameron, D., and Clement, B.M., 1987. Sediment disturbance and correlation of offset holes drilled with the hydraulic piston corer: Leg 94. *In* Ruddiman, W.F., Kidd, R.B., Thomas, E., et al., *Init. Repts. DSDP,* 94 (Pt. 2): Washington (U.S. Govt. Printing Office), 615–634.

Salimullah, A.R.M., and Stow, D.A.V., 1992. Application of FMS images in poorly recovered coring intervals: examples from ODP Leg 129. *In* Hurst, A., Griffiths, C.M., and Worthington, P.F. (Eds.), *Geological Application of Wireline Logs II.* Spec. Publ.—Geol. Soc. London, 65:71–86.

Sanfillipo, A., and Blome, C.D., 2001. Biostratigraphic implications of mid-latitude Palaeocene–Eocene radiolarian faunas from Hole 1051A, ODP Leg 171B, Blake Nose, western North Atlantic. *In* Kroon, D., Norris, R.D., and Klaus, A. (Eds.), *Western North Atlantic Paleogene and Cretaceous Paleoceanography,* Spec. Publ.—Geol. Soc. London, 183:185–224.

Sanfilippo, A., and Nigrini, C., 1995. Radiolarian stratigraphy across the Oligocene/Miocene transition. *Mar. Micropaleontology,* 24:239–285.

————, 1996. Radiolarian biomarkers at the Oligocene/Miocene boundary. *In* Moguilevsky, A., and Watley, R. (Eds.), *Microfossils and Oceanic Environments. Proceedings of ODP and the Marine Biosphere:* Aberystwyth, Wales (Univ. Wales, Aberystwyth Press), 317–326.

————, 1998. Code numbers for Cenozoic low latitude radiolarian biostratigraphic zones and GPTS conversion tables. *Mar. Micropaleontol.,* 33:109–156.

Schlumberger, 1989. *Log Interpretation Principles/Applications:* Houston (Schlumberger Educ. Services), SMP–7017.

Schlumberger, 1994. *IPL Integrated Porosity Lithology:* Houston (Schlumberger Wireline and Testing), SMP-9270.

Serra, O., 1984. *Fundamentals of Well-Log Interpretation* (Vol. 1): *The Acquisition of Logging Data:* Dev. Pet. Sci., 15A.

————, 1986. *Fundamentals of Well-Log Interpretation* (Vol. 2): *The Interpretation of Logging Data*. Dev. Pet. Sci., 15B.

————, 1989. *Formation MicroScanner Image Interpretation:* Houston (Schlumberger Educ. Services), SMP-7028.

Shackleton, N.J., Baldauf, J.G., Flores, J.-A., Iwai, M., Moore, T.C., Jr., Raffi, I., and Vincent, E., 1995a. Biostratigraphic summary for Leg 138. *In* Pisias, N.G., Mayer, L.A., Janecek, T.R., Palmer-Julson, A., and van Andel, T.H. (Eds.), *Proc. ODP, Sci. Results,* 138: College Station, TX (Ocean Drilling Program), 517–536.

Shackleton, N.J., Berger, A., and Peltier, W.A., 1990. An alternative astronomical calibration of the lower Pleistocene timescale based on ODP Site 677. *Trans. R. Soc. Edinburgh: Earth Sci.,* 81:251–261.

Shackleton, N.J., Crowhurst, S., Hagelberg, T., Pisias, N.G., and Schneider, D.A., 1995b. A new late Neogene time scale: application to Leg 138 sites. *In* Pisias, N.G., Mayer, L.A., Janecek, T.R., Palmer-Julson, A., and van Andel, T.H. (Eds.), *Proc. ODP, Sci. Results,* 138: College Station, TX (Ocean Drilling Program), 73–101.

Shackleton, N.J., Crowhurst, S.J., Weedon, G.P., and Laskar, J., 1999. Astronomical calibration of Oligocene–Miocene time. *Philos. Trans. R. Soc. London, Ser. A,* 357:1,907–1,929.

Speijer, R.P., Schmitz, B., and van der Zwaan, G.J., 1997. Benthic foraminiferal extinction and repopulation in response to latest Paleocene Tethyan anoxia. *Geology,* 25:683–686.

Spezzaferri, S., 1994. Planktonic foraminiferal biostratigraphy and taxonomy of the Oligocene and lower Miocene in the oceanic record: an overview. *Palaeontographica Ital.,* 81:1–187.

Spezzaferri, S., and Premoli Silva, I., 1991. Oligocene planktonic foraminiferal biostratigraphy and paleoclimatic interpretation from Hole 538A, DSDP Leg 77, Gulf of Mexico. *Palaeogeogr., Palaeoclimatol., Palaeoecol.,* 83:217–263.

Tauxe, L., Tucker, P., Petersen, N.P., and LaBrecque, J.L., 1984. Magnetostratigraphy of Leg 73 sediments. *In* Hsü, K.J., LaBrecque, J.L., et al., *Init. Repts. DSDP,* 73: Washington (U.S. Govt. Printing Office), 609–621.

Thierstein, H.R., Geitzenauer, K., Molfino, B., and Shackleton, N.J., 1977. Global synchroneity of late Quaternary coccolith datum levels: validation by oxygen isotopes. *Geology,* 5:400–404.

Tiedemann, R., Sarnthein, M., and Shackleton, N.J., 1994. Astronomic timescale for the Pliocene Atlantic $\delta^{18}O$ and dust flux records of Ocean Drilling Program Site 659. *Paleoceanography,* 9:619–638.

Tjalsma, R.C., and Lohmann, G.P., 1983. *Paleocene–Eocene Bathyal and Abyssal Benthic Foraminifera from the Atlantic Ocean*. Spec. Publ.—Micropaleontol., 4:1–90.

Toumarkine, M., and Luterbacher, H., 1985. Paleocene and Eocene planktic foraminifera. *In* Bolli, H.M., Saunders, J.B., and Perch-Nielsen, K. (Eds.), *Plankton Stratigraphy:* Cambridge (Cambridge Univ. Press), 87–154.

van Morkhoven, F.P.C.M., Berggren, W.A., and Edwards, A.S., 1986. Cenozoic cosmopolitan deep-water benthic foraminifera. *Bull. Cent. Rech. Explor.—Prod. Elf-Aquitaine,* 11.

Van Couvering, J.A., Castradori, D., Cita, M.B., Hilgen, F.J., and Rio, D., 2000. The base of the Zanclean stage and the Pliocene series. *Episodes,* 23:179–187.

Von Herzen, R.P., and Maxwell, A.E., 1959. The measurement of thermal conductivity of deep-sea sediments by a needle-probe method. *J. Geophys. Res.,* 64:1557–1563.

Wentworth, C.K., 1922. A scale of grade and class terms of clastic sediments. *J. Geol.,* 30:377–392.

Wilson, W.D., 1960. Speed of sound in seawater as a function of temperature, pressure and salinity. *J. Acoust. Soc. Am.,* 32:641–644.
Wyllie, M.R.J., Gregory, A.R., and Gardner, L.W., 1956. Elastic wave velocities in heterogeneous and porous media. *Geophysics,* 21:41–70.

Figure F1. Example of coring and depth intervals.

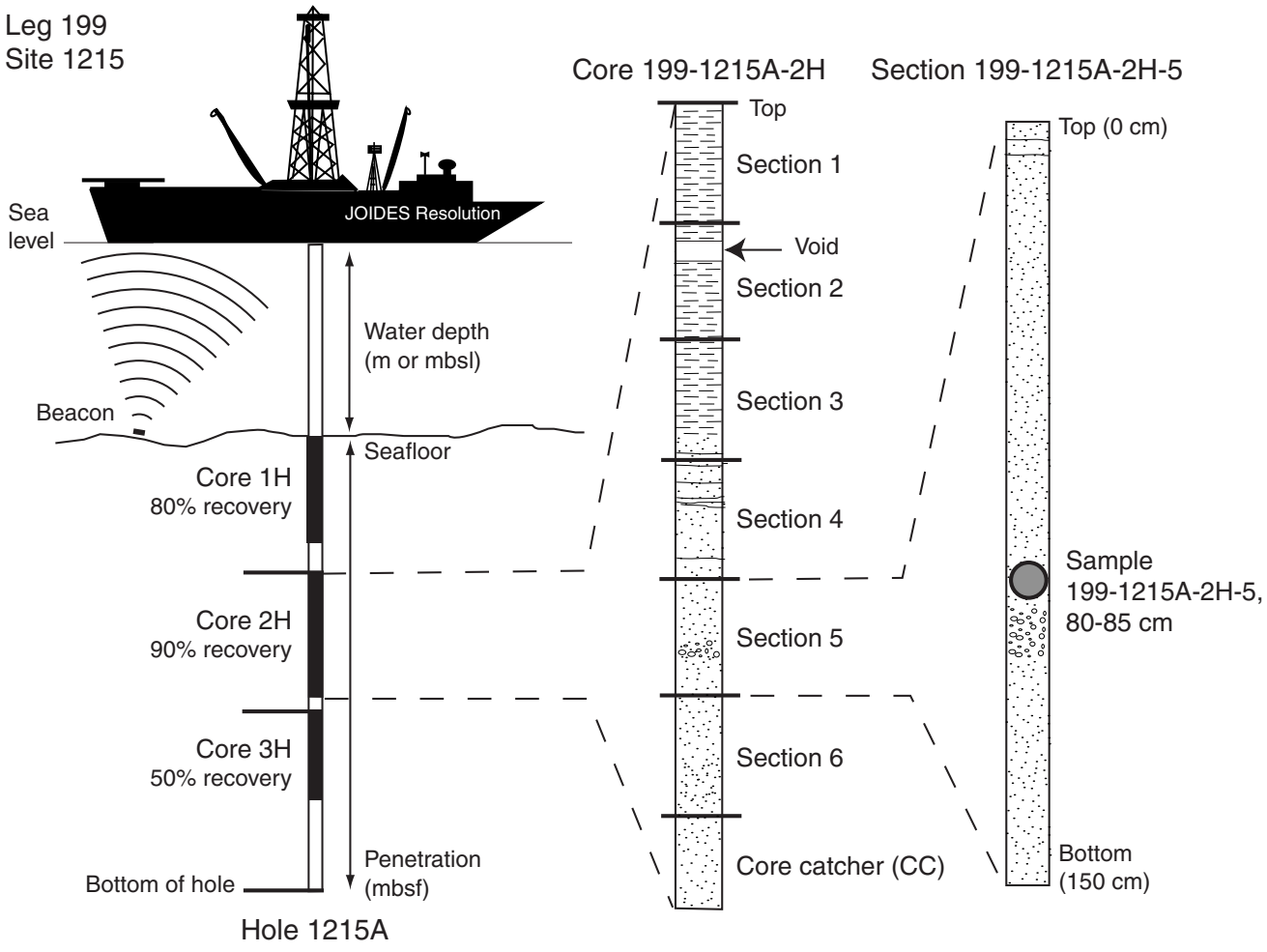

Figure F2. Example of an AppleCORE summary barrel sheet showing MST data (GRA, MS, and color reflectance) alongside a simplified graphical summary of the visual core description. MST = multisensor track, GRA = gamma ray attenuation, SS = smear slide, IW = interstitial water samples, PAL = micropaleontology samples, ye BR = yellowish brown, dk ye BR = dark yellowish brown, dk gy BR = dark grayish brown, vdk gy BR = very dark grayish brown.

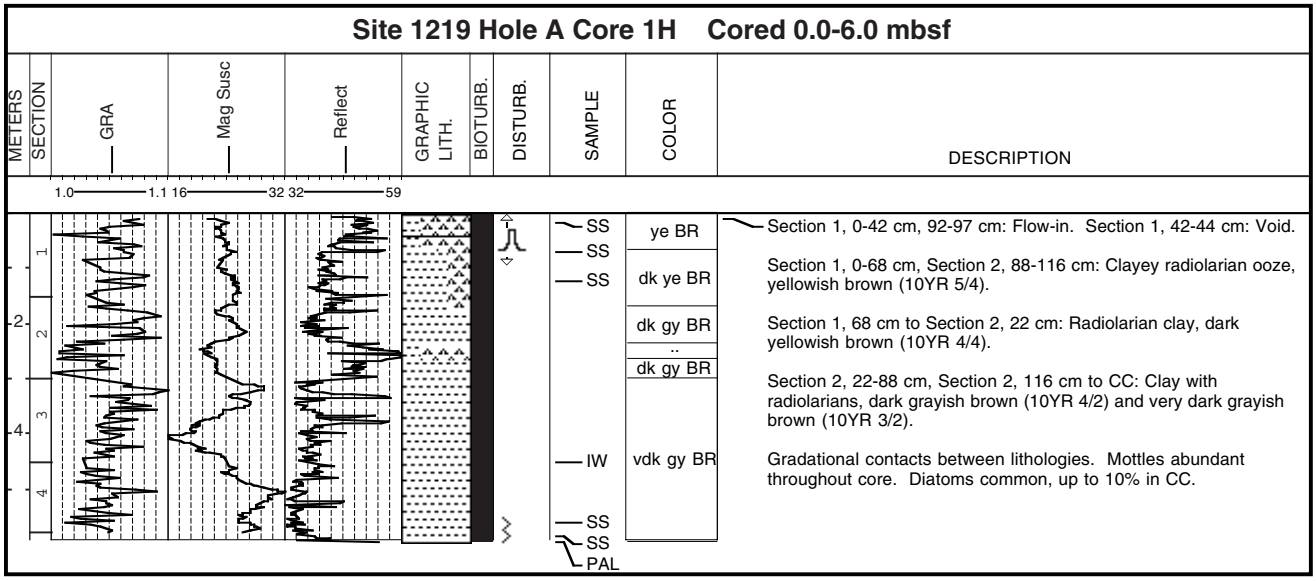

Figure F3. Key to symbols used for graphic lithologies on the AppleCORE summary barrel sheets.

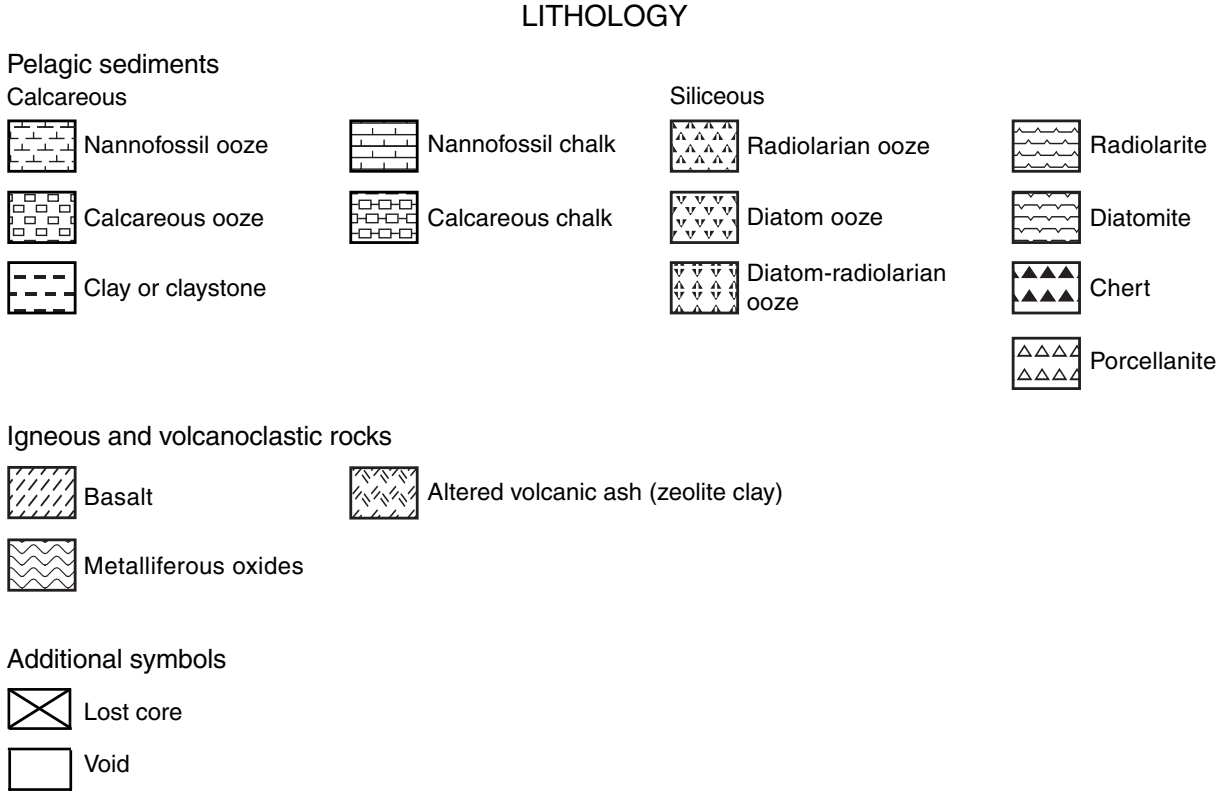

Figure F4. Key to symbols used for contacts, physical structures, lithologic accessories, ichnofossils, fossils, core disturbance, and bioturbation on the AppleCORE summary barrel sheets.

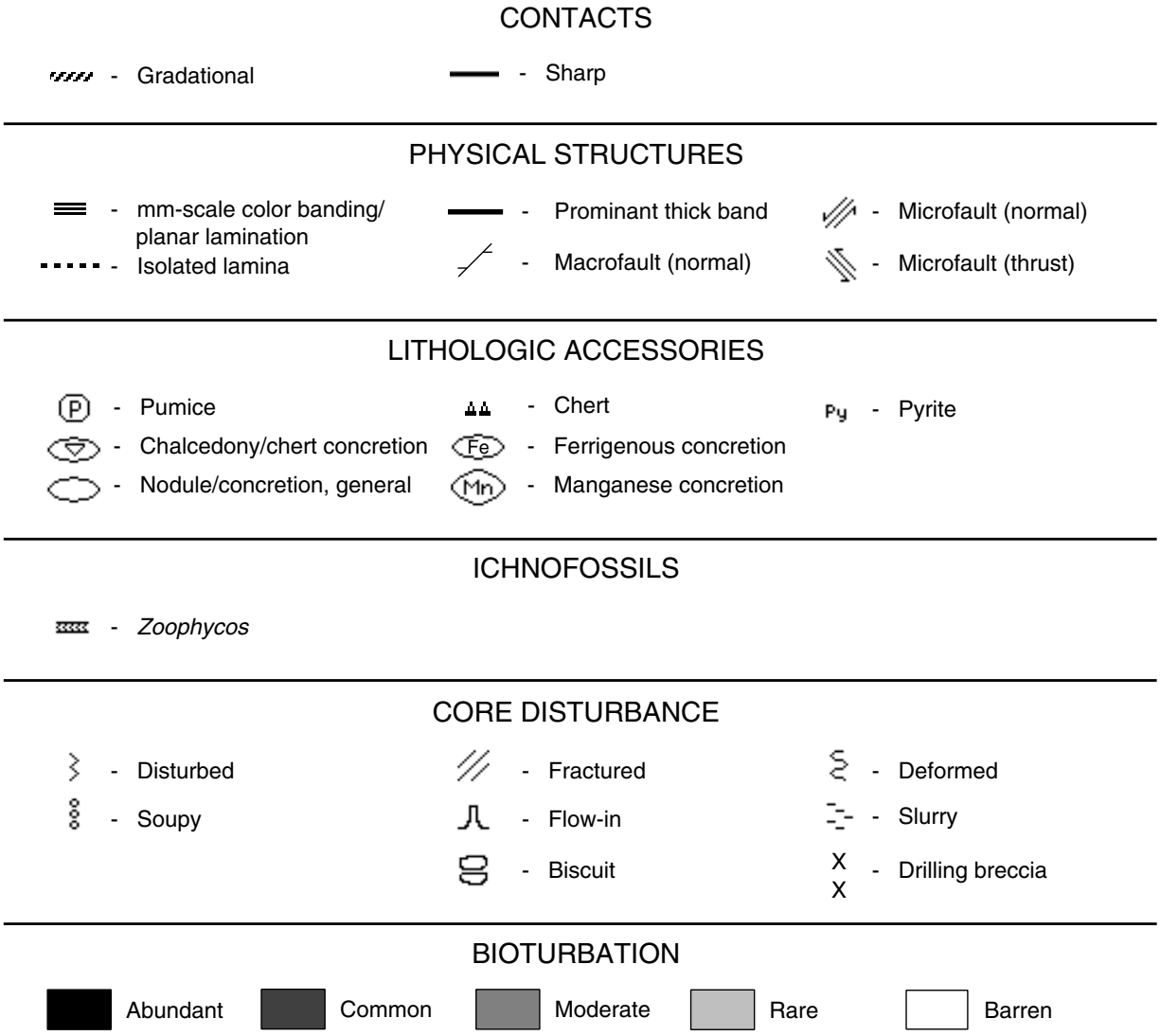

Figure F5. Ternary diagram showing nomenclature for principal components of whole-rock composition.

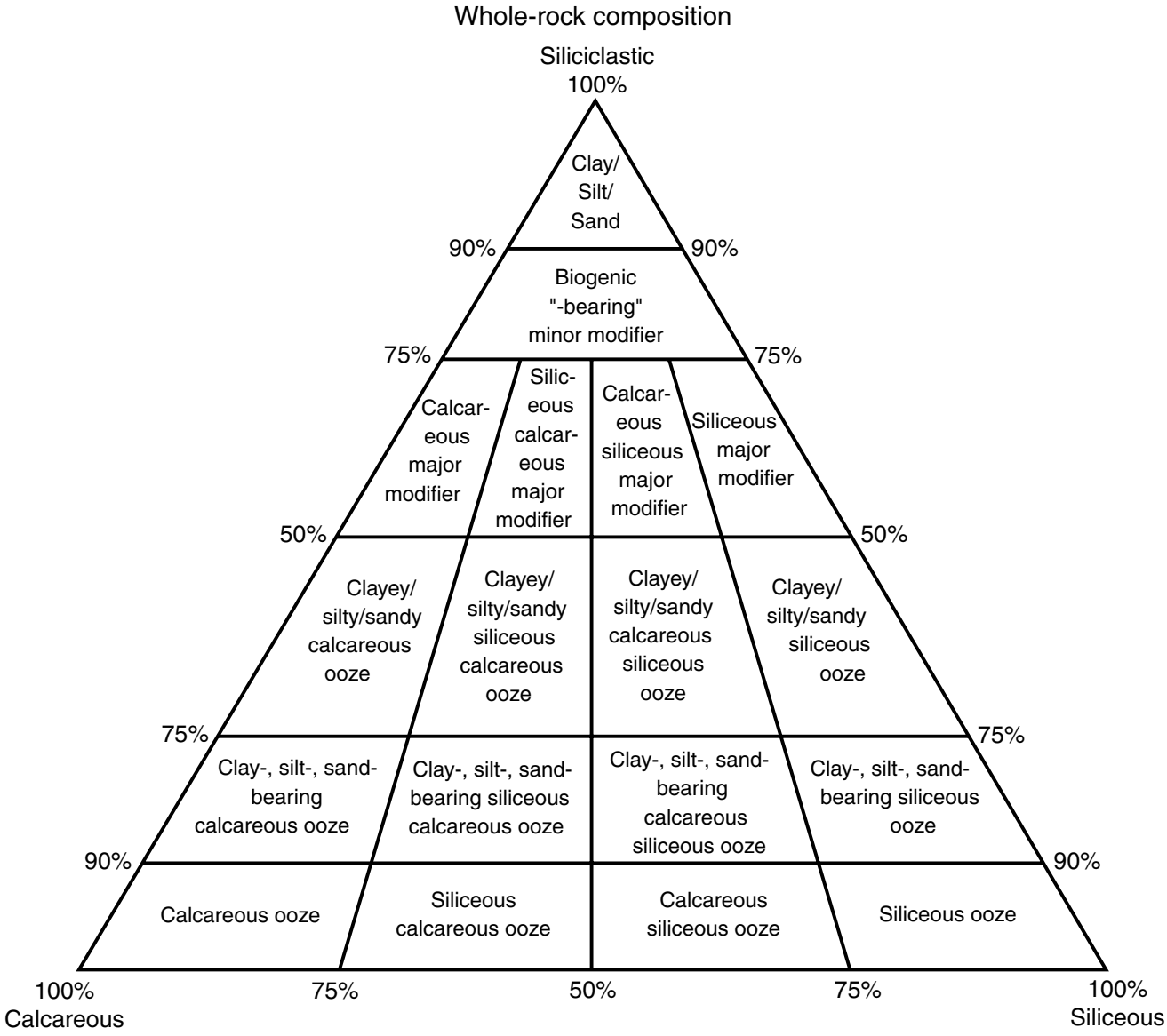

Figure F6. Grain-size divisions for sedimentary rocks (adapted from Wentworth, 1922).

Grain size (mm)	Grain size (μm)	Phi (ϕ)	Wentworth size class		Rock type
4096		-12.0	Boulder		Conglomerate/ Breccia
256		-8.0	Cobble	Gravel	
64		-6.0	Pebble		
4		-2.0	Granule		
2.00		-1.0	Very coarse sand		Sandstone
1.00		0.0	Coarse sand		
1/2 0.50	500	1.0	Medium sand	Sand	
1/4 0.25	250	2.0	Fine sand		
1/8 0.125	125	3.0	Very fine sand		
1/16 0.0625	63	4.0	Coarse silt		Siltstone
1/32 0.031	31	5.0	Medium silt		
1/64 0.0156	15.6	6.0	Fine silt	Silt	
1/128 0.0078	7.8	7.0	Very fine silt		
1/256 0.0039	3.9	8.0	Clay	Mud	Claystone
0.00006	0.06	14.0			

Figure F7. Correlation chart for the interval from 0 to 65 Ma. Underlined terms are foraminifers. T = top, B = bottom. Forams = foraminifers, Rads = radiolarians, Nanno = nannofossils. (Continued on next three pages.)

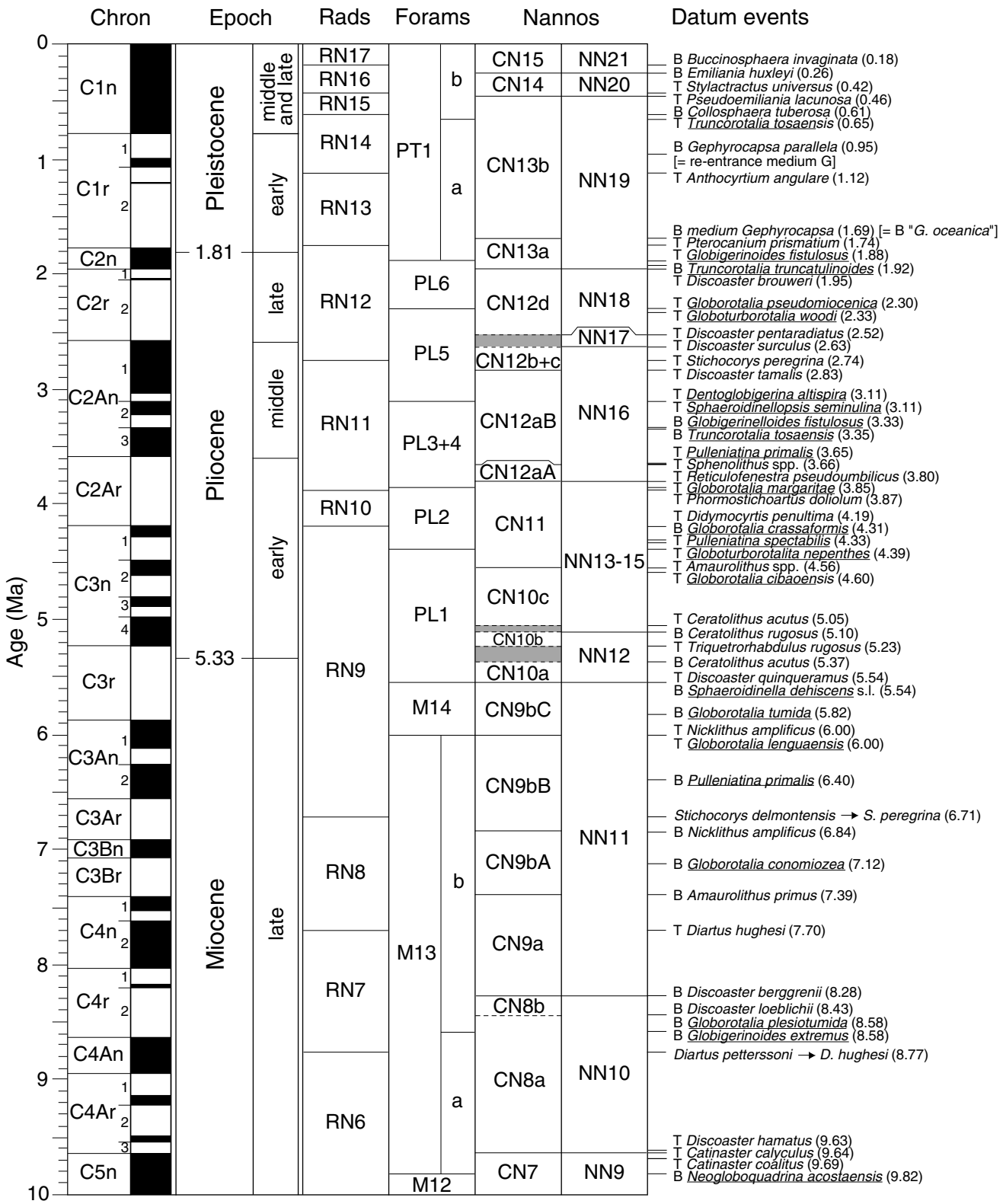

Figure F7 (continued.)

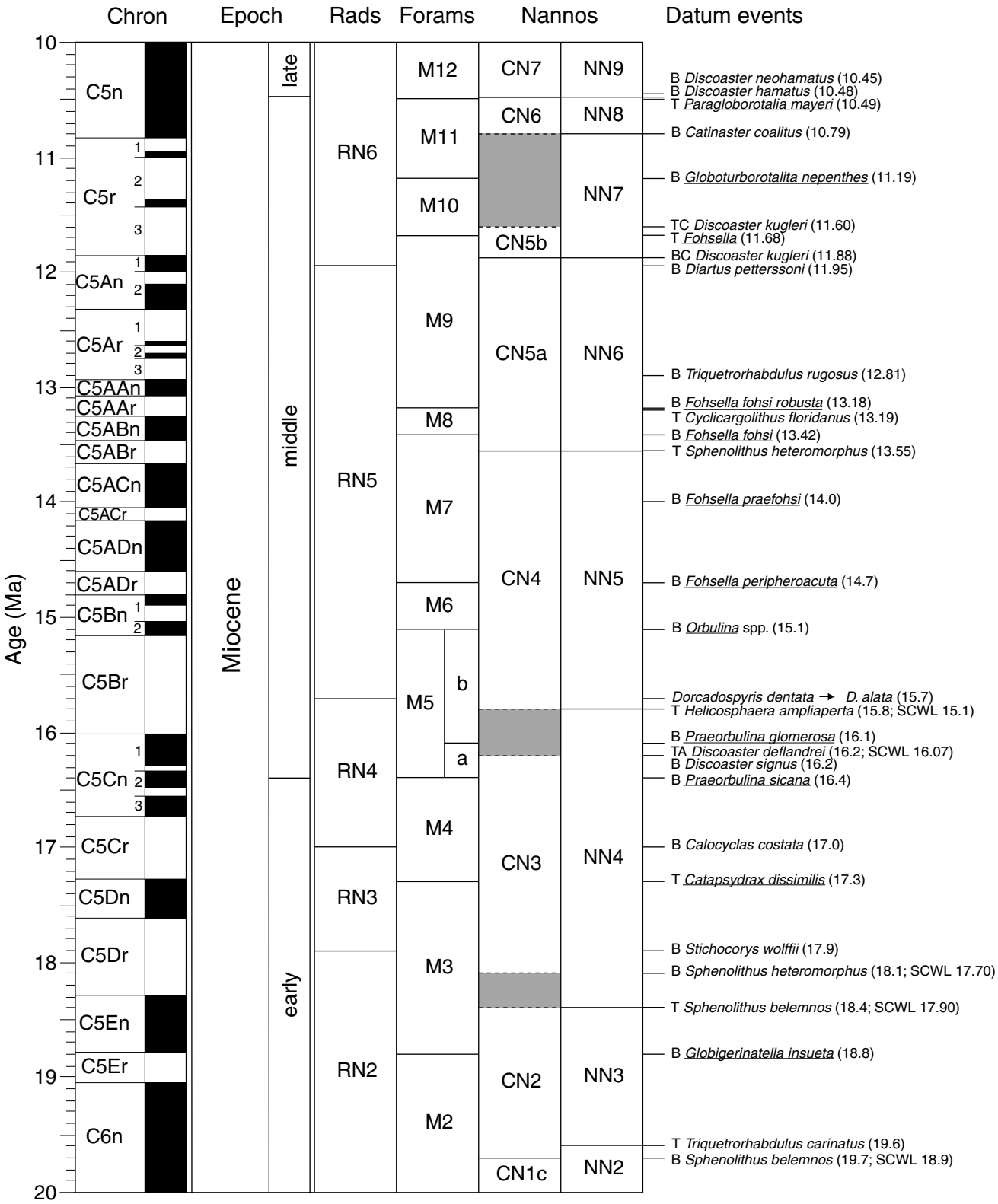

Figure F7 (continued.)

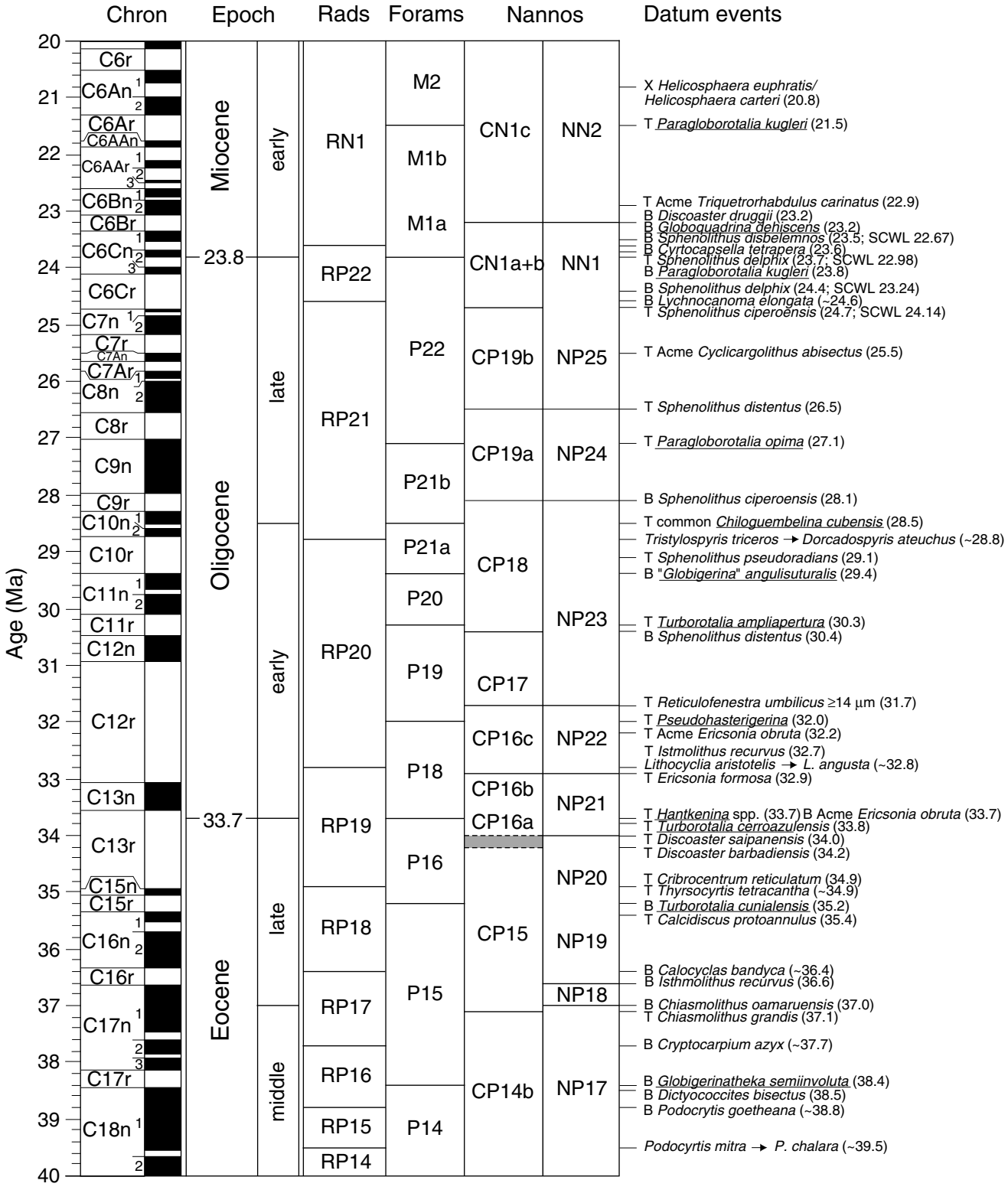

Figure F7 (continued.)

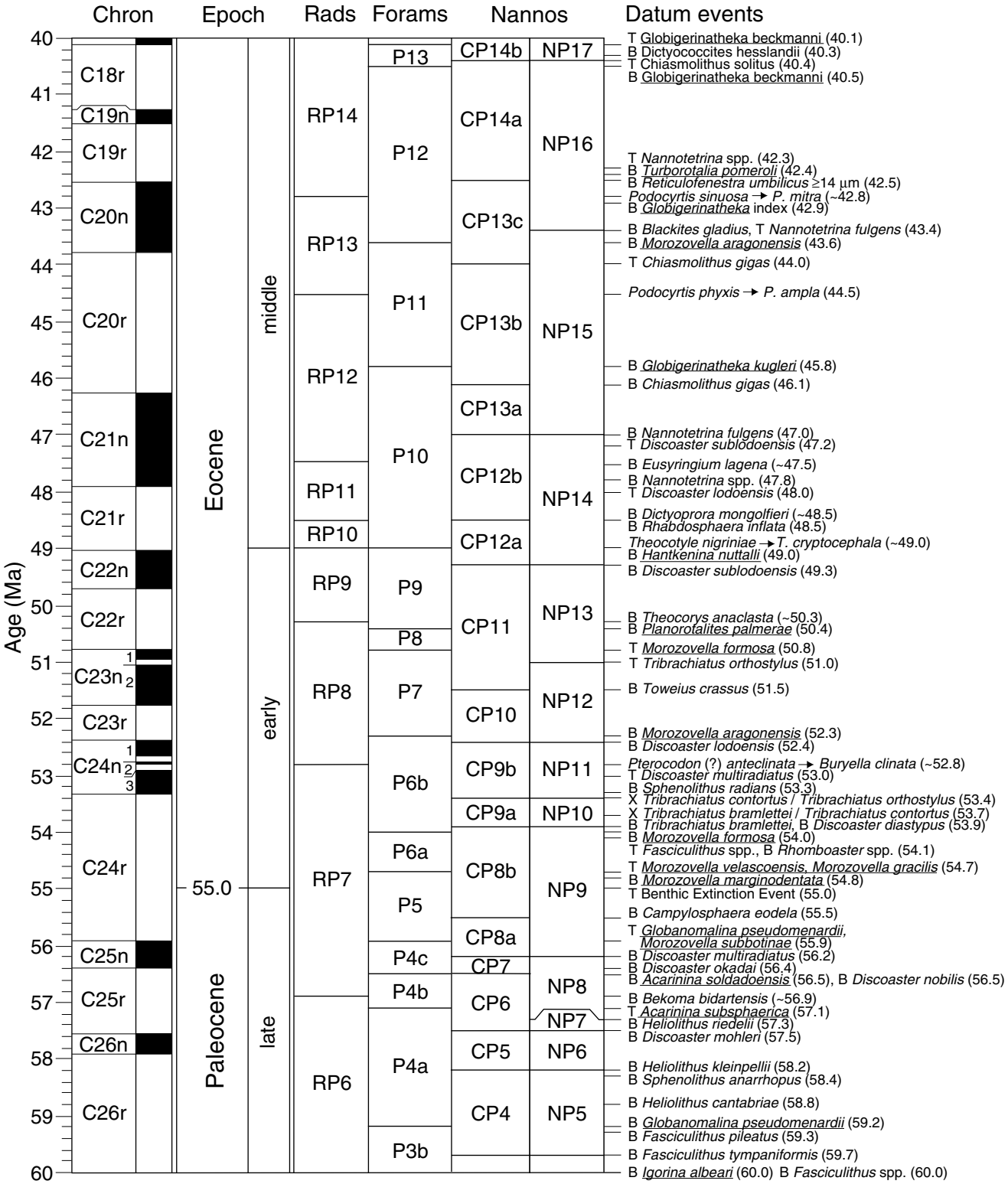

Figure F8. A. Selected interval of MS data from Holes 1218A (left; black), 1218B (middle; blue), and 1218C (right; green) shown on the mbsf depth scale. Data from Holes 1218B and 1218C are offset by a constant for clarity. **B.** The same records are shown after depth-scale adjustment so that correlative features are aligned. **C.** The resulting spliced record is shown utilizing cores for Holes 1218A and 1218B.

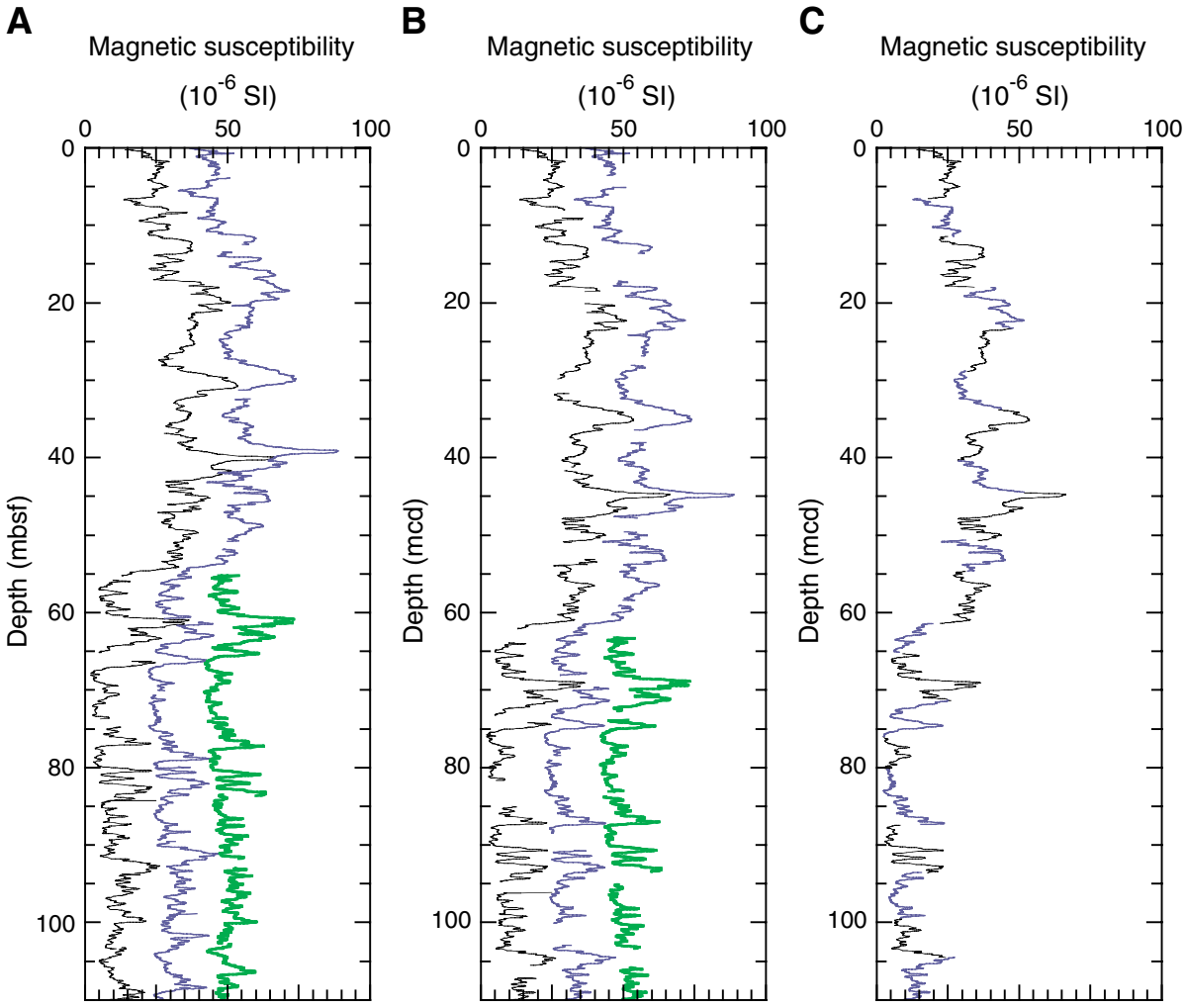

Figure F9. $CaCO_3$ calculated from Ca determined by ICP-AES vs. $CaCO_3$ determined by coulometer. Scatter seen for measured vs. calculated $CaCO_3$ > ~75 wt% is attributable to a combination of two factors: (1) precision for Ca determined by ICP-AES is relatively low (±11.5%) and (2) some samples analyzed (e.g., Oligocene carbonate ooze and chalk) contain more $CaCO_3$ than the ICP-AES standard with highest $CaCO_3$ content (NIST-IC, an argillaceous limestone containing 90 wt% $CaCO_3$; 35.9 wt% Ca).

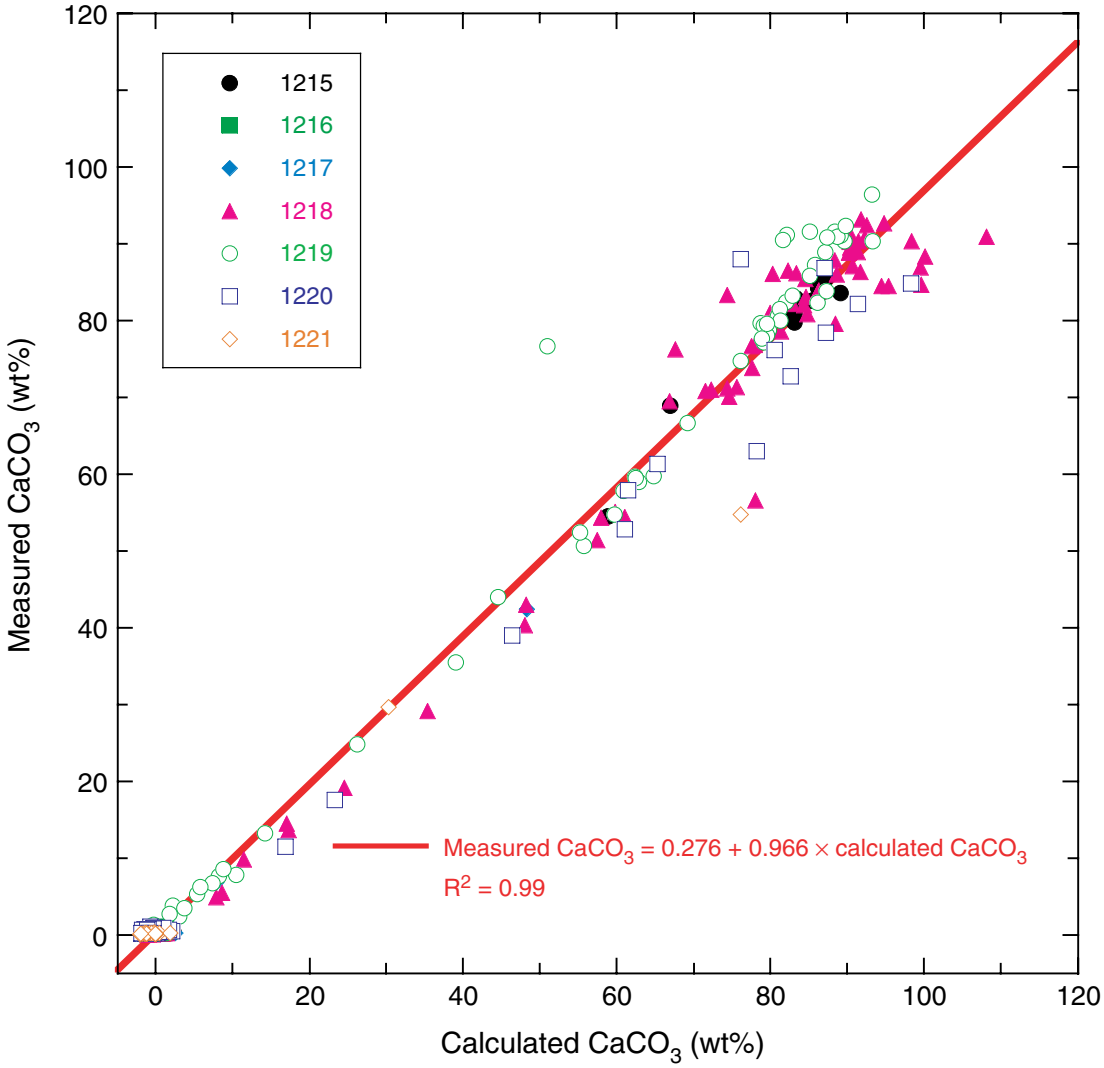

Figure F10. Schematic illustration of the configurations of tool strings used during Leg 199 (see Table T9, p. 70, for explanations of the acronyms).

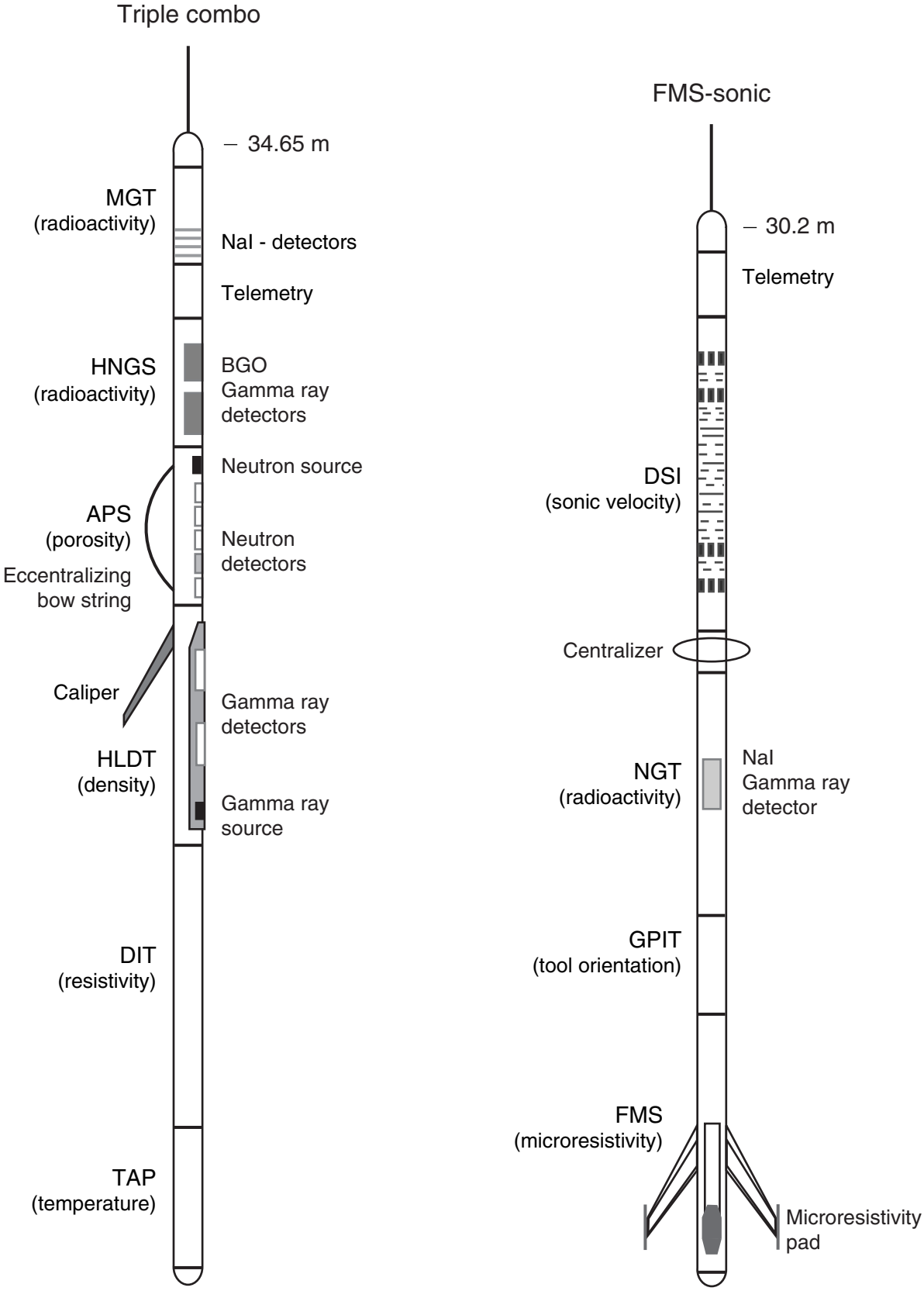

Table T1. Age estimates of calcareous nannofossil datum events. (See table notes. Continued on next page.)

Species event	Zone/Subzone (base)	Age (Ma)	Reference	Age (Ma)	Reference
B *Emiliania huxleyi*	CN15/NN21	**0.26**	1		
T *Pseudoemiliania lacunosa*	CN14b/NN20	**0.46**	1		
B *Gephyrocapsa parallela* (= reentrance medium G)		**0.95**	2		
B Medium *Gephyrocapsa*	CN13b	**1.69**	2		
Pliocene/Pleistocene boundary		**1.81**	3		
T *Discoaster brouweri*	CN13a/NN19	**1.95**	2		
T *Discoaster pentaradiatus*	CN12d/NN18	**2.52**	4		
T *Discoaster surculus*	CN12c/NN17	**2.63**	4		
T *Discoaster tamalis*	CN12b+c	**2.83**	4		
T *Sphenolithus* spp.	CN12aB*	**3.66**	5		
T *Reticulofenestra pseudoumbilicus*	CN12aA*/NN16	**3.80**	5		
T *Amaurolithus* spp.	CN11	**4.56**	5		
T *Ceratolithus acutus*	CN10c/NN13	**5.05**	6		
B *Ceratolithus rugosus*	CN10c/NN13	**5.10**	6		
T *Triquetrorhabdulus rugosus*		**5.23**	6		
Miocene/Pliocene boundary		**5.33**	7		
B *Ceratolithus acutus*	CN10b	**5.37**	6		
T *Discoaster quinqueramus*	CN10a/NN12	**5.54**	6		
T *Nicklithus amplificus*	CN9bC*	**6.00**	6		
B *Nicklithus amplificus*	CN9bB*	**6.84**	6		
B *Amaurolithus primus*	CN9bA*	**7.39**	6		
B *Discoaster berggrenii*	CN9a/NN11	**8.28**	6		
B *Discoaster loeblichii*	CN8b	**8.43**	5		
T *Discoaster hamatus*	CN8a/NN10	**9.63**	6		
T *Catinaster calyculus*		**9.64**	6		
T *Catinaster coalitus*		**9.69**	6		
B *Discoaster neohamatus*		**10.45**	6		
B *Discoaster hamatus*	CN7a/NN9	**10.48**	6		
B *Catinaster coalitus*	CN6/NN8	**10.79**	6		
TC *Discoaster kugleri*		**11.60**	6		
BC *Discoaster kugleri*	CN5b/NN7	**11.88**	6		
B *Triquetrorhabdulus rugosus*		**12.81**	5		
T *Cyclicargolithus floridanus*		**13.19**	5		
T *Sphenolithus heteromorphus*	CN5a/NN6	**13.55**	8		
T *Helicosphaera ampliaperta*	CN4/NN5	15.8	9	**15.10**	8
T Acme *Discoaster deflandrei*		16.2	5	**16.07**	8
B *Discoaster signus*		16.2	5		
B *Sphenolithus heteromorphus*	CN3	18.1	9	**17.70**	8
T *Sphenolithus belemnos*	CN3/NN4	18.4	9	**17.94**	8
T *Triquetrorhabdulus carinatus*	NN3	19.6	†		
B *Sphenolithus belemnos*	CN2	19.7	9	**18.90**	8
X *Helicosphaera euphratis/Helicosphaera carteri*				**20.80**	8
T Acme *Triquetrorhabdulus carinatus*		*22.9*	†		
B *Discoaster druggii*	CN1c/NN2	23.2	10		
B *Sphenolithus disbelemnos*		23.5	8	**22.67**	8
Oligocene/Miocene boundary		23.8	10	**22.90**	8
T *Sphenolithus delphix*		23.7	8	**22.98**	8
B *Sphenolithus delphix*		24.4	8	**23.24**	8
T *Sphenolithus ciperoensis*	CN1a	24.7	8	**24.14**	8
T Acme *Cyclicargolithus abisectus*	CN1b	*25.5*	†		
T *Sphenolithus distentus*	CP19b/NP25	26.5	11		
B *Sphenolithus ciperoensis*	CP19a/NP24	28.1	11		
T *Discoaster pseudoradians*		29.1	10		
B *Sphenolithus distentus*	CP18	30.4	11		
T *Reticulofenestra umbilicus* ≥14 µm	CP17/NP23	31.7	12		
T Acme *Ericsonia obruta*	CP16b	32.2	12		
T *Isthmolithus recurvus*		32.7	12		
T *Ericsonia formosa*	CP16c/NP22	32.9	12		
B Acme *Ericsonia obruta*		33.7	12		
Eocene/Oligocene boundary		33.7	10		
T *Discoaster saipanensis*	CP16a/NP21	34.0	12		
T *Discoaster barbadiensis*	CP16a	34.2	12		
T *Cribrocentrum reticulatum*		34.9	12		
T *Calcidiscus protoannulus*		35.4	12		

Table T1 (continued).

Species event	Zone/Subzone (base)	Age (Ma)	Reference	Age (Ma)	Reference
B *Isthmolithus recurvus*	NP19	36.6	12		
B *Chiasmolithus oamaruensis*	NP18	37.0	10		
T *Chiasmolithus grandis*	CP15	37.1	12		
B *Dictyococcites bisectus*		38.5	13		
B *Dictyococcites hesslandii*		40.3	12		
T *Chiasmolithus solitus*	CP14b/NP17	40.4	10		
T *Nannotetrina* spp.		42.3	12		
B *Reticulofenestra umbilicus* ≥14 µm	CP14a	42.5	12		
T *Blackites gladius*	NP16	43.4	10		
T *Nannotetrina fulgens*		43.4	14		
T *Chiasmolithus gigas*	CP13c	44.0	14		
B *Chiasmolithus gigas*	CP13b	46.1	10		
B *Nannotetrina fulgens*	CP13a/NP15	47.0	14		
T *Discoaster sublodoensis*		47.2	14		
B *Nannotetrina* spp.		47.8	14		
T *Discoaster lodoensis*		48.0	14		
B *Rhabdosphaera inflata*	CP12b	48.5	10		
B *Discoaster sublodoensis*	CP12a/NP14	49.3	14		
T *Tribrachiatus orthostylus*	NP13	51.0	14		
B *Toweius crassus*	CP11	51.5	10		
B *Discoaster lodoensis*	CP10/NP12	52.4	14		
T *Discoaster multiradiatus*		53.0	14		
B *Sphenolithus radians*		53.3	14		
X *Tribrachiatus contortus/Tribrachiatus orthostylus*	CP9b/NP11	53.4	14	53.400	‡
X *Tribrachiatus bramlettei/Tribrachiatus contortus*		53.7	14	53.875	‡
B *Discoaster diastypus*	CP9a	53.9	14		
B *Tribrachiatus bramlettei*	CP9a/NP10	53.9	14	54.359	‡
B *Rhomboaster cuspis*		54.1	14		
T *Fasciculithus* spp.		54.1	14		
Paleocene/Eocene boundary		55.0	15		
B *Campylosphaera eodela*	CP8b	55.5	10		
B *Discoaster multiradiatus*	CP8a/NP9	56.2	14		
B *Discoaster okadai*		56.4	14		
B *Discoaster nobilis*	CP7	56.5	14		
B *Heliolithus riedelii*	NP8	57.3	10		
B *Discoaster mohleri*	CP6/NP7	57.5	14		
B *Heliolithus kleinpellii*	CP5/NP6	58.2	14		
B *Sphenolithus anarrhopus*		58.4	10		
B *Heliolithus cantabriae*		58.8	14		
B *Fasciculithus pileatus*		59.3	14		
B *Fasciculithus tympaniformis*	CP4/NP5	59.7	10		
B *Fasciculithus* spp.		60.0	14		
B *Sphenolithus* spp.		60.7	14		

Notes: B = base, T = top, TC = top common, BC = base common, X = abundance cross-over. Bold = astrochronologically tuned datums. References: 1 = Thierstein et al., 1977; 2 = Raffi et al., 1993; 3 = Lourens et al., 1996; 4 = Tiedemann et al., 1994; 5 = Raffi and Flores, 1995; 6 = Backman and Raffi, 1997; 7 = Van Couvering et al., 2000; 8 = Shackleton et al., 1999; 9 = Backman et al. 1990; 10 = Berggren et al., 1995a; 11 = Olafsson and Villa, 1992; 12 = Backman, 1987; 13 = Monechi and Thierstein, 1985; 14 = Backman, 1986; 15 = carbon isotope excursion calibrated by astronomically tuning at ODP Site 1051 (Norris and Röhl, 1999). * = further subdivision of Subzones (CN12aB, etc.) according to Bukry (1991) and Raffi and Flores (1995). † = age estimate derived through calibration to magnetostratigraphy at Site 1218. ‡ = age estimate derived through counting of precessional cycles at Site 1215.

Table T2. Age estimates of planktonic foraminifer datum events. (**See table notes.** Continued on next two pages.)

Species event	Zone/ Subzone (base)	Age (Ma)	Reference
LO *Truncorotalia tosaensis*	PT1b	0.65	1
Pliocene/Pleistocene boundary		1.81	2
LO *Globigerinoides fistulosus*	PT1a	1.88	3
FO *Truncorotalia truncatulinoides*	N22	1.92	3
LO *Globorotalia pseudomiocenica* (Indo-Pacific only)	PL6	2.30	4
LO *Globoturborotalia woodi*		2.33	3
LO *Dentoglobigerina altispira*	PL5	3.11	3
LO *Sphaeroidinellopsis seminulina*	PL4	3.11	3
FO *Globigerinelloides fistulosus*		3.33	1
FO *Truncorotalia tosaensis*	N21	3.35	1
LO *Pulleniatina primalis*		3.65	1
LO *Globorotalia margaritae*	PL3	3.85	3
FO *Globorotalia crassaformis*		4.31	3
LO *Pulleniatina spectabilis*		4.33	5
LO *Globoturborotalita nepenthes*	PL2	4.39	3
LO *Globorotalia cibaoensis*	PL1b	4.60	4
Miocene/Pliocene boundary		5.33	6
FO *Sphaeroidinella dehiscens* s.l.	N19	5.54	3
FO *Globorotalia tumida*	N18/PL1a	5.82	3
LO *Globorotalia lenguaensis*	M14	6.00	4
FO *Pulleniatina primalis*		6.40	4
FO *Globorotalia conomiozea*		7.12 (6.9)	4
FO *Globigerinoides extremus*		8.58	3
FO *Globorotalia plesiotumida*	N17/M13b	8.58	3
FO *Neogloboquadrina acostaensis*	N16/M13a	9.82	3
LO *Paragloborotalia mayeri*	N15/M12	10.49	3
FO *Globoturborotalita nepenthes*	N14/M11	11.19	3
LO *Fohsella fohsi* s.l. (incl. *fohsi lobata* & *fohsi robusta*)	N13/M10	11.68	3
FO *Globorotalia lenguaensis*		12.85	3
FO *Fohsella fohsi robusta*		13.18	3
FO *Fohsella fohsi* s.l.	N12/M8	13.42	3
FO *Fohsella praefohsi*	N11	14.00	7
FO *Fohsella peripheroacuta*	N10/M7	14.70	7
FO *Orbulina* spp.	N9/M6	15.10	7
FO *Praeorbulina glomerosa*	M5b	16.10	7
FO *Praeorbulina sicana*	N8/M5a	16.40	7
FO *Globorotalia miozea*		16.70	4
LO *Catapsydrax dissimilis*	N7/M4a	17.30	7
FO *Globorotalia praescitula*		18.50	4
FO *Globigerinatella insueta*	N6/M3	18.80	4
LO *Globoquadrina binaiensis*		19.10	7
FO *Globigerinoides altiapertura*		20.50	4
LO *Tenuitella munda*		21.50	4
LO *Paragloborotalia kugleri*	N5/M2	21.50	4
FO *Globorotalia incognita*		21.60	4
LO *Paragloborotalia pseudokugleri*		21.60	4
LO *Globigerina angulisuturalis*		21.60	4
LO *Globoquadrina globularis*		22.80	4
FO *Globoquadrina dehiscens*	M1b	23.20	4
FO *Globigerinoides trilobus* s.l.		23.40	7
Oligocene/Miocene boundry		23.80	4
FO *Paragloborotalia kugleri*	N4/M1a	23.80	4
LO *Globigerina euapertura*		23.80	4
LO *Tenutitella gemma*		24.30	4
FO *Globigerinoides primordius* (common)		24.30	4
FO *Paragloborotalia pseudokugleri*		25.90	4
FO *Globigerinoides primordius*		26.70	4
LO *Globigerina labiacrassata*		27.10	4
LO *Paragloborotalia opima*	P22	27.10	4
LO *Chiloguembelina cubensis* (common)	P21b	28.50	4
FO *Globigerina angulisuturalis*	P21a	29.40	4
LO *Subbotina angiporoides*		30.00	4
LO *Globigerina ampliapertura*	P20	30.30	4
FO *Paragloborotalia opima*		30.60	4

Table T2 (continued).

Species event	Zone/ Subzone (base)	Age (Ma)	Reference
LO *Pseudohastigerina* spp.	P19	32.00	4
FO *Cassigerinella chipolensis*		33.65	4
Eocene/Oligocene boundary		33.70	4
LO *Hantkenina* spp.		33.70	4
LO *Turborotalia cerroazulensis*	P18	33.80	4
LO *Cribrohantkenina inflata*	P17	34.00	4
LO *Globigerinatheka index*		34.30	4
FO *Turborotalia cunialensis*	P16	35.20	4
LO *Turborotalia pomeroli*		35.30	4
LO *Globigerinatheka semiinvoluta*		35.30	4
FO *Cribrohantkenina inflata*		35.50	4
LO *Acarinina collactea*		37.70	4
LO *Subbotina linaperta*		37.70	4
LO *Morozovella spinulosa*		38.10	4
FO *Globigerinatheka semiinvoluta*	P15	38.40	4
LO *Planorotalites* spp.		38.50	4
LO *Acarinina primitiva*		39.00	4
LO *Subbotina frontosa*		39.30	4
LO *Globigerinatheka beckmanni*	P14	40.10	4
FO *Globigerinatheka beckmanni*	P13	40.50	4
LO *Acarinina bullbrooki*		40.50	4
FO *Turborotalia pomeroli*		42.40	4
FO *Globigerinatheka* index		42.90	4
FO *Morozovella lehneri*		43.50	4
LO *Morozovella aragonensis*	P12	43.60	4
FO *Globigerinatheka kugleri*	P11	45.80	4
FO *Turborotalia possagnoensis*		46.00	4
FO *Hantkenina nuttalli*	P10	49.00	4
FO *Planorotalites palmerae*	P9	50.40	4
LO *Morozovella formosa*	P8	50.80	4
FO *Acarinina pentacamerata*		50.80	4
FO *Morozovella aragonensis*	P7	52.30	4
LO *Morozovella marginodentata*		52.50	4
LO *Morozovella lensiformis*		52.70	4
LO *Subbotina velascoensis*		53.50	4
LO *Morozovella aequa*		53.60	4
FO *Morozovella formosa*	P6b	54.00	4
FO *Morozovella lensiformis*		54.00	4
LO *Morozovella velascoensis*	P6a	54.70	4
LO *Morozovella acuta*		54.70	4
FO *Morozovella gracilis*		54.70	4
FO *Igorina broedermanni*		54.70	4
FO *Morozovella marginodentata*		54.80	4
Paleocene/Eocene boundary		55.00	8
FO *Globanomalina australiformis*		55.50	4
FO *Morozovella subbotinae*		55.90	4
LO *Globanomalina pseudomenardii*	P5	55.90	4
LO *Acarinina nitida* (= *A. acarinata*)		56.30	4
LO *Acarinina mckannai*		56.30	4
FO *Acarinina soldadoensis*	P4c	56.50	4
FO *Acarinina coalingensis* (= triplex)		56.50	4
FO *Morozovella aequa*		56.50	4
LO *Acarinina subsphaerica*	P4b	57.10	4
FO *Acarinina mckannai*		59.10	4
FO *Acarinina subsphaerica*		59.20	4
FO *Acarinina nitida*		59.20	4
FO *Globanomalina pseudomenardii*	P4a	59.20	4
LO *Parasubbotina variospira*		59.20	4
LO *Parasubbotina varianta*		59.20	4, 9
FO *Morozovella velascoensis*		60.00	4
FO *Igorina albeari*	P3b	60.00	4
FO *Acarinina strabocella*		60.50	9
FO *Morozovella conicotruncata*		60.90	4
FO *Morozovella angulata*	P3a	61.00	4
FO *Igorina pusilla*		61.00	4
FO *Praemurica praeangulata*		61.20	4
FO *Praemurica uncinata*	P2	61.20	4

Table T2 (continued).

Species event	Zone/ Subzone (base)	Age (Ma)	Reference
FO *Globoanomalina imitata*		61.30	4
FO *Globanomalina compressa*	P1c	63.00	4
FO *Praemurica inconstans*		63.00	4
FO *Parasubbotina varianta*		63.00	4
FO *Subbotina triloculinoides*	P1b	64.50	4
LO *Parvularugoglobigerina extensa*		64.90	9
LO *Parvularugoglobigerina eugubina*	P1a	64.90	4
FO *Parvularugoglobigerina eugubina*	Pa	64.97	4

Notes: FO = first occurrence, LO = last occurrence. 1 = Berggren et al., 1995b; 2 = Lourens et al., 1996; 3 = Chaisson and Pearson, 1997; 4 = Berggren et al., 1995a; 5 = Shackleton et al., 1995; 6 = Van Couvering et al., 2000; 7 = Pearson and Chaisson, 1997; 8 = Norris and Röhl, 1999; 9 = Olsson et al., 1999. This table is also available in **ASCII.**

Table T3. Age estimates of radiolarian datum events. (**See table notes.** Continued on next three pages.)

Epoch/ Age (Ma)	Standard tropical zonation	Code number	Event	Age* (Ma)	Reference
	B. invaginata	RN17	**FO *Buccinosphaera invaginata***	0.18	1
	C. tuberosa	RN16	**LO *Stylatractus universus***	0.42	2
	S. universus	RN15	**FO *Collosphaera tuberosa***	0.61	2
Pleistocene	*A. ypsilon*	RN14	LO *Pterocorys campanula*	0.80	3
			FO *Pterocorys hertwigii*	0.75	3
			LO *Anthocyrtidium angulare*	1.12	2
	A. angulare	RN13	FO *Lamprocyrtis nigriniae*	1.55	3
			LO *Lamprocyrtis heteroporos*	1.30	3
1.81			**LO *Pterocanium prismatium***	1.74	2
	P. prismatium	RN12	FO *Anthocyrtidium angulare*	1.80	3
			LO *Theocorythium vetulum*	1.40	3
			LO *Anthocyrtidium jenghisi*		
late Pliocene			FO *Cycladophora davisiana*		
			FO *Lamprocyrtis heteroporos*		
			FO *Theocorythium trachelium trachelium*	1.60	3
			LO *Stichocorys peregrina*	2.74	2
	L. audax	RN1	*Didymocyrtis avita* → *D. tetrathalamus*		
3.58			LO *Phormostichoartus fistula*	3.35	3
			LO *Lychnodictyum audax*	3.60	3
			LO *Phormostichoartus doliolum*	3.87	2
	P. doliolum	RN10	FO *Amphirhoplaum ypsilon*	4.00	3
			Spongaster pentas → *S. tetras tetras*	4.10	3
early Pliocene			LO *Spongaster berminghami*	4.70	3
			LO *Didymocyrtis penultima*	4.19	2
	S. Peregrina	RN9	*Didymocyrtis penultima* → *D. avita*		
			FO *Pterocanium prismatium*	4.90	3
			LO *Solenosphaera omnitubus procera*	5.30	3
5.33			LO *Solenosphaera omnitubus omnitubus*	5.30	3
			Spongaster berminghami → *S. pentas*		
			LO *Siphostichartus corona*	5.60	3
			FO *Pterocorys campanula*		
			LO *Acrobotrys tritubus*	6.00	3
			LO *Calocycletta (Calocyclior) caepa*	6.20	3
			LO *Stichocorys johnsoni*	6.60	3
			LO *Calocycletta (Calocycletta) cladara*		
			Stichocorys delmontensis* → *S. peregrina	6.71	2
	D. penultima	RN8	FO *Solenosphaera omnitubus omnitubus*	7.30	3
			FO *Solenosphaera omnitubus procera*	7.30	3
late Miocene			*Didymocyrtis antepenultima* → *D. penultima*		
			LO *Diartus hughesi*	7.70	2
	D. antepenultima	RN7	LO *Dictyocoryne ontongensis*		
			FO *Acrobotrys tritubus*	7.90	3
			LO *Botryostrobus miralestensis*	8.20	3
			FO *Spongaster berminghami*	8.30	3
			Didymocyrtis laticonus → *D. antepenultima*		
			Diartus petterssoni* → *D. hughesi	8.77	2
	D. petterssoni	RN6	*Lithopera neotera* → *L. bacca*	8.80	3
			LO *Stichocorys wolffii*	8.80	3
			LO *Cyrtocapsella japonica*	9.80	3
11.19			LO *Lithopera thornburgi*		
			LO *Cyrtocapsella cornuta*	12.10	3
			LO *Cyrtocapsella tetrapera*	12.10	3
			LO *Carpocanopsis cristata*	10.60	3
			FO *Phormostichoartus doliolum*	8.80	3
			LO *Dorcadospyris alata*	13.60	3
			LO *Liriospyris parkerae*		
			FO *Cyrtocapsella japonica*		
			Calocycletta virginis → *C. cladara*		
			FO *Diartus petterssoni*	[11.95]	2
middle Miocene	*D. alata*	RN5	LO *Carpocanopsis bramlettei*	14.70	3
			Lithopera renzae → *L. neotera*	12.10	3
			Didymocyrtis mammifera → *D. laticonus*		
			FO *Lithopera thornburgi*		
			FO *Phormostichoartus corbula*		
			FO *Dictyocoryne ontongensis*		
			LO *Calocycletta costata*	15.00	3
			LO *Didymocyrtis tubaria*		
			LO *Didymocyrtis violina*		
			FO *Lithopera renzae*		

Table T3 (continued).

Epoch/ Age (Ma)	Standard tropical zonation	Code number	Event	Age* (Ma)	Reference
middle Miocene	*D. alata*	RN5	LO *Dorcadospyris forcipata* ***Dorcadospyris dentata → D. alata***	15.68	2
16.4	*C. Costata*	RN4	LO *Eucyrtidium diaphanes* *Liriospyris stauropora → L. parkerae* *Carpocanopsis favosa* LO *Didymocyrtis prismatica* LO *Carpocanopsis cingulata* FO *Carpocanopsis cristata* LO *Lychnocanoma elongata* **FO *Calocycletta costata***	17.03	4
early Miocene	*S. wolffii*	RN3	FO *Didymocyrtis mammifera* FO *Calocycletta caepa* FO *Dorcadospyris dentata* FO *Liriospyris stauropora* LO *Dorcadopsyris ateuchus* FO *Siphostichartus corona* **FO *Stichocorys wolffii***	17.92	4
	S. delmontensis	RN2	FO *Didymocyrtis tubaria* FO *Didymocyrtis violina* FO *Stichocorys delmontensis* FO *Carpocanopsis bramlettei* **LO *Theocyrtis annosa***	20.53	4
	C. tetrapera	RN1	LO *Calocycletta serrata* LO *Calocycletta robusta* FO *Carpocanopsis favosa* FO *Cyrtocapsella cornuta* FO *Calocycletta serrata* FO *Calocycletta virginis* FO *Botryostrobus miralestensis* **FO *Cyrtocapsella tetrapera***	23.62	5
23.80					
late Oligocene	*L. elongata*	RP22	LO *Artophormis gracilis*	23.94	6
			FO *Eucyrtidium diaphanes*	23.94	6
			LO *Dorcadospyris papilio* FO *Carpocanopsis cingulata* **FO *Lychnocanoma elongata***	24.60	6
	D. atuechus	RP21	FO *Dorcadospyris forcipata* LO *Lychnocanomma trifolium* FO *Calocycletta robusta* LO *Dorcadospyris circulus*		5
28.5			FO *Dorcadospyris papilio* LO *Lithocyclia angusta* ***Tristylospyris triceros → D. ateuchus***	~28.8	7
early Oligocene	*T. tuberosa*	RP20	FO *Theocyrtis annosa* LO *Theocyrtis tuberosa* FO *Dorcadospyris circulus*		5
			LO *Lithocyclia crux* FO *Lychnocanoma trifolium* FO *Didymocyrtis prismatica* LO *Dorcadospyris pseudopapilio* *Centrobotrys petrushevskayae → C. thermophila* FO *Lychnodictyum audax* *Centrobotrys gravida → C. petrushevskayae* FO *Dorcadospyris pseudopapilio* FO *Lithocyclia crux* *Artophormis barbadensis → A. gracilis* FO *Centrobotrys gravida* LO *Dictyoprora pirum* FO *Phormostichoartus fistula* LO *Cryptocarpium ornatum* LO *Dictyoprora mongolfieri* LO *Lychnocanoma amphitrite* ***Lithocyclia aristotelis → L. angusta***	~32.8	7

Table T3 (continued).

Epoch/ Age (Ma)	Standard tropical zonation	Code number	Event	Age* (Ma)	Reference
	C. ornatum	RP19	LO *Dictyoprora armadillo* LO *Lophocyrtis jacchia* LO *Calocyclas turris* LO *Thyrsocyrtis bromia* LO *Thyrsocyrtis rhizodon* LO *Cryptocarpium azyx* LO *Thyrsocyrtis lochites* LO *Calocyclas bandyca* LO *Calocyclas hispida* LO *Lychnocanoma bellum* LO *Podocyrtis papalis*		
33.7 late Eocene			**LO *Thyrsocyrtis tetracantha***	~34.9	7
	C. bandyca	RP18	LO *Thyrsocyrtis triacantha* FO *Theocyrtis tuberosa* LO *Eusyringium fistuligerum* LO *Podocyrtis goetheana*		
			FO *Calocyclas bandyca*	~36.4	7
37.0	*C. azyx*	RP17	LO *Podocyrtis chalara* FO *Lychnocanoma amphitrite* *Calocyclas hispida* → *Calocyclas turris*		
			FO *Cryptocarpium azyx*	~37.7	7
	P. goetheana	RP16	LO *Spongatractus pachystylus* FO *Thyrsocyrtis bromia* FO *Thyrsocyrtis tetracantha* FO *Dictyoprora pirum* LO *Theocotylissa ficus* LO *Sethochytris triconiscus* FO *Dictyorprora armadillo*		
			FO *Podocyrtis goetheana*	~38.8	7
	P. chalara	RP15	LO *Podocyrtis trachodes* LO *Phormocyrtis striata striata* FO *Tristylospyris triceros*		
			Podocyrtis mitra* → *P. chalara	~39.5	7
	P. mitra	RP14	FO *Cryptocarpium ornatum* LO *Podocyrtis ampla* LO *Eusyringium lagena* FO *Artophormis barbadensis* FO *Thyrsocyrtis lochites* FO *Sethochytris triconiscus* LO *Podocyrtis fasciolata* LO *Podocyrtis helenae*		
			Podocyrtis sinuosa* → *P. mitra	~42.8	7
middle Eocene	*P. ampla*	RP13	FO *Podocyrtis trachodes* LO *Podocyrtis dorus* *Eusyringium lagena* → *E. fistuligerum* FO *Podocyrtis fasciolata* FO *Podocyrtis helenae* LO *Theocotyle venezuelensis*		
			Podocyrtis phyxis* → *P. ampla	~44.5	7
	T. triacantha	RP12	FO *Eusyringium fistuligerum* LO *Theocotyle nigriniae* LO *Theocotyle conica* *Podocyrtis diamesa* → *P. phyxis* LO *Theocorys anaclasta* LO *Lamptonium fabaeforme constrictum* LO *Lamptonium fabaeforme chaunothroax* LO *Thyrsocyrtis hirsuta* LO *Thyrsocyrtis robusta* *Thyrsocyrtis tensa* → *T. triacantha*		
			FO *Eusyringium lagena*	~47.5	7
	D. mongolfieri	RP11	LO *Lamptonium fabaeforme fabaeforme* FO *Podocyrtis dorus* *Theocotyle cryptocephala* → *T. conica* LO *Calocycloma castum*		
			FO *Dictyoprora mongolfieri*	~48.5	7

Table T3 (continued).

Epoch/ Age (Ma)	Standard tropical zonation	Code number	Event	Age* (Ma)	Reference
middle Eocene	*T. cryptocephala*	RP10	*Podocyrtis acalles* → *P. sinuosa* FO *Thyrsocyrtis robusta* FO *Theocotyle venezuelensis* LO *Buryella clinata* ***Theocotyle nigriniae* → *T. cryptocephala***	~49.0	7
49.0					
early Eocene	*P. striata striata*	RP9	*Spongatractis bablis* → *S. pachystylus* LO *Lamptonium sanfilippoae* FO *Thyrsocyrtis rhizodon* FO *Podocyrtis diamesa* FO *Lamptonium fabaeforme constrictum* *Phormocyrtis striata exquisita* → *P. striata striata* FO *Podocyrtis acalles* LO *Phormocyrtis cubensis* FO *Lychnocanoma bellum* **FO *Theocorys anaclasta***	~50.3	7
early Eocene	*B. clinata*	RP8	LO *Pterocodon* (?) *ampla* LO *Bekomma bidartensis* LO *Buryella tetradica* LO *Thyrsocyrtis tarsipes* FO *Lithocyclia ocellus* gp. FO *Thyrsocyrtis tensa* *Theocotylissa alpha* → *T. ficus* FO *Calocyclas hispida* FO *Spongatractus balbis* FO *Lamptonium sanfilippoae* FO *Theocotyle nigriniae* FO *Thyrsocyrtis hirsuta* ***Pterocodon* (?) *anticlinata* → *Buryella clinata***	~52.85	7
55.0	*B. bidartensis*	RP7	FO *Theocotylissa alpha* FO *Lamptonium fabaeforme chaunothorax* FO *Pterodocon* (?) *anteclinata* FO *Lophocyrtis jacchia* FO *Calocycloma castum* *Lamptonium pennatum* → *L. fabaeforme fabaeforme* FO *Podocyrtis papalis* LO *Bekomma campechensis* **FO *Bekomma bidartensis***	~56.9	7
late Paleocene	*B. campechensis*	RP6	FO *Phormocyrtis cubensis* LO *Buryella pentadica* FO *Pterocodon* (?) *ampla* **FO *Bekomma campechensis***	~60.2	8
61.0		RP5	**FO *Buryella tetradica***	~60.9	9
early Paleocene		RP4	**FO *Buryella foremanae***	~62.8	9
		RP3	**FO *Stichomitra granulata***	~63.9	9
		RP2	**FO *Amphisphaera kina***	~64.6	9
		RP1	**FO *Amphisphaera aotea***	~65.1	9

Notes: FO = first morphotypic occurrence, LO = last morphotypic occurrence. → = an evolutionary transition. * = Cande and Kent, 1995. The age for the morphotypic first occurrence of *Diartus petterssoni* (base RN7) is a demonstrably diachronous event (Johnson and Nigrini, 1985). Brackets = approximately synchronous events. Bold = taxa that define the base of radiolarian zones. The assigned numerical ages should be used with caution because they are approximations only. For the Paleogene record, a combination of data from Sanfilippo and Nigrini (1995, 1996) and an integrated compilation chart (unpublished) based on published data from DSDP/ODP Legs 1–135 have been used to approximate the ages of zonal boundaries. (It is expected that results from Leg 199 will greatly improve the accuracy of these ages. See the **"Leg 199 Summary"** chapter) References: 1 = Johnson et al., 1989; 2 = Shackleton et al., 1995b; 3 = Lazarus et al., 1995; 4 = Sanfilippo and Nigrini, 1996; 5 = Sanfilippo and Nigrini, 1995; 6 = A. Sanfilippo and C. Nigrini (unpubl. data) (an integrated compilation based on published DSDP/ODP Legs 1–135); 7 = Nishimura, 1992; 8 = Hollis, 1993; 9 Nigrini and Sanfilippo, 2001. This table is also available in **ASCII.**

Table T4. Ages used for the geomagnetic polarity timescale (normal polarity interval).

Interval (Ma)		Chron/	
Top	Bottom	Subchron	Reference
0.000	0.780	C1n	1
0.990	1.070	C1r.1n	1
1.201	1.211	C1r.2n	1
1.770	1.950	C2n	1
2.581	3.040	C2An.1n	1, 2
3.110	3.220	C2An.2n	2
3.330	3.580	C2An.3n	2
4.180	4.290	C3n.1n	2
4.480	4.620	C3n.2n	2
4.800	4.890	C3n.3n	2
4.980	5.230	C3n.4n	2, 3
5.875	6.122	C3An.1n	3
6.256	6.555	C3An.2n	3
6.919	7.072	C3Bn	3
7.135	7.170	C3Br.1n	3
7.341	7.375	C3Br.2n	3
7.406	7.533	C4n.1n	3
7.618	8.027	C4n.2n	3
8.174	8.205	C4r.1n	3
8.631	8.945	C4An	3
9.142	9.218	C4Ar.1n	3
9.482	9.543	C4Ar.2n	3
9.639	9.880	C5n.1n	3
9.920	10.839	C5n.2n	3
10.943	10.991	C5r.1n	3
11.343	11.428	C5r.2n	3
11.841	11.988	C5An.1n	3
12.096	12.320	C5An.2n	3
12.605	12.637	C5Ar.1n	3
12.705	12.752	C5Ar.2n	3
12.929	13.083	C5AAn	3
13.252	13.466	C5ABn	3
13.666	14.053	C5ACn	3
14.159	14.607	C5ADn	3
14.800	14.888	C5Bn.1n	3, 4
15.034	15.155	C5Bn.2n	4
16.014	16.293	C5Cn.1n	4
16.327	16.488	C5Cn.2n	4
16.556	16.726	C5Cn.3n	4
17.277	17.615	C5Dn	4
18.281	18.781	C5En	4
19.048	20.131	C6n	4
20.518	20.725	C6An.1n	4
20.996	21.320	C6An.2n	4
21.768	21.859	C6AAn	4
22.151	22.248	C6AAr.1n	4
22.459	22.493	C6AAr.2n	4
22.588	22.750	C6Bn.1n	4
22.804	23.069	C6Bn.2n	4
23.353	23.535	C6Cn.1n	4
23.677	23.800	C6Cn.2n	4
23.999	24.118	C6Cn.3n	4
24.730	24.781	C7n.1n	4
24.835	25.183	C7n.2n	4
25.496	25.648	C7An	4
25.823	25.951	C8n.1n	4
25.992	26.554	C8n.2n	4
27.027	27.972	C9n	4
28.283	28.512	C10n.1n	4
28.578	28.745	C10n.2n	4
29.401	29.662	C11n.1n	4
29.765	30.098	C11n.2n	4
30.479	30.939	C12n	4
33.058	33.545	C13n	4
34.655	34.940	C15n	4
35.343	35.526	C16n.1n	4
35.685	36.341	C16n.2n	4
36.618	37.473	C17n.1n	4
37.604	37.848	C17n.2n	4
37.920	38.113	C17n.3n	4
38.426	39.552	C18n.1n	4
39.631	40.130	C18n.2n	4
41.257	41.521	C19n	4
42.536	43.789	C20n	4
46.264	47.906	C21n	4
49.037	49.714	C22n	4
50.778	50.946	C23n.1n	4
51.047	51.743	C23n.2n	4
52.364	52.663	C24n.1n	4
52.757	52.801	C24n.2n	4
52.903	53.347	C24n.3n	4
55.904	56.391	C25n	4
57.554	57.911	C26n	4
60.920	61.276	C27n	4
62.499	63.634	C28n	4
63.976	64.745	C29n	4

Note: References: 1 = Shackleton et al., 1990; 2 = Hilgen, 1991a, 1991b; 3 = Shackleton et al., 1995b; 4 = Cande and Kent, 1995. This table is also available in **ASCII.**

Table T5. Example of composite depth tables found in each site chapter.

Core	Length (m)	Depth (mbsf)	Offset (m)	Depth (mcd)
199-1218A-				
1H	8.2	0.0	0.00	0.00
2H	9.5	8.2	0.78	8.98
3H	9.5	17.7	2.34	20.04
4H	9.5	27.2	4.42	31.62
5H	9.5	36.7	4.80	41.50
6H	9.5	46.2	6.84	53.04
7H	9.5	55.7	8.06	63.76
8H	9.5	65.2	7.96	73.16
9H	9.5	74.7	10.26	84.96
10H	9.5	84.2	11.90	96.10
11H	9.5	93.7	13.40	107.10
12H	9.5	103.2	14.47	117.67
13H	9.5	112.7	14.91	127.61
14H	9.5	122.2	15.42	137.62
15H	9.5	131.7	16.22	147.92
16H	9.5	141.2	17.84	159.04
17H	9.5	150.7	17.90	168.60
18H	9.5	160.2	20.56	180.76
19H	9.5	169.7	20.38	190.08
20H	9.5	179.2	22.28	201.48
22X	9.6	195.9	22.30	218.20
23X	9.6	205.5	23.24	228.74
24X	9.6	215.1	25.08	240.18
25X	9.6	224.7	26.27	250.97
26X	9.6	234.3	26.07	260.37
27X	9.6	243.9	26.13	270.03
28X	9.6	253.5	23.93	277.43
29X	7.6	263.1	24.23	287.33
30X	6.1	270.7	24.23	294.93
199-1218B-				
1H	3.9	0.0	0.00	0.00
2H	9.5	3.9	1.16	5.06
3H	9.5	13.4	3.82	17.22
4H	9.5	22.9	5.18	28.08
5H	9.5	32.4	5.66	38.06
6H	9.5	41.9	7.66	49.56
7H	9.5	51.4	7.29	58.69
8H	9.5	60.9	8.39	69.29
9H	9.5	70.4	8.34	78.74
10H	9.5	79.9	10.80	90.70
11H	9.5	89.4	13.38	102.78
12H	9.5	98.9	15.24	114.14
13H	9.5	108.4	15.49	123.89
14H	9.5	117.9	16.46	134.36
15H	9.5	127.4	17.82	145.22
16H	9.5	136.9	19.02	155.92
17H	9.5	146.4	19.78	166.18
18H	9.5	155.9	20.12	176.02
19X	9.7	165.4	19.04	184.44
20X	9.7	175.1	20.70	195.80
21X	9.6	184.8	22.52	207.32
22X	9.7	194.4	23.02	217.42
23X	9.6	204.1	23.78	227.88
24X	9.6	213.7	26.46	240.16
25X	5	223.3	28.13	251.43
26X	9.6	228.3	27.61	255.91
27X	9.6	237.9	29.13	267.03
28X	9.7	247.5	30.53	278.03
29X	6.3	257.2	30.63	287.83
199-1218C-				
1H	9.5	55.0	8.04	63.04
2H	9.5	64.5	9.36	73.86
3H	9.5	74.0	9.78	83.78
4H	9.5	83.5	11.58	95.08
5H	9.5	93.0	12.82	105.82
6H	9.5	102.5	15.58	118.08
7H	9.5	112.0	14.09	126.09
8H	9.5	121.5	14.47	135.97
9H	9.5	131.0	15.90	146.90
10H	9.5	144.5	17.84	162.34
11H	9.5	154.0	18.62	172.62
12X	8.5	163.5	19.78	183.28
13X	9.6	172.0	19.76	191.76
14X	9.6	181.6	19.81	201.41
15X	9.6	191.2	21.92	213.12
16X	9.6	200.8	23.90	224.70
17X	9.6	210.4	23.46	233.86
18X	9.6	223.0	24.42	247.42
19X	9.6	232.6	24.93	257.53
20X	5	242.2	27.45	269.65
21X	9.6	247.2	27.57	274.77

Table T6. Example of splice tie points table found in each site chapter.

Hole, core, section, interval (cm)	Depth (mbsf)	Depth (mcd)		Hole, core, section, interval (cm)	Depth (mbsf)	Depth (mcd)
199-				199-		
1218A-1H-1, 0			Start			
1218A-1H-5, 54	6.54	6.54	Tie to	1218B-2H-1, 148	5.38	6.54
1218B-2H-5, 40	10.30	11.46	Tie to	1218A-2H-2, 97	10.68	11.46
1218A-2H-7, 6	17.26	18.04	Tie to	1218B-3H-1, 82	14.22	18.04
1218B-3H-5, 12	19.52	23.34	Tie to	1218A-3H-3, 30	21.00	23.34
1218A-3H-6, 132	26.52	28.86	Tie to	1218B-4H-1, 78	23.68	28.86
1218B-4H-4, 120	28.60	33.78	Tie to	1218A-4H-2, 66	29.36	33.78
1218A-4H-6, 132	36.02	40.44	Tie to	1218B-5H-2, 88	34.78	40.44
1218B-5H-5, 44	38.84	44.50	Tie to	1218A-5H-2, 150	39.70	44.50
1218A-5H-7, 20	45.90	50.70	Tie to	1218B-6H-1, 113	43.04	50.70
1218B-6H-4, 60	47.00	54.66	Tie to	1218A-6H-2, 12	47.82	54.66
1218A-6H-6, 88	54.58	61.42	Tie to	1218B-7H-2, 128	54.13	61.42
1218B-7H-5, 56	57.91	65.20	Tie to	1218A-7H-1, 144	57.14	65.20
1218A-7H-6, 8	63.28	71.34	Tie to	1218B-8H-2, 54.5	62.95	71.34
1218B-8H-5, 76	67.66	76.05	Tie to	1218A-8H-2, 138.5	68.09	76.05
1218A-8H-5, 112	72.32	80.28	Tie to	1218B-9H-2, 3	71.94	80.28
1218B-9H-6, 118	79.08	87.42	Tie to	1218A-9H-2, 96	77.16	87.42
1218A-9H-6, 112	83.32	93.58	Tie to	1218B-10H-2, 138	82.78	93.58
1218B-10H-6, 126	88.66	99.46	Tie to	1218A-10H-3, 36	87.56	99.46
1218A-10H-6, 92	92.62	104.52	Tie to	1218B-11H-2, 24	91.14	104.52
1218B-11H-6, 144	98.34	111.72	Tie to	1218A-11H-4, 12	98.32	111.72
1218A-11H-6, 136	102.56	115.96	Tie to	1218B-12H-2, 32	100.72	115.96
1218B-12H-5, 144	106.34	121.58	Tie to	1218A-12H-3, 90.5	107.11	121.58
1218A-12H-5, 112	110.32	124.79	Tie to	1218B-13H-1, 90	109.30	124.79
1218B-13H-6, 44	116.34	131.83	Tie to	1218A-13H-3, 122	116.92	131.83
1218A-13H-6, 44	120.64	135.55	Tie to	1218B-14H-1, 118.5	119.09	135.55
1218B-14H-4, 66	123.06	139.52	Tie to	1218A-14H-2, 36	124.10	139.52
1218A-14H-6, 104	130.74	146.16	Tie to	1218B-15H-1, 94	128.34	146.16
1218B-15H-4, 40	132.30	150.12	Tie to	1218A-15H-2, 69	133.90	150.12
1218A-15H-7, 48	141.18	157.40	Tie to	1218B-16H-1, 148	138.38	157.40
1218B-16H-6, 40	144.30	163.32	Tie to	1218A-16H-3, 128	145.48	163.32
1218A-16H-6, 64	149.34	167.18	Tie to	1218B-17H-1, 99	147.40	167.18
1218B-17H-6, 46	154.36	174.14	Tie to	1218C-11H-2, 0	155.52	174.14
1218C-11H-5, 58	160.58	179.20	Tie to	1218B-18H-3, 18	159.08	179.20
1218B-18H-5, 118	163.08	183.20	Tie to	1218A-18H-2, 94	162.64	183.20
1218A-18H-5, 8	166.20	186.76	Tie to	1218C-12X-3, 48	166.98	186.76
1218C-12X-6, 28	171.28	191.06	Tie to	1218A-19H-1, 98	170.68	191.06
1218A-19H-6, 76	177.96	198.34	Tie to	1218B-20X-2, 103	177.64	198.34
1218B-20X-5, 120	182.30	203.00	Tie to	1218A-20H-1, 152	180.72	203.00
1218A-20H-6, 92	187.62	209.90	Tie to	1218B-21X-2, 108	187.38	209.90
1218B-21X-6, 66	192.96	215.48	Tie to	1218C-15X-2, 85	193.56	215.48
1218C-15X-4, 76	196.46	218.38	Tie to	1218B-22X-1, 96	195.36	218.38
1218B-22X-7, 20	203.23	226.25	Tie to	1218C-16X-2, 4.5	202.35	226.25
1218C-16X-5, 6	206.86	230.76	Tie to	1218A-23X-2, 52	207.52	230.76
1218A-23X-5, 92	212.42	235.66	Tie to	1218C-17X-2, 30	212.20	235.66
1218C-17X-6, 12	217.72	241.18	Tie to	1218B-24X-1, 101	214.72	241.18
1218B-24X-6, 94	222.14	248.60	Tie to	1218C-18X-1, 118	224.18	248.60
1218C-18X-7, 32	231.89	256.31	Tie to	1218B-26X-1, 40	228.70	256.31
1218B-26X-5, 96	234.76	262.37	Tie to	1218A-26X-2, 50	236.30	262.37
1218A-26X-6, 6	241.86	267.93	Tie to	1218B-27X-1, 90	238.80	267.93
1218B-27X-6, 132	246.72	275.85	Tie to	1218C-21X-1, 108	248.28	275.85
1218C-21X-3, 106	251.26	278.83	Tie to	1218A-28X-1, 139	254.90	278.83
1218A-28X-7, 74	262.74	286.67	Append to	1218A-29X-1, 0	263.10	287.33
1218A-29X-4, 88	268.48	292.71	Append to	1218A-30X-1, 0	270.70	294.93
1218A-30X-2, 140	273.60	297.83	End			

Table T7. Reproducibility for analytical determinations, Leg 199.

Parameter	Method	Reproducibility
Interstitial water:		
Alkalinity	Gran titration	±1.5%
Cl^-	Titration with AgCl	±0.1%
K^+	Ion chromatography	±0.02%
Mg^{2+}	Ion chromatography	±0.1%
Ca^{2+}	Ion chromatography	±0.2%
SO_4^{2-}	Ion chromatography	±0.1%
$Si(OH)_4$	Spectrophotometry	±0.9%
NH_4^+	Spectrophotometry	±4 µM
Mn^{2+}	ICP-AES	±3.9%
Li^+	ICP-AES	±3.0%
Sr^{2+}	ICP-AES	±4.8%
Ba^{2+}	ICP-AES	±4.0%
B	ICP-AES	±1.49%
Bulk sediments:		
Ba	ICP-AES	±21.3%
Ca	ICP-AES	±11.5%
Fe	ICP-AES	±9.2%
Mn	ICP-AES	±8.1%
Si	ICP-AES	±3.3%
Ti	ICP-AES	±21.7%
Al	ICP-AES	±5.1%
Mg	ICP-AES	±12.7%
P	ICP-AES	±32.9%
Sr	ICP-AES	±14.7%

Notes: ICP-AES = inductively coupled plasma–atomic emission spectroscopy. Because absolute concentrations of NH_4^+ measured during Leg 199 were so small, relative to typical NH_4^+ concentrations, reporting reproducibility relative to these low, measured concentrations would be exaggerated. Therefore, we report reproducibility in absolute concentration units.

Table T8. Measurements made by wireline tool strings.

Tool string	Tool*	Measurement	Sampling interval (cm)	Approximate vertical resolution
Triple combination	HNGS†	Spectral gamma ray	15	51
	APS	Porosity	5 and 15	43
	HLDT	Bulk density	2.5	38
	DIT/DLL	Resistivity	15	200/150/76,61(DLL)
	TAP	Temperature	1 per s	NA
		Tool acceleration	4 per s	NA
		Pressure	1 per s	NA
	MGT‡	Gamma ray	15	15
Formation MicroScanner	NGT	Spectral gamma ray	15	46
FMS-sonic combination	GPIT	Tool orientation	0.25 and 15	NA
	FMS	Microresistivity	0.25	0.5
	DSI/SDT/LSS/BHC	Acoustic velocity	15	107/120/61/61

Notes: * = for additional information about tool physics and use consult ODP Logging Services at **www.ldeo.columbia.edu/BRG/ODP**. † = see Table **T9,** p. 70,for explanations of acronyms used to describe tool strings and tools. ‡ = not included in each logging run. NA = not applicable.

Table T9. Acronyms and units used for wireline tools.

Tool	Output	Explanation	Unit
APS		Accelerator porosity sonde	
	APLC	Near array porosity (limestone calibrated)	%
	SIGF	Formation capture cross section (Σ_f)	Capture units
	STOF	Tool standoff (computed distance from borehole wall)	in
DIT		Dual induction tool	
	IDPH	Deep induction resistivity	Ωm
	IMPH	Medium induction resistivity	Ωm
	SFLU	Spherically focused resistivity	Ωm
DSI		Dipole sonic imager	
	DTCO	Compressional wave delay time (Δt)	ms/ft
	DTSM	Shear wave delay time (Δt)	ms/ft
	DTST	Stoneley wave delay time (Δt)	ms/ft
FMS		Formation MicroScanner	
	C1, C2	Orthogonal hole diameters	in
	P1AZ	Pad 1 azimuth	Degrees
		Spatially oriented resistivity images of borehole wall	
GPIT		General purpose inclinometer tool	
	DEVI	Hole deviation	Degrees
	HAZI	Hole azimuth	Degrees
	F_x, F_y, F_z	Earth's magnetic field (three orthogonal components)	Degrees
	A_x, A_y, A_z	Acceleration (three orthogonal components)	m/s^2
HLDT		Hostile environment lithodensity tool	
	RHOM	Bulk density	g/cm^3
	PEFL	Photoelectric effect	b/e^-
	LCAL	Caliper (measure of borehole diameter)	in
	DRH	Bulk density correction	g/cm^3
HNGS		Hostile environment gamma ray sonde	
	HSGR	Standard (total) gamma ray	gAPI
	HCGR	Computed gamma ray (HSGR minus uranium contribution)	gAPI
	HFK	Potassium	wt%
	HTHO	Thorium	ppm
	HURA	Uranium	ppm
MGT		Multisensor gamma tool	
	GR	Gamma ray	gAPI
NGT		Natural gamma ray spectrometry tool	
	SGR	Standard total gamma ray	gAPI
	CGR	Computed gamma ray (SGR minus uranium contribution)	gAPI
	POTA	Potassium	wt%
	THOR	Thorium	ppm
	URAN	Uranium	ppm
TAP		Temperature/acceleration/pressure tool	°C, m/s^2, psi